e-ISSN: 2618-575X

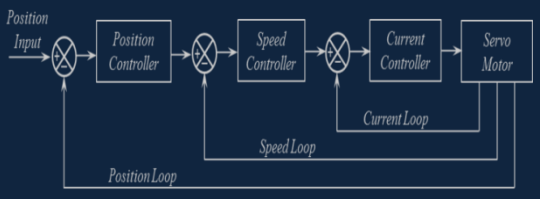

International Advanced Researches and Engineering Journal

Aerospace Engineering,
Aquaculture and Fisheries Engineering,
Architecture,
Bioengineering,
Chemical Engineering,
Civil Engineering,
Computer Engineering,
Electrical and Electronics,
Energy,
Environmental Engineering,
Food Engineering,
Geomatics Engineering,
Industrial Engineering,
Industrial Applications,
Machine Theory and Dynamics,
Manufacturing,
Mechanical Engineering,
Mechanics,
Mechatronics,
Medical,
Modeling and Simulation,
Physics Engineering,
Robotics,
Textile Engineering
Health in Engineering

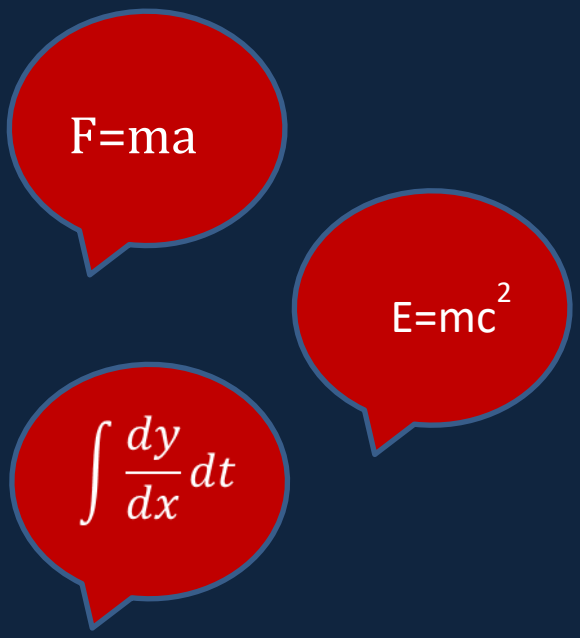

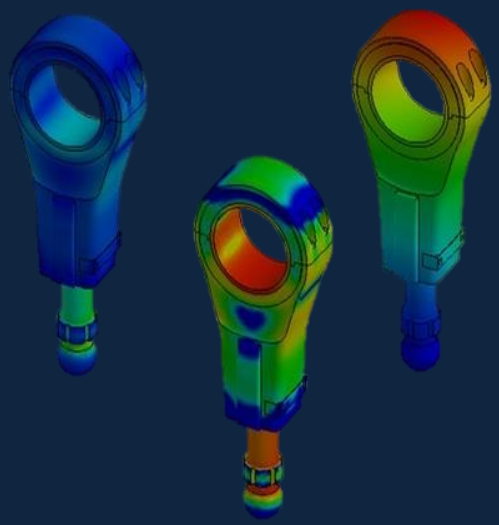

Editor-in-Chief
Dr. Recep HALICIOGLU

Volume: 02 / Issue: 01 / April 2018

e-ISSN: 2618-575X

Available online at www.dergipark.gov.tr

INTERNATIONAL ADVANCED RESEARCHES
and
ENGINEERING JOURNAL

Journal homepage: www.dergipark.gov.tr/iarej

International
Open Access

Volume 02
Issue 01

April, 2018

Journal Title	:	International Advanced Researches and Engineering Journal
Online ISSN	:	2618-575X
Abbreviated key-title	:	Int. adv. res. eng. j.
Other variant title	:	IAREJ
Subject	:	Technology (Applied Sciences) and Engineering
Publisher	:	Recep HALICIOGLU
Dates of publication	:	2017 - current
Frequency	:	Three times a year
Language	:	English
Medium	:	Online / Open Access
Web	:	www.dergipark.gov.tr/iarej
Country	:	Turkey
E-Mail	:	iarej.info@gmail.com; recephalicioglu@gmail.com

International Advanced Researches and Engineering Journal (IAREJ) is a double-blind peer-reviewed and publicly available online journal. The editor in chief of IAREJ welcomes the submissions that cover theoretical and/or applied researches on engineering and related sciences. IAREJ publishes **original papers** that are research papers and technical review papers.

IAREJ publication, which is open access, is free of charge. There is no article submission and processing charges (APCs).

IAREJ is indexed by:

Directory of Open Access Scholarly Researches (ROAD)
Directory of Research Journals Indexing (DRJI)
Google Scholar
Journal Factor
J-Gate
Index Copernicus
Rootindexing
Scientific Indexing Services (SIS)

Authors are responsible from the copyrights of the figures and the contents of the manuscripts, accuracy of the references, quotations and proposed ideas and the Publication Ethics.

Available online at www.dergipark.gov.tr

INTERNATIONAL ADVANCED RESEARCHES
and
ENGINEERING JOURNAL

Journal homepage: www.dergipark.gov.tr/iarej

International
Open Access

Volume 02
Issue 01

April, 2018

e-ISSN: 2618-575X

Owner / Publisher / Editor in Chief

Editorial Board

Editorial Assistants

Available online at www.dergipark.gov.tr

INTERNATIONAL ADVANCED RESEARCHES
and
ENGINEERING JOURNAL

Journal homepage: www.dergipark.gov.tr/iarej

e-ISSN: 2618-575X

International
Open Access

Volume 02
Issue 01

April, 2018

Table of Contents

Available online at www.dergipark.gov.tr

INTERNATIONAL ADVANCED RESEARCHES
and
ENGINEERING JOURNAL

Journal homepage: www.dergipark.gov.tr/iarej

International
Open Access

Volume 02
Issue 01

April, 2018

e-ISSN: 2618-575X

Research Article

Ab-initio calculations of structural, optical and electronic properties of $AgBiS_2$

Seyfettin Ayhan[a] , Gülten Kavak Balcı[a*]

[a] Department of Physics, Dicle University, Diyarbakır, Turkey

ARTICLE INFO

Article history:
Received 05 January 2018
Revised 19 March 2018
Accepted 20 March 2018

Keywords:
$AgBiS_2$
Ab-intio calculations
Wien2k
FPLAPW
Structural properties
Optical properties
Electronic properties

ABSTRACT

In this work, we use first-principles calculations based on density-functional theory generalized gradient approximation (Perdew Burke Ernzerhof, PBE). Cubic and hexagonal $AgBiS_2$ structures have been performed using the self-consistent full-potential linearized augmented plane wave (FPLAPW) method to investigate the structural, optical and electronic properties. We have calculated the ground-state energy, the lattice constant, DOS, band gap and dielectric constant of cubic and hexagonal $AgBiS_2$ by using Wien2k packet. The calculated physical properties of silver bismuth sulfide are compared with the experimental results and good agreement was observed.

1. Introduction

Recently, there are great attention on I–V–VI_2 ternary chalcogenide semiconducting compounds because of their many applications as a solar cell in linear, nonlinear, optoelectronic and thermoelectric devices [1,2,3]. In addition to experimental study there are intensive theoretical study on this material class [4,5]. Silver bismuth sulfide, one of these compounds, (AgBiS2) is a promising candidate for use as novel semiconductors[6, 7].

$AgBiS_2$ is considerable practical concern as a solar cell material, because its energy gap [7,8] is close to the optical energy gap of solar cell absorbers [9].

AgBiS2 has been studied because of exceptional its uncommon electronic and magnetic properties which can be applied in linear, non-linear, optoelectronic, and thermoelectric devices as well as optical recording media [4, 10,11].

$AgBiS_2$ nanocrystals are used in quantum dot-sensitized solar cells and it increases the conversion efficiency [12].

Accurate knowledge of the thermodynamic properties of β-AgBiS2 is very important not only for studies of ore genesis, processing of complex minerals, and the optimization of the extractive metallurgy of the base and precious metals but also for improved manufacturing of novel electronic materials incorporating β-AgBiS2 [4,13].

Ternary silver bismuth sulfide ($AgBiS_2$) is a typical member of I−V−VI_2 family. Bulk AgBiS2 crystallizes in the hexagonal phase (space group, P-3m1) at room temperature,) and transforms to a cubic rocksalt structure (space group, Fm-3m) at around 473 Kelvin[14]. It is known that there exist two phases of $AgBiS_2$, namely, the low temperature phase β-$AgBiS_2$ with a hexagonal structure and the high temperature phase α–$AgBiS_2$ with a cubic structure [10]. It is also some works show that mineral matildite ($AgBiS_2$) have orthorhombic phase with a=8.14 b=7.87 and c=5.69. α-$AgBiS_2$ has face-centered disordered cubic statistically NaCl-type structure with Ag and Bi atoms distributed indistinguishably (0, 0, 0; 0, 1/2,1/2) and S on the

* Corresponding author. Tel.: +90 *0412 2488550-3172*; Fax: +90 *0412 2488300*;
E-mail address: *gulten@dicle.edu.tr*
Note: This study was presented at International Advanced Researches and Engineering Congress 2017 (IAREC'17)

average in the other set of position (1/2, 1/2, 1/2; 0, 0, 1/2) (Figure 1.a.). β–phase of $AgBiS_2$ is hexagonal with space group 139 (P-3m1) and a =4.72, c=19.06 (Figure 1.c) [10,15].

Because of its physical properties, $AgBiS_2$ compound is used at widely area so we aimed to find more information about its physical properties and contribute the literature

In the present study, the ground-state energy, the lattice constant, DOS, band gap, structural, electronic and optical properties of cubic and hexagonal $AgBiS_2$ are investigated. According to our knowledge, no theoretical works have been performed for structural, electronic and optical properties of $AgBiS_2$ using the full-potential linearized augmented plane wave (FPLAPW) method.

This work is organized as follows: Section 2 describes our method and give the computational details, in Section 3 is given to the description of the results and Section 4 is for the conclusions.

2. Computational method

We studied structural, electronic and optical properties of both cubic and hexagonal $AgBiS_2$ compounds with in a self-consistent scheme by solving the Kohn–Sham equations based on Density Functional Theory with generalized gradient approximation (GGA) method [16]. The calculations were performed using the self-consistent full potential linearized augmented plane wave (FPLAPW) method [17] implemented in Wien2k code [18]. We select Perdew-Burke-Ernzerhof Generalized Gradient Approximation (PBE-GGA) exchange and correlation potentials described by Perdew-Burke-Ernzerhof (PBE) [18-21]. In the LAPW method the space is divided into non-overlapping muffin-tin (MT) spheres and interstitial region. We select muffin-tin sphere radii as 2.5 au for Ag and Bi, and 2.08 au for S. The convergence of the basis set was controlled by a cut off parameter $R_{MT}K_{max}$. The $R_{MT}K_{max}$ was selected as 8 value. The magnitude of the largest vector in charge density Fourier expansion (G_{max}) was selected as 12. The separation of valence and core states energy called the cutoff energy was chosen as -7 Ry. During SCF calculation, we select the 0.001e for charge and 0.0001 Ry for energy convergence criteria. For the Brillouin zone (BZ) integration, the tetrahedron method with 159 special k points in the irreducible wedge (2000 k-points in the full BZ) was used to construct the charge density in each self-consistency step.

Structural calculation of hexagonal $AgBiS_2$ was started with experimental lattice constant (a= 4.07, c =19.06 A^0) and atomic coordinate, given in Table 1 [16], and searched for minimum energy depend on volume. The electronic and optical calculations were performed with optimized structure data.

Because of cubic $AgBiS_2$ is disordered and Bi and Ag atoms distributed indistinguishably (Figure 1.a.) the cubic $AgBiS_2$ was studied as supercell 2x2x2. So Ag and Bi were settled in regular order position in NaCl type structure. The produced cell dimensions is 2 times and volume is 8 times larger than disordered unit cell structure (Figure 1.b.).

Table 1. Atomic positions of hexagonal $AgBiS_2$

Atom	x	y	z
Ag1	0	0	0
Ag2	1/3	2/3	0.672
Bi1	0	0	0.5
Bi2	1/3	2/3	0.163
S1	0	0	0.253
S2	1/3	2/3	0.926
S3	1/3	2/3	0.406

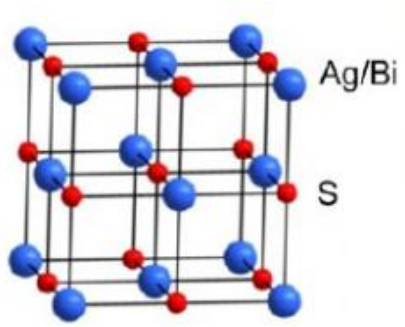

(a)

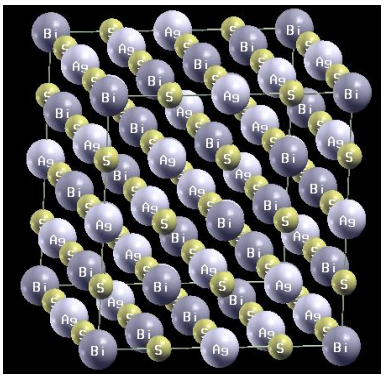

(b)

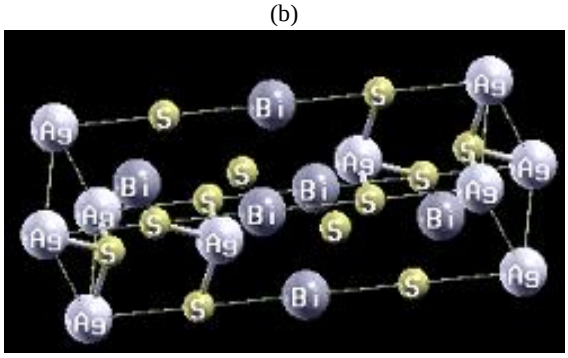

(c)

Figure 1. Unit cell of $AgBiS_2$ (a) NaCl disordered cubic structure, (b) $Ag_{0.5}Bi_{0.5}S$ supercell structure, (c) hexagonal $AgBiS_2$ structure

The volume optimization of supercell performed with ground state energy minimization. The electronic and optical calculations were performed with optimized lattice constant.

3. Results and discussion

3.1. Structural properties

To find ground state energy the total energy was calculated for different volume. The calculated total energies as a function of volume are fitted with Murnaghan's equation of state [22] to determine the ground state properties. We plotted total energy as a function of volume for hexagonal $AgBiS_2$ in Figure 2 and for cubic $Ag_{0.5}Bi_{0.5}S$ in Figure 3.

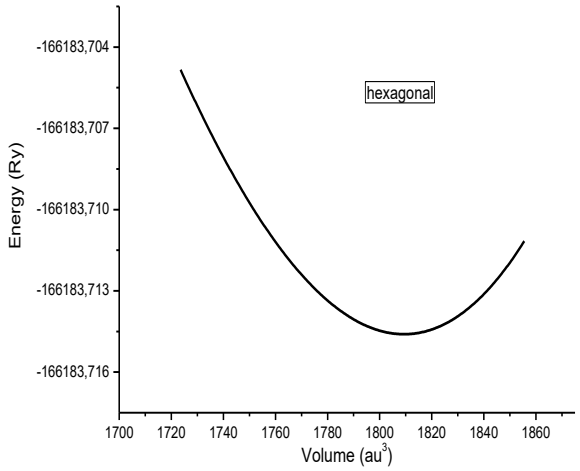

Figure 2. Dependence of total energy on unit cell volume for hexagonal AgBiS2

In Figure 2, it is can be seen that the minimum value of energy corresponds to the ground state volume 1809,3644 au^3 . Therefore, the calculated lattice constants for hexagonal $AgBiS_2$ are found a= 4,02 A^0 and c=19,054 A^0. Meanwhile, the experimental values of lattice constants are:

a= 4.07 A^0, c =19.06 A^0 [15]

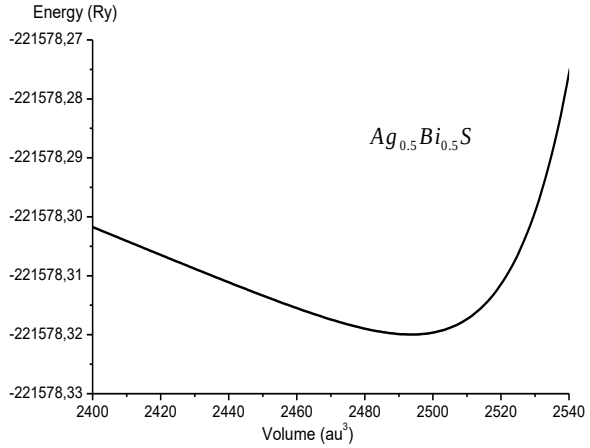

Figure 3. Dependence of total energy on unit cell volume for cubic $AgBiS_2$

In Figure 3, it is seen that the minimum value of energy corresponds to the ground state volume 2493,5740 au^3 Therefore, the calculated lattice constant for cubic $Ag_{0.5}Bi_{0.5}S$ is found a=11.3910 A^0. Meanwhile, the experimental value of lattice constant a = 5.648 A^0. The calculated results are good agreement with experimental data if we consider supercell is 2 times larger than experimental unit cell.

Calculated volume cell dimensions, bulk modulus (B) and minimum energy (E) values for both phase are given in Table 2

Table 2. Calculated cell dimensions, bulk modulus and minimum energy of cubic and hexagonal $AgBiS_2$ compound

Parameter	a (A^0)	c (A^0)	B (GPa)	E (Ry)
Hexagonal $AgBiS_2$	4,068	19,054	80,07	-166183,71460
Cubic $Ag_{0.5}Bi_{0.5}S$	11,391	-	54,8389	-221578,31996

The structural stability of cell is determined by cohesive energy calculation. According to cohesive energy [23]:

$$E_{coh} = -\frac{E^{tot}_{AgBiS_2} - kE^{tot}_{Ag} - mE^{tot}_{Bi} - nE^{tot}_{S}}{k+m+n}$$

Where $E^{tot}_{AgBiS_2}$, E^{tot}_{Ag}, E^{tot}_{Bi}, E^{tot}_{S} are total energy for $AgBiS_2$ unit cell, isolated Ag, Bi and S atom, respectively. k, m and n indexes refer to the number of each atom in the unit cell.

We obtained the value of cohesive energy 2.38 eV/atom for cubic $Ag_{0.5}Bi_{0.5}S$ and 2.33 eV/atom for hexagonal phase $AgBiS_2$.

3.2. Electronic properties

It is well known that the electronic band structure and density of states (DOS) are important quantities to determine the crystal structure [24]. In order to understand bonding character clearly, the density of states (DOS) is calculated, as shown in Figure 4 and Figure 5. In the figures, Fermi level were settled at zero point. Evidently, the total DOS's of the two phases exhibit semiconductor feature. It can be seen from Figure 4.b and 5.b that the big DOS contribution at the valence band are given by silver. At the conducting band, the contribution of silver decreases and the contribution of bismuth increases. So we can say that charge transfer is occurred from silver to bismuth at Fermi energy level, and the bond character of both phase are largely covalent bonding.

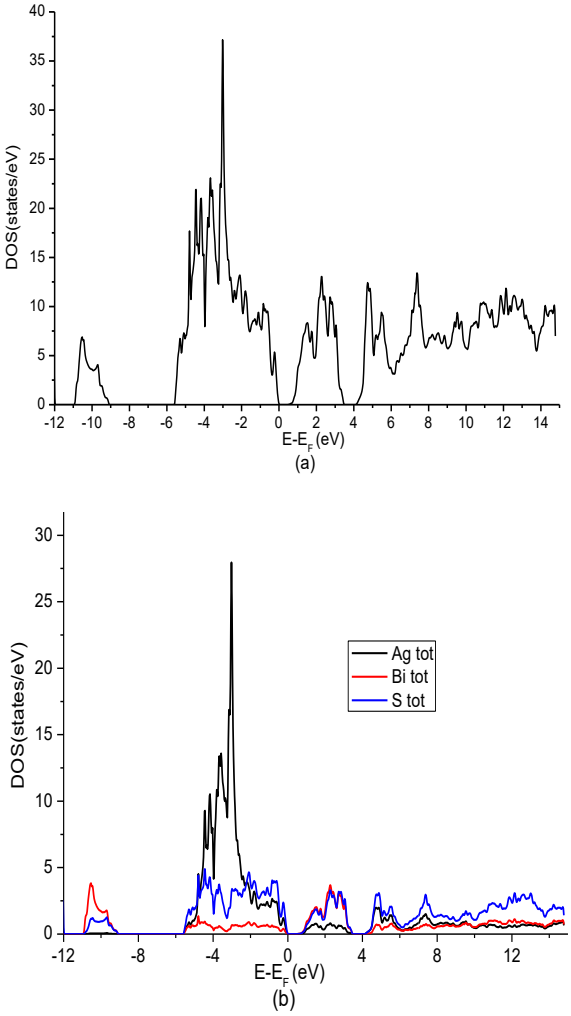

Figure 4. Calculated total and partial DOS for hexagonal $AgBiS_2$ (a) total DOS (b) partial DOS

We plotted an electronic band chart to understand the electronic properties of the both cubic and hexagonal phase structures (Figure 6. and Figure 7.). At the figures the Fermi energy level set to origin. In the Figure 6, top of valence band is located between the high symmetry points K and Γ while the bottom of conduction band is located at the A in the Brillion Zone [25]. Therefore, hexagonal $AgBiS_2$ has an indirect band gap with value of 0.463 eV.

In the Figure 7, top of valence band is located at the high symmetry point X while the bottom of conduction band is located at the L in the BZ. Therefore, cubic $AgBiS_2$ has an indirect band gap with value of 0.83 eV. The calculated band structure is in good agreement with previous works [14].

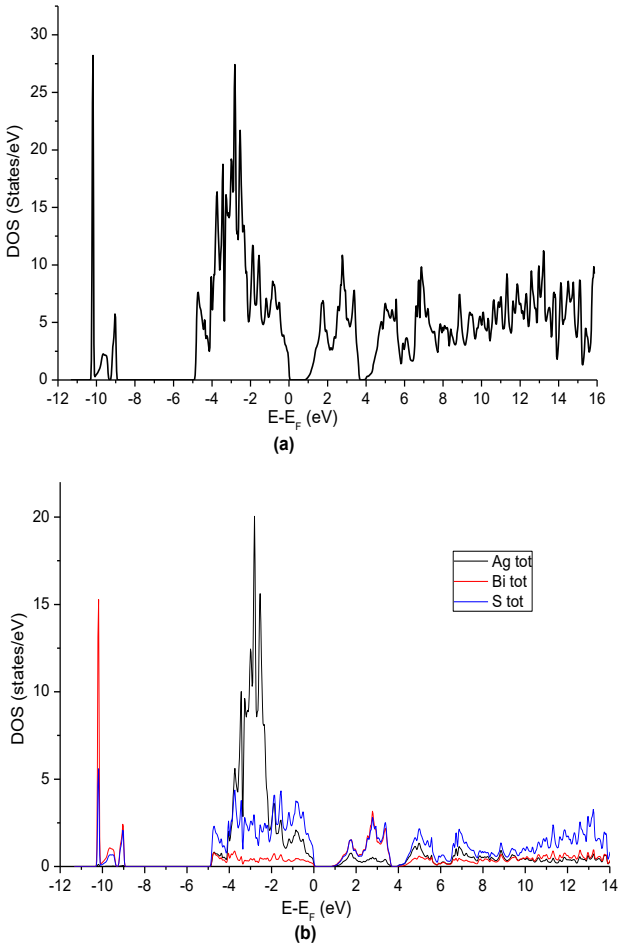

Figure 5. Calculated total and partial DOS for cubic $AgBiS_2$ (a) total DOS (b) partial DOS

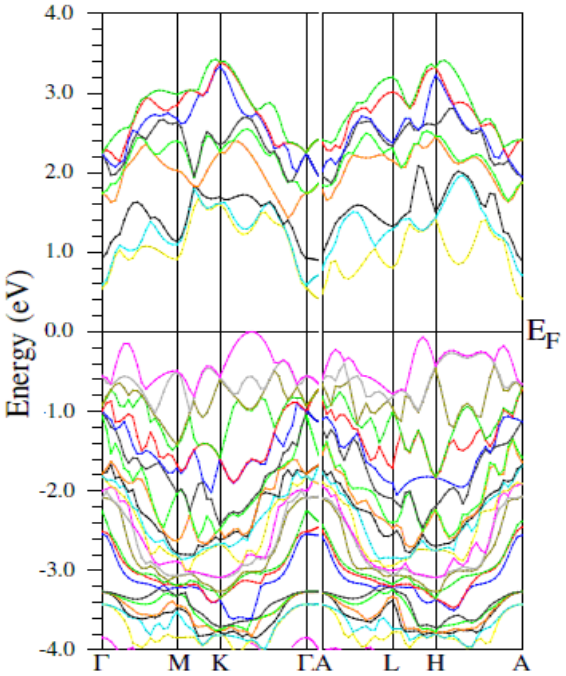

Figure 6. Electronic band plot of hexagonal $AgBiS_2$

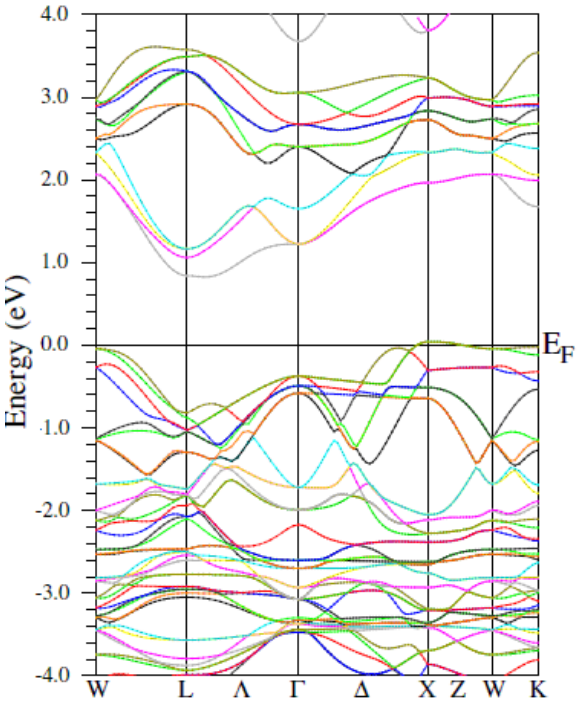

Figure 7. Electronic band plot of cubic $AgBiS_2$

3.3. Optical properties

Determining optical properties of materials let us to develop new optoelectronic applications. So we calculated dielectric function, optical conductivity, absorption, energy loss function and reflection of both cubic and hexagonal $AgBiS_2$ to contribute this area. All calculations performed with no intra band contributions added.

3.3.1. Dielectric function

The calculation of complex dielectric function can be considered as one of the best approaches to investigate the optical properties of materials [26]. The optical response of a medium at all photon energies is described by the dielectric function:

$$\varepsilon(\omega) = \varepsilon_1(\omega) + i\varepsilon_2(\omega)$$

The real part $\varepsilon_1(\omega)$ and the imaginary part $\varepsilon_2(\omega)$ corresponds to the dispersive and absorptive behavior of the material, respectively. The real and imaginary parts of dielectric function of cubic and hexagonal phase of $AgBiS_2$ calculated without the addition of spin orbit interaction are plotted in Figure 8 and Figure 9.

As seen in the Figure 8 and 9, the static values of real part of dielectric constant, ε_0, is 20 and 16.4, respectively.

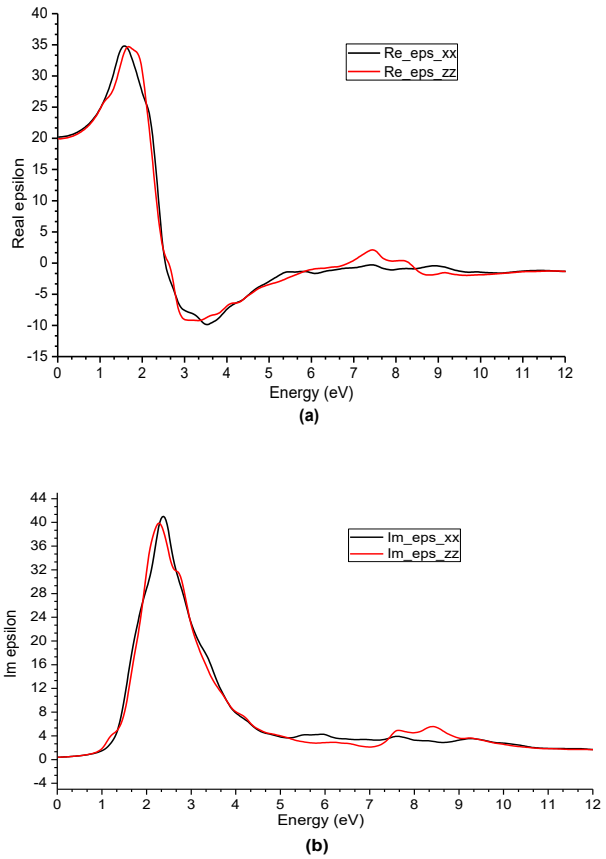

Figure 8. Calculated real and imaginary part of epsilon hexagonal $AgBiS_2$ a) real part epsilon (b) imaginary part epsilon

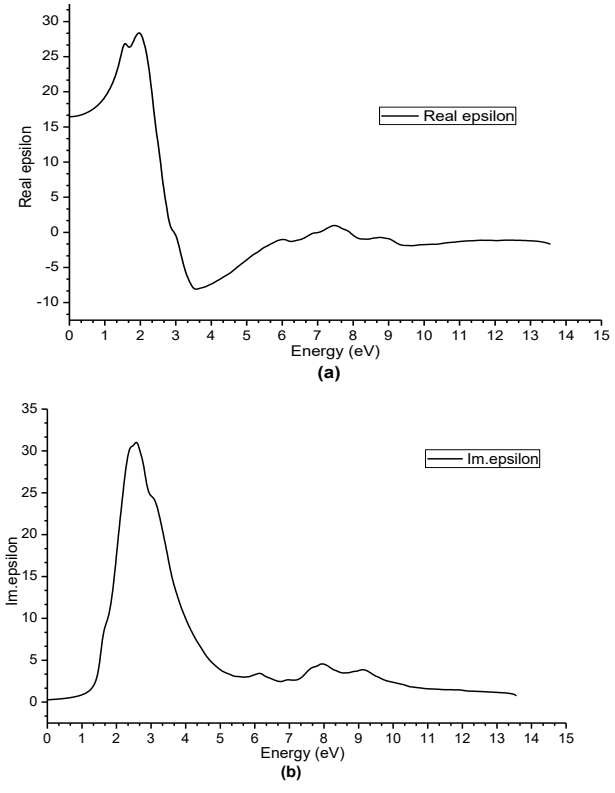

Figure 9. Calculated real and imaginary part of epsilon cubic phase of $AgBiS_2$ a) real part b) imaginary part

3.3.2. Absorption coefficient

The absorption coefficient determines the ability of material to absorb the incident photon of specific frequency [25]. We can write the absorption coefficient:

$$\alpha(\omega)_j = 2\omega / c(-\mathrm{Re}(\varepsilon(\omega)_j) + \left|\varepsilon(\omega)_j\right| / 2)^{1/2}$$

Calculated absorption coefficient of $AgBiS_2$ are plotted in Figure 10.

It can be seen from Figure 10, **t**he absorption part of hexagonal $AgBiS_2$ spectra starts with 0.8 eV energy, and the absorption part of cubic $AgBiS_2$ spectra starts with nearly 1 eV energy.

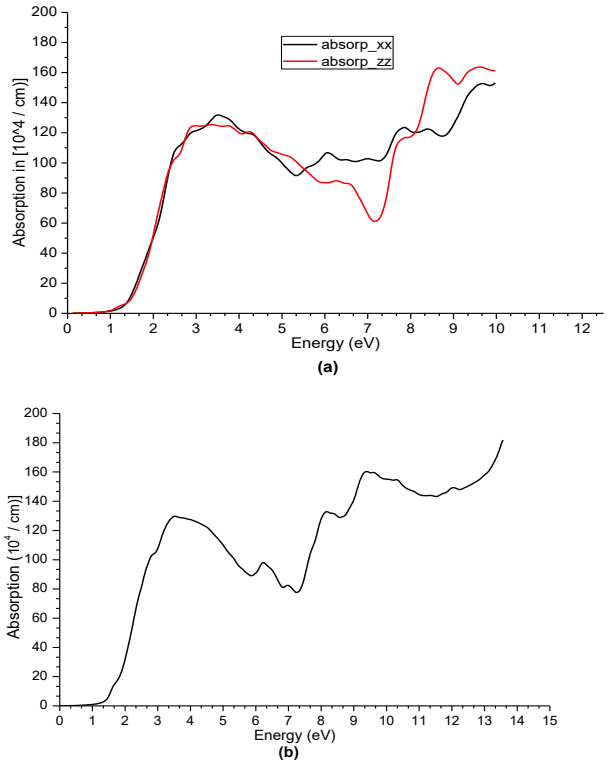

Figure 10. Calculated optical absorption of $AgBiS_2$
a) hexagonal phase b) cubic phase

3.3.3. Optical conductivity

The optical conductivity $\sigma(\omega) = \alpha nc / 4\pi$ corresponds to the conduction of electrons produced when photon of certain frequency is incident upon a material [25]. The optical conductivity of hexagonal $AgBiS_2$ given in Figure 11.a. E_0 =0.65 eV and the first peak appears for xx direction 2.408 eV and for zz direction 2.327 eV. The optical conductivity(sigma) has the maximum value of xx direction 13227 [1 / (Ohm cm)] and 12381 [1 / (Ohm cm)] for zz direction corresponds to visible region of the electromagnetic spectrum.

The optical conductivity of cubic $AgBiS_2$ shown in Figure 11.b. E_0 =0.8 eV, the first peak appears for 3.088 eV and the optical conductivity has the maximum value of 10064 [1 / (Ohm cm)] corresponds to visible region of the electromagnetic spectrum.

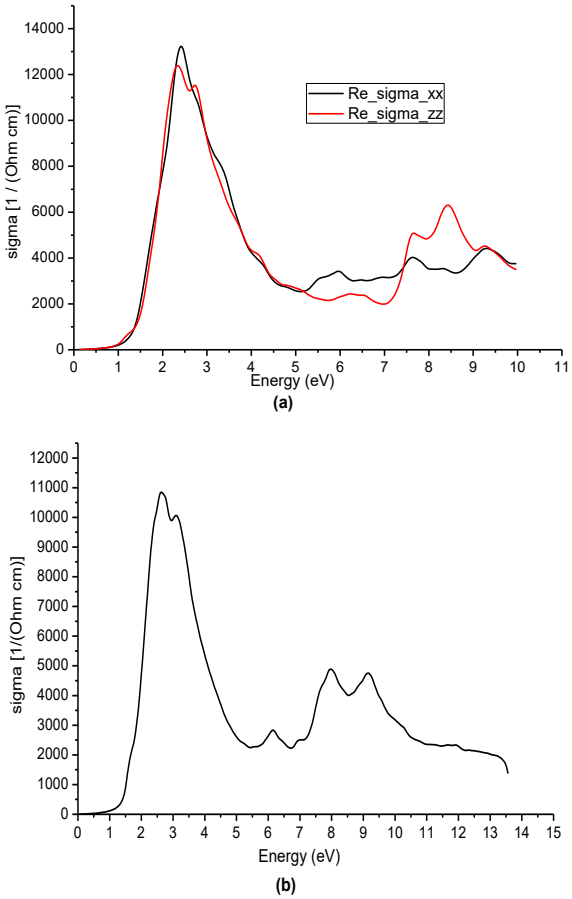

Figure 11. Calculated optical conductivity of AgBiS2
a) hexagonal phase, b) cubic phase

3.3.4. Reflectivity

The value of reflectivity at the zero frequency is described as the static reflectivity (R_0). For the cubic phase of $AgBiS_2$, R_0 =0.36 and for the hexagonal $AgBiS_2$ R_0 =0.4 (Figure 12.a.). It can be seen from figure the reflectivity has many peaks depending on energy. The reflectivity has a maximum value R_{max}=0.617 at the 4.14 eV energy and minimum value R_{min} = 0.186 at 7.31 eV energy for cubic $AgBiS_2$.

The maximum reflectivity values of hexagonal $AgBiS_2$ are 0.656 at the 3.36 eV energy for xx direction and 0.638 at the 2,48 eV energy for zz direction. The minimum values of reflectivity for hexagonal phase are 0.281 at the 7.39 eV energy at xx direction and 0.133 at the 7.17 eV energy for zz direction.

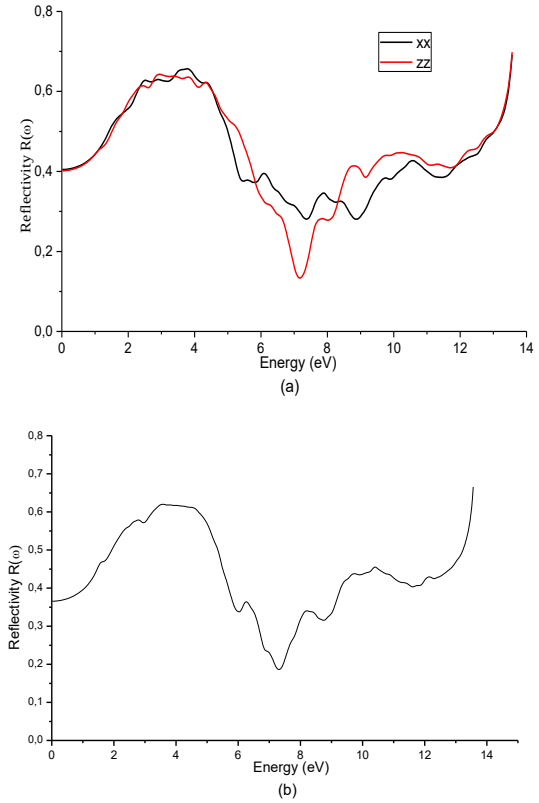

Figure 12. Calculated reflectivity coefficient, R(ω) index a) hexagonal phase $AgBiS_2$ b) cubic phase $AgBiS_2$

3.3.5. Energy loss function

The energy loss function L(ω) describes the frequencies correspond to the plasma resonance. Plasma resonance occurs when the frequency of incident radiations matches with the frequency of plasmas. The energy loss function depend on incident energy for cubic and hexagonal of $AgBiS_2$ is plotted in Figure 13. The loss function shows peaks at 5.37 eV, 7.22 eV, 8.72 eV and 11.44 eV for xx direction and at 6.93 eV, 7.96 eV, 9.13 eV, 9.83 eV, 11.68 eV for zz direction(Figure 13.a.), and for cubic phase shows peaks at 5.89 eV, 6.79 eV, 8.67 eV and 12.31 eV(Figure 13b).

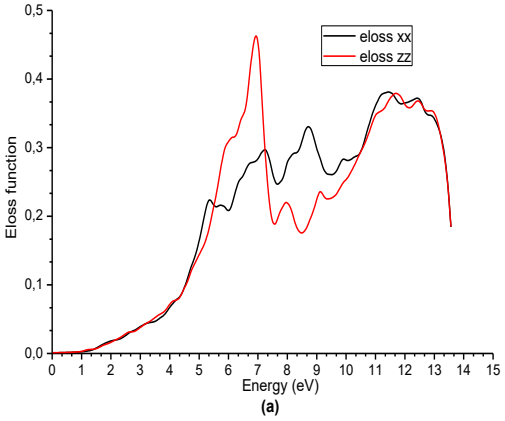

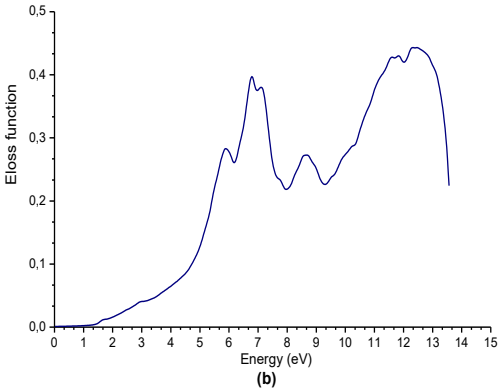

Figure 13. Calculated electron energy loss spectrum of $AgBiS_2$ a) hexagonal phase b) cubic phase

4. Conclusions

We have investigated structural, electronic and optical properties both cubic and hexagonal $AgBiS_2$ using all electrons full potential linearized augmented plane wave (FPLAPW) method based on DFT within generalize gradient approximation (GGA). We calculated ground state energy, cell constants, bulk modulus, and cohesive energy. The calculated cell constants are good agreement with experimental works. Calculated cohesive energy of compounds show that the structures have mechanical stability.

DOS calculation of both phase of cubic and hexagonal are plotted. DOS plot show the both phase have semiconducting features. The DOS plots show that the bond character of compounds are covalent bonding. The calculated electronic band structure shows that the both phase of $AgBiS_2$ are indirect band gap semiconductor. The calculated band gap of cubic phase is 0.83 eV and it has a good agreement with compare to other experimental results (bulk 0.8 eV, monocrystalline 1 eV) [14]. The hexagonal $AgBiS_2$ has indirect band gap with 0,463 eV.

To determine optical properties of $AgBiS_2$ we calculated optical parameters such as dielectric function, absorption coefficient, refractive index, reflectivity and energy loss function for radiation up to 14.0 eV.

Calculated electronic and optical properties of $AgBiS_2$ show that the both phase of $AgBiS_2$ compounds are good candidate for electronic devices, optical devices and solar cell applications.

Acknowledgement

This research was supported by the Dicle University Scientific Research project coordination unit (project no: FEN.15.016). Thanks to Prof. Peter Blaha and Prof. Karlheinz Schwarz for supplied free Wien2k code to us.

References

1. Samanta, L.K., S. Chatterjee, On the linear, nonlinear, and optoelectronic properties of some multinary compound semiconductors, Phys. Status Solidi B, 1994, 182, K85.

2. Aliev, S.A., S.S. Raginov, Thermoelectric Proper- ties of Ag–Sb–Te Materials, Neorg. Mater, 1992, 28- 329.

3. Saadi B. , D. Maouche, N. Bouarissa, Y. Medkour, First principles study of structural, electronic and optical properties of AgSbS2,Materials Science in Semiconductor Processing,16, 2013, 1439–1446

4. Tesfaye, F., Taskinen, P., Electrochemical study of the thermodynamic properties of matildite (β-$AgBiS_2$) in different temperature and compositional ranges, Solid State Electrochem, 2014, 18:1683–1694

5. Hoang, K., S.M. Mahant, Atomic and electronic structures of I-V-VI_2 ternary chalcogenides, Journal of Science: Advanced Materials and Devices Volume 1, Issue 1, March 2016, 51-56

6. Shen, G., D. Chen, K. Tang, Y. Qian, Polyol mediated synthesis of nanocrystalline M_3SbS_3 (M = Ag, Cu), J. Cryst. Growth 252, 2003, 199.

7. Nakamura, M., H. Nakamura, T. Ohsawa, M. Imura, K. Shimamura, N. Ohashi, AgBiS2 single crystal grown using slow cooling method and its characterization, Journal of Crystal Growth, 2015, 411, 1-3.

8. Pejova, B., D. Nesheva, Z. Aneva, A. Petrova, Photoconductivity and Relaxation Dynamics in Sonochemically Synthesized Assemblies of $AgBiS_2$ Quantum Dots, J. Phys. Chem., 2011, C 115, 37.

9. Zdanowicza, T., T. Rodziewiczb, M. Zabkowska-Waclawek, Theoretical analysis of the optimum energy band gap of semiconductors for fabrication of solar cells for applications in higher latitudes locations,Sol. Energy Mater. Sol. Cells ,2005, 87, 757-769.

10. Chen, D., G.Z. Shen, K.B. Tang, X. Jiang, L.Y. Huang, Y. Jin, Y.T. Qian, Microwave synthesis of $AgBiS_2$ dendrites in aqueous solution, Inorg. Chem. Commun., 2003, 6, 710–712.

11. Yan, J., J. Yu, W. Zhang, Y. Li, X. Yang, A. Li, X. Yang, W. Wang, J. Wang, Synthesis of Cu_3BiS_3 and AgBiS2 crystallites with controlled morphology using hypocrellin template and their catalytic role in the polymerization of alkyls lane, J. Mater. Sci. 2012, 47 4159–4166.

12. Liang, N., W. Chen, F. Dai, X. Wu,W. Zhang, Z. Li, J. Shen, S. Huang, Q. He, J. Zai, N. Fang and X. Qian, Homogenously hexagonal prismatic AgBiS2 nanocrystals: Controlled synthesis and application in quantum dot-sensitized solar cells. CrystEngComm, 2015, 17, 1902-1905.

13. Huang, P. C., Yang, W. C., and Lee, M. W., $AgBiS_2$ Semiconductor-Sensitized Solar Cells, *J. Phys. Chem. C*, 2013, 117 (36), pp 18308–18314.

14. Satya N. G. and K. Biswas, Cation Disorder and Bond Anharmonicity Optimize the Thermoelectric Properties in Kinetically Stabilized Rocksalt $AgBiS_2$ Nanocrystals, Chem. Mater., 2013, 25, 3225−3231.

15. Galler, S. and J.H., Wernick Ternary semiconducting compounds with sodium chloride-like structure: $AgSbSe_2$, $AgSbTe_2$, $AgBiS_2$, $AgBiSe_2$ acta crystallographica, 1959,12, 46-54.

16. Perdew, J.P., J.A. Chevary, S.H. Vosko, K.A. Jackson, M.R. Pederson, D.J. Singh, C.Fiolhais, Atoms, molecules, solids, and surfaces: Applications of the generalized gradient approximation for exchange and correlation, Phys. Rev. B., 1992, 46, 6671.

17. Singh, D.J., Planes Waves, Pseudo-Potentials and the LAPW Method, Kluwer Academic Publishers, 1994, .Boston, Dortrecht, London.

18. Blaha, P., K. Schwarz, G.K.H. Madsen, D. Kvasnicka, J. Luitz, WIEN2k, An Augmented Plane Wave + Local Orbitals Program for Calculating Crystal Properties, Karlheinz Schwarz, Techn Universitat Wien, Austria, 2001, ISBN:3-9501031-1-2.

19. Perdew, J.P., K. Burke, Y. Wang, Physical Review, Erratum: Generalized gradient approximation for the exchange-correlation hole of a many-electron system, Phys. Rev. 1996, B 54, 16533.

20. Perdew, J.P., S. Burke, M. Ernzerhof, Generalized Gradient Approximation Made Simple, Physical Review Letters, 1996, 773865.

21. Kervan, N. S. Kervan, A first-principle study of half-metallic ferrimagnetism in the Ti_2CoGa Heusler compound, Journal of Magnetism and Magnetic Materials, 2012, 324, 4, 645-648.

22. Murnaghan, F.D., Proceedings of the National Academy of Sciences of the United States of America, 1947, 30, 244.

23. Mosayeb N., J. Jalilian, A.H. Reshak, Electronic and optical properties of pentagonal-B_2C monolayer: A first-principlescalculation, Int. J. Mod. Phys. B, 2017, **31**, 1750044.

24. Erdinc, B., M.N. Secuk, M. Aycibin, S.E. Gülebagan, E. K. Dogan, H. Akkus, Ab-initio Calculations of Structural, Electronic, Optical, Dynamic and Thermodynamic Properties of HgTe and HgSe, Computational Condensed Matter, 4, 2015, 6-12.

25. Setyawan, W., S. Curtarolo, High-throughput electronic band structure calculations: Challenges and tools, Computational Materials Science, 2010, 49, 299–312.

26. Hilal, M., R. Bahroz, S.H. Khan, A. Khan, Investigation of electro-optical properties of InSb under the influence of spin-orbit interaction at room temperature, Materials Chemistry and Physics, 2016, 184, 41-48.

Available online at www.dergipark.gov.tr

INTERNATIONAL ADVANCED RESEARCHES and ENGINEERING JOURNAL

Journal homepage: www.dergipark.gov.tr/iarej

e-ISSN: 2618-575X

International Open Access

Volume 02
Issue 01

April, 2018

Research Article

Co-application of EDDS and ZnO nanoparticles with TiO_2Ag nanoparticles on rye

Zeynep Görkem Doğaroğlu[a]* and Nurcan Köleli[a]

[a]Department of Environmental Engineering, Mersin University, Mersin, Turkey

ARTICLE INFO

Article history:
Received 05 March 2018
Revised 19 March 2018
Accepted 20 March 2018

Keywords:
Interaction
Seed germination
Titanium dioxide-silver
Zinc oxide

ABSTRACT

The aim of this study was to determine the effects of $nTiO_2Ag$, co-application of nZnO and $nTiO_2Ag$ and co-application of EDDS as an organic acid with $nTiO_2Ag$ on seed germination, seedling vigor, plumule and radicle length of rye. Ten seeds were placed in petri-dishes with double layer of filter paper which used as an inert material. Then 5 mL $nTiO_2Ag$, nZnO-$nTiO_2Ag$ and EDDS-$nTiO_2Ag$ suspensions were added to every petri dish with different concentrations (control, 50, 100 and 200 mg/L). Treatment of nZnO-$nTiO_2Ag$, especially at concentration of 50 mg/L, promoted the germination rate, seedling vigor, plumule and radicle elongation. The highest seedling vigor index (SVI) was observed at concentration of 50 mg/L nZnO-$nTiO_2Ag$. Seedling vigor index of rye seeds was decreased after treatment of $nTiO_2Ag$. The plumule elongation increased with treatment of all test chemicals and radicle elongation was increased nZnO-$nTiO_2Ag$ and EDDS-$nTiO_2Ag$ exposure compared to control. This is the first report on the effect of co-application of ZnO-TiO_2Ag nanoparticles and co-application of EDDS-TiO_2Ag nanoparticles on rye growth.

1. Introduction

Nanotechnology is a manipulation of nature that has emerged through the use of basic sciences, material science and engineering at nano-scale. Nowadays, nanomaterials are widely used in different fields such as cosmetics, agriculture, water and air purification and wastewater treatment, environmental remediation, and food additives as shelf life extender and packaging agents. Their unique properties (shape, size, huge specific surface area, high reaction activity, etc.) [1,2] make nanoparticles different from the other chemicals and contaminants. Toxicological studies have been increased because of increasing production, usage and disposal of nanoparticles pose a threat to the environment [3].

Plants are used to determine the potential toxicity of nanoparticles due to they can uptake and accumulate the nanoparticles easily [4]. Uptake and accumulation of nanoparticles by plants may change germination rate, shoot and root length [3]. The use of nanoparticles in agriculture was mostly theoretical in last decade [5] but using in fields increase day by day. Although, nanomaterials have some advantage, the negative effects of nanoparticles on plant productivity, soil microbes and environment should not overlook [6].

The interaction between two different nanoparticles, nanoparticles and organic materials and/or nanoparticles and biological environment is not yet well understood. Co-application of nanoparticles may cause them to accumulate in the soil and could be threatened plants. Plants can generally be exposed to both different nanoparticles and inorganic and organic contaminants, such as chelating agents through the soil in many ways [7].

Titanium dioxide nanoparticles ($nTiO_2$), zinc oxide nanoparticles (nZnO) and silver (nAg) nanoparticles are the most widely used nanoparticles in many industries. Previous reports have shown these nanoparticles responsible for toxicity in plants [8]. Cai et al. [7] indicated that, $nTiO_2$ will accumulate in soil and its concentration will increase accordingly. Silver nanoparticles are mostly used as antimicrobial agents in plant protection process [2,9,10]. Several papers reported effects of TiO_2, ZnO, and Ag nanoparticles in plants. Doğaroğlu and Köleli [11] reported that $nTiO_2$ and titanium dioxide-silver nanoparticles ($nTiO_2Ag$)

* Corresponding author. Tel.: *+90 324 361 00 01*; Fax: *+90 324 361 00 32*;
E-mail address: *gorkemgulmez@gmail.com*

Note: This study was presented at International Advanced Researches and Engineering Congress 2017 (IAREC'17)

enhanced the seed germination of lettuce *(Lactuca sativa)*. Jian et al [12] investigated impact of ZnO nanoparticles on pearl millet, tomato, and wheat. Authors determined that 1000 mg/L nZnO inhibited wheat seed germination around 60%.

Chelating agents such as ethylene-diaminedisuccinic acid (EDDS) are highly effective in remediating heavy metal-contaminated soils.

The impact of nanoparticles on living organisms has attention from researchers. Determining these impacts is important to sustainable and healthy environment. It should be noted that the amount of nanoparticle-contaminated field increases day by day because of using nano-products. Plants are the most important component between soil and nanoparticles. Using plants for soil remediation has some advantages such as, sustainability, low cost and environmentally friendly, as against other soil remediation techniques. Seed germination rates and seedling growth are most measured to assess nanoparticles effects [13]. Thus, the first and most important step of this study was to investigate seed germination rate of rye under exposure of different nanoparticles combinations and nanoparticles-chelating agent (EDDS). It was not only investigated seed germination, but also seedling vigor, plumule and radicle length of rye and the effectiveness and impacts of EDDS due to its low cost, good degree of biodegradability and high efficacy of metal extraction on seed germination and seedling growth of rye.

2. Materials and Methods

2.1 Chemicals

Dr. Birol Karakaya synthesized TiO_2Ag and ZnO nanoparticles using a combination of sol-gel and hydrothermal methods. Ethylen-diamine disuccinic acid (EDDS) was prepared at concentration of 10 mg/L from commercial EDDS (~ 35% in H_2O, Sigma-Aldrich). The average size of ZnO and TiO_2Ag nanoparticles was determined using zeta-sizer Ver. 6.32 (Malvern Instruments Ltd.) using a 1 mL disposable cuvette.

2.2 Preparation of Suspensions and Treatment

TiO_2Ag nanoparticles suspensions were prepared at concentrations of 50, 100 and 200 mg/L. 10 mg/L ZnO nanoparticles and 10 mg/L EDDS solution was prepared from 100 mg/L stock nZnO solution and from 40 mM EDDS stock solution.

Rye seeds were purchased from Mersin Province, Turkey. Rye was selected for the present study as a representative cereal crop. This test plant can resist to aridity, cold climates and high saline soil, due to having strong root systems.

The seeds of uniform size were selected to minimize error in germination assay. Experiments were performed using 10 seeds in 10 cm petri dishes for seven days. The seeds were sterilized in 70% ethanol for 30 s and then exposed to 3% sodium hypochlorite for 10 min. After the sterilization, seeds were shaken in ultrapure water five times for 5 min. Double-layer of filter paper cut and placed in petri dishes was used as inert material. Ten seeds were placed in every petri dish and were separately treated with 5 mL test chemicals. Petri dishes placed in a dark chamber till germination at 25 ^oC.

Three different applications were realized in the experiments. In the first application, rye seeds treated with nTiO_2Ag at concentration of 50, 100 and 200 mg/L. Control seeds were treated only 5 mL distilled water; in the second application, the seeds treated with co-application of nTiO_2Ag and nZnO. In this step 10 mg/L nZnO and the concentration of 50, 100 and 200 mg/L nTiO_2Ag were co-applied. Control groups include only 10 mg/L nZnO. And in the last application, the seeds treated with co-application of the concentration of 50, 100 and 200 mg/L nTiO_2Ag and 10 mg/L EDDS. Control groups include only 10 mg/L EDDS.

Number of germinated seeds was recorded every 24 hours for 7 days. After 7 days from the date of germination, primary root and shoot length of each seedling was measured by millimetric paper (3 replicates per treatment). Germination percentage (%) was calculated as described by Mahmoodzadeh et al [14]; Afrakhteh et al [15] in the following Formula (1) and seedling vigor index (SVI) was calculated by the formula described by Prasad et al [16] in the following Formula (2).

$$\text{Germination percentage (GP)} = \text{TNSG} / \text{TNST} \times 100 \quad (1)$$

Where; TNSG is the total number of seeds germinated; TNST is the total number of seed tested.

$$\text{Seed Vigor Index} = \text{Germination percentage (\%)} \times (\text{Root length} + \text{Shoot length}) \quad (2)$$

3. Results and Discussion

3.1 Nanoparticles Characterization

The average size of ZnO and TiO_2Ag nanoparticles was determined using a zeta-sizer. Average size of nZnO was 31.5 nm, and average size of nTiO_2Ag was 78.2 nm.

3.2 Effect of nTiO_2Ag, Co-application of nTiO_2Ag-nZnO, and nTiO_2Ag-EDDS on Seed Germination

Seed germination and root elongation assays are most valid methods to assess the phytotoxicity of organic and inorganic chemicals [17]. The effects of nTiO_2Ag, co-application of nZnO-nTiO_2Ag, and EDDS- nTiO_2Ag at various concentrations (50, 100 and 200 mg/L) were tested on rye seeds and shown in Figure 1. The results indicated that exposure of 10 mg/L nZnO and 10 mg/L EDDS was increased germination rate at concentration of

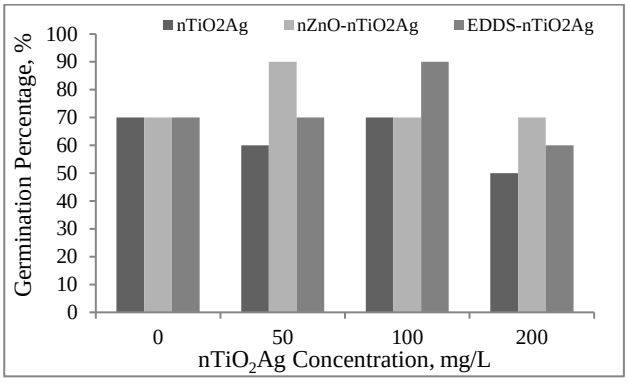

Figure 1. Seed germination percentage of rye; test chemicals include 10 mg/L nZnO or 10 mg/L EDDS and different concentration $nTiO_2Ag$, control groups include only distilled water.

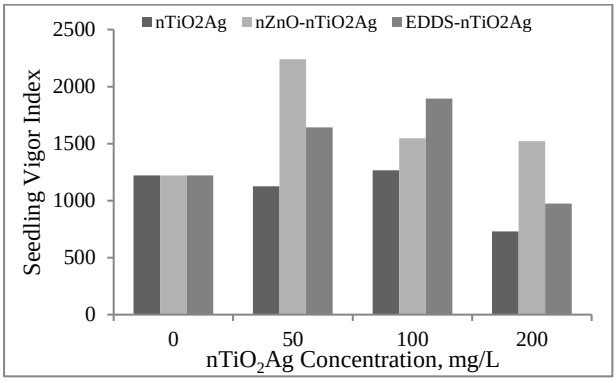

Figure 2. Seedling vigor index of rye; test chemicals include 10 mg/L nZnO or 10 mg/L EDDS and different concentration $nTiO_2Ag$, control groups include only distilled water.

50 and 100 mg/L $nTiO_2Ag$, respectively. The minimum seed germination was observed at concentration of 200 mg/L just $nTiO_2Ag$ as 50%, and the maximum germination percentage was observed both at concentration of 10 mg/L nZnO-50 mg/L $nTiO_2Ag$ co-application and 10 mg/L EDDS-100 mg/L $nTiO_2Ag$ co-application as 90%.

There are contradictory results about the plant-nanoparticles interaction in literature depending on plant species, nanoparticles types and application dose. Doğaroğlu and Köleli (2017) demonstrated that nZnO and nTiO2 nanoparticles had no effect on seed germination of barley [8], while exposing barley to nAg caused partial inhibition (13% germination rate) at concentration of 1500 mg/L was reported [18]. Xiang et al (2015) showed that nZnO did not affect germination rates at concentration of 1–80 mg/L chinese cabbage [19]. Another study showed that seed germination of ryegrass and flax was inhibited by nAg at 750 and 1500 mg/L [18].

3.3 Effect of $nTiO_2Ag$, Co-application of nZnO-$nTiO_2Ag$, and EDDS- $nTiO_2Ag$ on Seedling Vigor

Seedling vigor is one of the quality parameter of seed and it is a supplemental data for seed germination [12]. The seedling vigor index of rye was shown in Figure 2. Vigor index of control groups of rye was 1221.89. The maximum seedling vigor index was observed at concentration of 50 mg/L nZnO- $nTiO_2Ag$ (2239.0), and the minimum data was obtained at concentration of 200 mg/L $nTiO_2Ag$ (730.56). Treatment of 10 mg/L nZnO promoted the seedling vigor in all concentration of $nTiO_2Ag$. Similar result was observed by Prasad et al. (2012) when peanut seeds were treated with at concentration of 1000 mg/L nZnO [16].

Also treatment of 10 mg/L EDDS increased the seedling vigor except 200 mg/L $nTiO_2Ag$ concentration with respect to control rye seedlings.

Seedling vigor index of rye seeds was decreased after treatment of $nTiO_2Ag$. Co-application of nZnO-$nTiO_2Ag$ and co-application of EDDS-$nTiO_2Ag$ was promoted the seedling vigor. These results proved that the interaction between different nanoparticles and interaction between chelating agent and nanoparticles is important for the uptake of nanoparticles by plants and environmental fate and risk of nanoparticles.

3.4 Effect of $nTiO_2Ag$, Co-application of nZnO-$nTiO_2Ag$, and EDDS- $nTiO_2Ag$ on Seedling Growth

In order to understand the possible effects of co-application of different metal oxide nanoparticles and metal oxide nanoparticles-chelating agents, seedling growth (plumule and radicle elongation) was investigated in this study and shown in Figure 3.

Roots have an important role in plant development. The embryonic root called as radicle grows during the seed germination process. If the nanoparticles come into contact with seeds in the germination process, first translocation may realize on surface of radicle.

Plants exposed to nanoparticles can accumulate nanoparticles in their roots and can translocate these nanoparticles to other parts such as leaves, seeds or flowers. The first shoot which grows from seed is called as plumule. Nanoparticles may transportation from root to leaves and flowers via shoot. These accumulation and translocation factors depends on plant and nanoparticles type, exposure pathway and concentration, and agglomeration properties of nanoparticles [20]. Plumule and radicle is important for determination toxicity of nanoparticles so, the elongation of these parts were investigated in this study. Figure 3a and b present the effects of $nTiO_2Ag$, co-application of nZnO-$nTiO_2Ag$ and co-application of EDDS-$nTiO_2Ag$ on plumule and radicle elongation of rye. The plumule elongation increased with treatment of all test chemicals compared to control. The maximum plumule length was observed at concentration of 10 mg/L EDDS-50 mg/L $nTiO_2Ag$ as 10.29 cm, and the minimum data was obtained at concentration of 10 mg/L EDDS-200 mg/L $nTiO_2Ag$ as 6.08 cm. It was clear that EDDS and nZnO was more effective than $nTiO_2Ag$

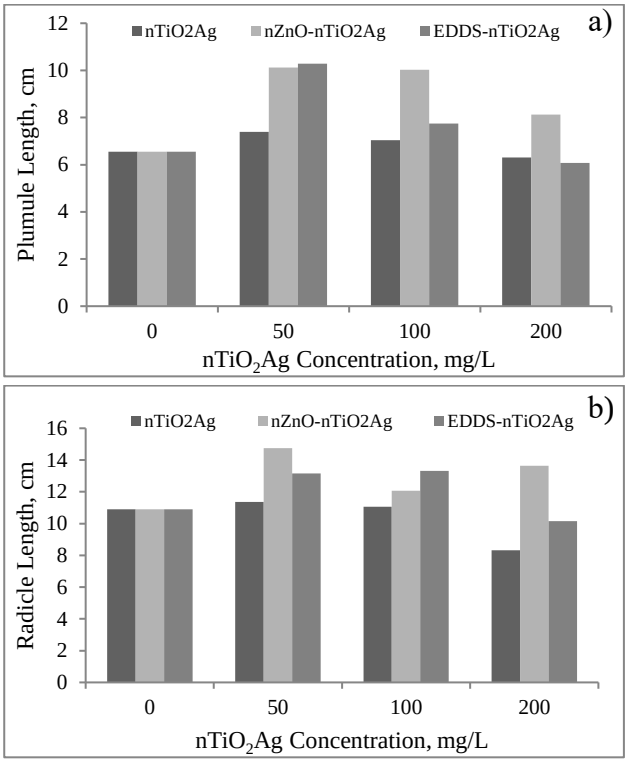

Figure 3. a)Plumule b)Radicles length of rye; test chemicals include 10 mg/L nZnO or 10 mg/L EDDS and different concentration $nTiO_2Ag$, control groups include only distilled water.

on plumule elongation of rye. On the other hand, the plumule elongation was more sensitive to co-application of EDDS-$nTiO_2Ag$ than co-application of nZnO-$nTiO_2Ag$, especially at high concentration. Yoon et al (2014) reported that the root and shoot length of soybean was inhibited by nZnO application as compared to control [21]. Figure 3b shows that the radicle elongation was increased nZnO-$nTiO_2Ag$ and EDDS-$nTiO_2Ag$ exposure at 50 and 100 mg/L concentration. At highest concentration $nTiO_2Ag$ (200 mg/L) and co-application of 10 mg/L EDDS-200 mg/L $nTiO_2Ag$ inhibited the radicle elongation of rye. The maximum radicle length was measured at concentration of 10 mg/L nZnO-50 mg/L $nTiO_2Ag$ co-application as 14.76 cm and the minimum length was measured at concentration of 200 mg/L $nTiO_2Ag$ as 8.31 cm, as Ghosh et al., (2010). The authors reported that 6 mM $nTiO_2$ reduced the root elongation of onion [22]. In Figure 3b, it is clear that the co-application process (nZnO-$nTiO_2Ag$ and EDDS-$nTiO_2Ag$) has positive impact on radicle elongation.

4. Conclusions

Last decades of nano-toxicology research has been increased in the literature. Metallic (e.g. ZnO, TiO_2, TiO_2Ag) nanoparticles are test materials which commonly used for determining and better understanding the nano-toxicity mechanisms. Today, a substantial amount of nanoparticles release inevitably into the environment and cause soil, air, and water pollution.

Plants are the most important component between soil and nanoparticles. Seed coat is the most important part of the seed germination. Its semipermeable structure allows or not allows nanoparticles to pass through the seed coat. If the nanoparticles pass through the coat, toxic effects may occur in the seed germination stage. If the nanoparticles cannot pass through the coat, the toxic effects may occur in the seedling stage. In this study, we evaluated that the effects of co-application of nZnO-$nTiO_2Ag$ and co-application of EDDS-$nTiO_2Ag$ on seed germination, seedling vigor index and plumule and radicle elongation of rye. We determined the nZnO promoted the seed germination, seedling vigor index and radicle-plumule elongation especially at concentration of 10 mg/L nZnO-50 mg/L $nTiO_2Ag$.

Future studies should also need to clarify the nano-toxicology, possible uptake and translocation of nanoparticles by plants. The potential toxic effects of commonly used nanoparticles on human health, plants, and animals are still unknown. This and the other studies in the literature demonstrate that there is too little data about the fate and effects of nanoparticles in the environment and need for more research in this area.

This is the first report on the effect of co-application of nZnO-$nTiO_2Ag$ and co-application of EDDS-$nTiO_2Ag$ on rye seed germination, seedling vigor and plumule and radicle elongation.

References

1. Khan I., K. Saeed, and I. Khan, *Nanoparticles: Properties, applications and toxicities.* Arabian Journal of Chemistry, 2017. Article in press. https://doi.org/10.1016/j.arabjc.2017.05.011.
2. Servin A., W. Elmer, A. Mukherjee, R. Torre-Roche, H. Hamdi, J. C. White, and C. Dimkpa, *nanoscale micronutrients suppress disease*. VFRC Report 2015/2, Washington, D.C., USA.
3. Siddiqi K. S. and A. Husen, *Plant response to engineered metal oxide nanoparticles.* Nanoscale Research Letters, 2017. 12(92): p.1-18.
4. Narendhran S., P. Rajiv, and R. Sivaraj, *influence of zinc oxide nanoparticles on growth of sesamum indicum L. In Zinc Deficient Soil.* International Journal of Pharmacy and Pharmaceutical Sciences, 2016. 8(3):p.365-371.
5. Savithramma N., S. Ankanna and G. Bhumi, *Effect of nanoparticles on seed germination and seedling growth of boswellia ovalifoliolata – an endemic and endangered medicinal tree taxon.* Nano Vision, 2012. 2(1,2&3): p.61-68.
6. Thul S.T. and B.K. Sarangi, *Implications of nanotechnology on plant productivity and its rhizospheric environment.* In: Siddiqui M. H. et al (eds) Nanotechnology and plant sciences. Springer, Cham 2015. p 37–53.
7. Cai F., X. Wu, H. Zhang, X. Shen, M. Zhang, W. Chen, Q. Gao, J.C. White, S. Tao, and X. Wang, *Impact of TiO2 nanoparticles on lead uptake and bioaccumulation in rice (Oryza sativa L.).* NanoImpact, 2017. 5: p. 101–108.
8. Doğaroğlu Z.G. and N. Köleli, *TiO_2 and ZnO nanoparticles toxicity in barley (Hordeum vulgare L.).*

Clean – Soil, Air, Water, 2017. 45: p. 1-7.

9. Tolaymat T., A. Genaidy, W. Abdelraheem, D. Dionysiou, and C. Andersen, *The effects of metallic engineered nanoparticles upon plant systems: An analytic examination of scientific evidence.* Science of the Total Environment, 2017. 579: p.93–106.
10. Durán N., P.D. Marcato, R. Conti, O. L. Alves, F. T. M. Costa, and M. Brocchi, *Potential use of silver nanoparticles on pathogenic bacteria, their toxicity and possible mechanisms of action.* J. Braz. Chem. Soc., 2010. 21(6): p. 949-959.
11. Doğaroğlu, Z.G. and N. Köleli, *Titanyum Dioksit ve Titanyum Dioksit-Gümüş Nanopartiküllerinin Marul (Lactuca sativa) Tohumunun Çimlenmesine Etkisi.* Çukurova University Journal of the Faculty of Engineering and Architecture, 2016. 31: p.193-198.
12. Jain N., A. Bhargava, V. Pareek, M. S. Akhtar, and J. Panwar, *Does seed size and surface anatomy play role in combating phytotoxicity of nanoparticles?.* Ecotoxicology, 2017. 26: p.238–249.
13. Miralles, P., T.L. Church, and A.T. Harris, *Toxicity, uptake, and translocation of engineered nanomaterials in vascular plants*. Environ. Sci. Technol., 2012. 46 (17): p.9224-9239.
14. Mahmoodzadeh H., M. Nabavi, and H. Kashefi, *Effect of nanoscale titanium dioxide particles on the germination and growth of canola (Brassica napus).* J Ornamental Hortic Plants, 2013. 3: p. 25–32.
15. Afrakhteh, S., E. Frahmandfar, A. Hamidi, H.D. Ramandi, *Evaluation of growth characteristics and seedling vigor in two cultivars of soybean dried under different temperature and fluidized bed dryer*. International Journal of Agriculture and Crop Sciences, 2013. 5(21): p.2537-2544.
16. Prasad T.N.V.K.V., P. Sudhakar, Y. Sreenivasulu, P. Latha, V. Munaswamy, K.R. Reddy, T.S. Sreeprasad, P.R. Sajanlal, and T. Pradeep, *Effect of nanoscale zinc oxide particles on the germination, growth and yield of peanut*. Journal of Plant Nutrition, 2012. 35(6): p. 905-927.
17. Khot L.R., S. Sankaran, J.M. Maja, R. Ehsani, and E.W. Schuster, *Applications of nanomaterials in agricultural production and crop protection: A review*. Crop Protection, 2012. 35: p.64-70.
18. El-Temsah Y.S., and E.J. Joner, *Impact of Fe and Ag nanoparticles on seedgermination and differences in bioavailability during exposure in aqueoussuspension and soil*. Environ. Toxicol., 2012. 27: p. 42–49.
19. Xiang L., H.-M. Zhao, Y.-W. Li, X.-P. Huang, X.-L. Wu, T. Zhai, Y. Yuan, Q.-Y. Cai, and C.-H. Mo, *Effects of the size and morphology of zinc oxide nanoparticles on the germination of Chinese cabbage seed*. Environmental Science and Pollution Research, 2015. 22(14): p. 10452–10462.
20. Rizwan M., S. Ali, M.F. Qayyum, Y.S. Ok, M. Adrees, M. Ibrahim, M. Zia-ur-Rehmand, M. Faride, and F. Abbas, *Effect of metal and metal oxide nanoparticles on growth andphysiology of globally important food crops: A critical revie.* Journal of Hazardous Materials, 2017. 322: p. 2–16.
21. Yoon S.J., J.I. Kwak, W.M. Lee, P.A. Holden, and Y.J. An, *Zinc oxide nanoparticlesdelay soybean development: a standard soil microcosm study*. Ecotoxicol. Environ. Saf., 2014. 100: p.131–137.
22. Ghosh M**.**, M**.** Bandyopadhyay, and A. Mukherjee, *Genotoxicity of titanium dioxide (TiO_2) nanoparticles at two trophic levels:plant and human lymphocytes*. Chemosphere, 2010. 81: p. 1253–1262.

Available online at www.dergipark.gov.tr

INTERNATIONAL ADVANCED RESEARCHES
and
ENGINEERING JOURNAL

Journal homepage: www.dergipark.gov.tr/iarej

e-ISSN: 2618-575X

International
Open Access

Volume 02
Issue 01

April, 2018

Research Article

Numerical investigation of combined effect of nanofluids and impinging jets on heated surface

Mustafa Kilic[a]*, Mahmut Yavuz[a], İbrahim Halil Yılmaz[b]

[a]*Department of Mechanical Engineering, Adana Science and Technology University, Adana, 01250, Turkey*
[b]*Department of Automotive Engineering, Adana Science and Technology University, Adana, 01250, Turkey*

ARTICLE INFO

Article history:
Received 02 March 2018
Revised 10 March 2018
Accepted 12 March 2018

Keywords:
Heat transfer
Multiple impinging jets
Nanofluids

ABSTRACT

Present study is focused on numerical investigation of heat transfer and fluid flow from a heated surface by using nanofluids and impinging jets. Effects of Reynolds number, different particle diameter and different types of nanofluids (TiO_2-water, CuO-water, NiO-water) on heat transfer and fluid flow were studied numerically. TiO_2-water nanofluid was used as a base coolant. Three impinging jets were used to cool the surface. It is obtained that increasing jet velocities from Ren/Re1=1-1.33-1.67 to Ren/Re1=1-1.20-1.40 causes an increase of 49.9% on average Nusselt number (ANN) but increasing jet velocities from Ren/Re1=1-1.20-1.40 to Ren/Re1=1-1.17-1.33 causes a decrease of 4.6% on ANN. Particle diameter from Dp=80nm to 10nm causes an increase of 2.9% on ANN. Using NiO-Water nanofluid causes an increase of 1% on ANN with respect to CuO and 2.8% with respect to TiO_2-water. Low Re k-ε turbulent model of PHOENICS CFD code was used for numerical analysis. Numerical results show a good approximation to experimental results.

1. Introduction

The jet cooling technique provides an important enhancement in heat transfer. Impinging jet technique can be used to boost up heating, cooling or drying processes on a selected surface. Impinging jets technic enhance heat transfer by increasing local heat transfer coefficient between the impinged fluid and a selected surface.

Suspension of solid particles which have 1-100 nm size in a base fluid called as nanofluid. Nanoparticles suspended in base fluid can expand thermal capacity of the fluid and also interactions and collisions between nanoparticles cause to increase in turbulence and turbulence intensity of the transition surface. Nanoparticles have 20% of their atoms on the particle surface, making them ready to heat transfer with high heat transfer coefficient. Nanoparticles provide another advantage which called as the particle mobility to nanofluids. Particle mobility causes micro-convection in the liquid due to its nano size and therefore increases heat transfer. Hence, they have a wide range of application in industry as microelectronics medicine and space research. Combination of the liquid jet impingement and the nanofluid technologies provides advantages of both and consequently improves the heat transfer significantly. This improvement means compact size and low weight which reduces the cooling system capital cost.

Many studies on nanofluid or impinging jet, can be found in the literature. Cakır M.T. [1] experimentally examined the thermal performance of the thermosiphon-type heat pipe which is using nanofluid as a working fluid. The nanofluid contained 2% by volume Al_2O_3. As a result, significant reduce on thermal resistance is obtained but a complete stabilization at thermal efficiency could not be provided. Sun et al. [2] searched the effect of a single jet using CuO nanofluid for heat transfer. It has been determined that when the nanofluid is used, a significant increase in heat transfer can be achieved compare with water. When a circular nozzle is used, a higher heat transfer coefficient is obtained compared to a square shaped nozzle, and the highest heat transfer is obtained when the jet angle is 90º. Teamah et al. [3] examined the heat transfer and flow structure for a flat plate by numerically and experimentally with different Reynolds numbers (Re = 3000-32000) and nanofluid volume ratios

* Corresponding author. Tel.: *+90 (322) 455 0000 - 2140*
E-mail address: mkilic@adanabtu.edu.tr
Note: This study was presented at International Advanced Researches and Engineering Congress 2017 (IAREC'17)

(φ= 0-10%) by using Al_2O_3 nanofluid. It has been observed that as volume fraction of nanoparticles in the fluid are increased, the heat transfer from the surface increases. Heat transfer coefficient can be increased by 62% when compared with the water. Qu et al. [4] Used Al2O3-water as working nanofluid in their experiment to investigate the thermal performance of a closed-loop vibrating heat pipe. As a result, they observed that the thermal resistance of the system decreased by 32.5% compared to pure water. Chien et al. [5] experimentally observed the application of nanofluid in the flat plate heat pipe. It was acquired that the use of nanofluid achieve 40% reduction in thermal resistance compared to pure water utilization. Kang et al. [6] determined that, when nanofluid which include 10 nm and 35 nm sized Ag nanoparticles is used, thermal resistance diminished by 50% and 80% compared to pure water respectively. Xuan and Li [7]. Prepared nanofluid that include Cu and they investigated heat transfer effect of nanoparticle volume fraction, heat transfer effect of particle diameter and heat transfer effect of particle geometry. As a result; it has been found that an increase of from 2.5% to 7.5% in the volumetric range causes an increase in the coefficient of thermal conductivity of nanofluid from 1.24 to 1.78. Shang et al. [8] studied the heat transfer characteristics of a closed-loop vibrating heat pipe with Cu-water nanofluid. They obtained that compared with pure water, the heat transfer capacity of the system increased by 83% when nanofluid was used. Manay et al. [9] have compiled recent studies which focusing on using of nanofluids in microchannel. As a result, nanofluids using in microchannel increases heat transfer, but the presence of nanoparticles causes an increase in pressure loss. Naphon et al. [10] investigated the heat transfer between the nanofluids that they built using titanium-ethanol and the closed two-phase thermosiphon. An increase of 10.6% on heat transfer was obtained by using nanoparticles, compared to ethanol using. Kilic et al. [11] examined the cooling of a flat plate by using impinging fluid air jet. It was observed that the mean Nusselt number increases by 49.5% when Reynold numbers is between 4000 and 10000. There are also some studies about alternative energy resources of [14-16]. As seen from literature there are some studies about impinging jets and nanofluids separately but researches of enhancing heat transfer by using nanofluids and impinging jets are required.

2. Numerical Model

Low Re k-ε turbulence model of PHOENICS CFD code was used for this numerical analysis. CFD simulation domain is shown in Figure1. Mesh structure is shown in Figure2.

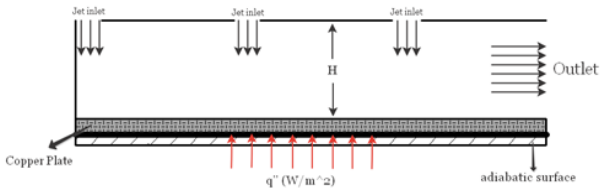

Figure 1. CFD simulation domain

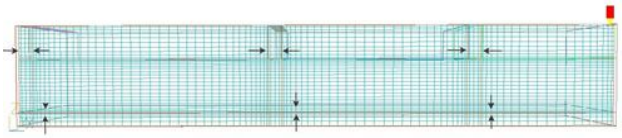

Figure. 2. Mesh structure

The continuity, Reynolds averaged momentum and time averaged energy equations governing 3-dimensional steady, flow of air with constant properties used for turbulent solutions can be written in the Cartesian coordinate system as follows:

Continuity equation:

$$\frac{\partial U_i}{\partial x_i} = 0 \tag{1}$$

Momentum equation:

$$\rho U_i \frac{\partial U_j}{\partial x_i} = -\frac{\partial P}{\partial x_j} + \frac{\partial}{\partial x_i}\left[\mu\left(\frac{\partial U_i}{\partial x_j} + \frac{\partial U_j}{\partial x_i}\right) - \rho\overline{u_i' u_j'}\right] \tag{2}$$

Energy equation:

$$\rho c_p U_i \frac{\partial T}{\partial x_i} = \frac{\partial}{\partial x_i}\left[k\frac{\partial T}{\partial x_i} - \rho c_p \overline{u_i' T'}\right] \tag{3}$$

All the boundary conditions used in the study are summarized in Table 1.

Table 1. Boundary Conditions

	U (m/s)	V (m/s)	W (m/s)	T (°C)	k	ε
$W_{jet,inlet}$ (W_1,W_2,W_3)	U=0	V=0	W= W inlet	$T=T_{inlet}$	$(T_i W_{jet})^2$	$(C_\mu C_d)^{3/4}\frac{k^{3/2}}{L}$
Cu Plate	U=0	V=0	W=0	$q''=q_{inlet}$	k=0	$\frac{\partial \varepsilon}{\partial z}=0$
Outlet	$\frac{\partial U}{\partial x}=0$	$\frac{\partial V}{\partial x}=0$	$\frac{\partial W}{\partial x}=0$	$T=T_{out}$	$\frac{\partial k}{\partial x}=0$	$\frac{\partial \varepsilon}{\partial x}=0$
Front and Back wall	U=0	V=0	W=0	$\frac{\partial T}{\partial y}=0$	-	-
Top wall	U=0	V=0	W=0	$\frac{\partial U}{\partial z}=0$	-	-

It was used 96x15x34 (48960 elements) mashes for this application. Mesh structure was prepared according to flow conditions. In order to get more precise numerical results, we intensified mesh numbers in some region as jet inlet, surface of copper plate. Sweep number was studied between 400 and 2500 and cell number was also studied between 24 and 44. It is observed that numerical geometry was independent from sweep number and cell

number when sweep number was 600 and cell number was 96x15x34. Verification of this modal with experimental results of Kilic [12] was shown in Figure3.

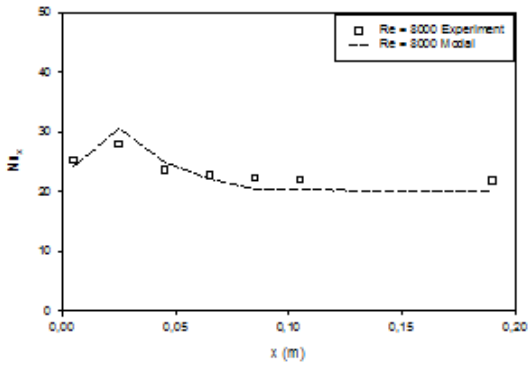

Figure 3. Verification of modal with experimental result

3. Date Reduction

The heat transfer from the surface will take place by convection, conduction and radiation.

$$Q_{convection} = Q_{total} - Q_{conduction} - Q_{radiation} \quad (4)$$

The total amount of heat to be given to the plate is;

$$Q_{total} = \frac{V^2}{R} \quad (5)$$

Where V is the voltage value of the power unit and R is the resistance of the heater. Here, the heat generated by the heater placed under the copper plate will be transmitted to the upper surface of the plate through the copper plate thickness by conduction, and as a result, the plate surface will be cooled by using nanofluid with impinging jet. Heat transfer by conduction along the plate

$$Q_{conduction} = \frac{-k_c.A_c.(T_{bottom} - T_{upper})}{L_c} \quad (6)$$

here, kc is the heat transfer coefficient of the copper plate, Ac is the copper plate surface area, and Lc is the copper plate thickness.

Thermal loses due to radiation;

$$Q_{radiaton} = \varepsilon.\sigma.A.F.(T_s^{\,4} - T_{bulk}^{\,4}) \quad (7)$$

Where ε is the copper plate emissivity, σ is the Stefan Boltzmann constant, A is the radiation surface area, T_s is the surface temperature, and T_{bulk} is the mean fluid temperature.

$$T_{bulk} = \frac{T_{in} + T_{out}}{2} \quad (6)$$

It is assumed that heat transfer with radiation is negligible in this study because surface temperature is under 573.15 K.

Heat transfer from surface with convection;

$$Q_{convection} = h.A.\Delta T \quad (7)$$

Where h is the heat transfer coefficient, A is the convection surface area, ΔT ($\Delta T = T_s - T_{bulk}$) is the difference between the measured surface temperature and the fluid mean temperature.

Nusselt number (Nu) is a dimensionless parameter indicating the ratio of heat transfer with conduction to h eat transfer with convection.

$$Nu = \frac{(Q_{convection}.D_h)}{(T_s - T_{jet}).k_{nf}} \quad (8)$$

Where T_s is the measured surface temperature, D_h is the hydraulic diameter, and k_{nf} is the coefficient of thermal conductivity of the nanofluid. Reynolds number (Re) is used to determine for forced convection whether the flow is laminar or turbulent. Reynolds number based on turbulent flow;

$$\mathrm{Re} = \frac{(\rho_{nf}.V_{jet}.D_h)}{(\mu_{nf})} \quad (9)$$

Where ρ_{nf} is the nanofluid density, V_{jet} is the jet velocity, and μ_{nf} is the nanofluid dynamic viscosity. The density of nanofluids is;

$$\rho_{nf} = (1-\varphi).\rho_{bf} + \varphi.\rho_p \quad (10)$$

Where ρ_{bf} is the base fluid (water) density, φ is the volumetric ratio of the nanofluid, and ρ_p is the density of the solid particles in the nanofluid. The volumetric ratio of nanoparticles is;

$$\varphi = \frac{1}{(1/\omega).(\rho_p - \rho_{bf})} \quad (11)$$

Where ω is the density difference between the fluid and the main fluid (water). The nanofluid specific heat is calculated from;

$$C_{p_{nf}} = \frac{\varphi.(\rho.C_p)_p + (1-\varphi).(\rho.C_p)_f}{(\rho_{nf})} \quad (12)$$

Where $Cp_{(p)}$ is specific heat of particle, $Cp_{(f)}$ is specific heat of base fluid. The effective thermal conductivity of nanofluid is calculated according to Corcione [13];

$$\frac{k_{eff}}{k_f} = 1 + 4.4\,\mathrm{Re}^{0.4}\,\mathrm{Pr}^{0.66}\left(\frac{T}{T_{fr}}\right)^{10}\left(\frac{k_p}{k_f}\right)^{0.03}\varphi^{0.66} \quad (13)$$

Where Re is the nanoparticle Reynolds number, Pr is the Prandtl number of the base liquid. k_p is the nanoparticle thermal conductivity, φ is the volume fraction of the suspended nanoparticles, T is the nanofluid temperature (K), T_{fr} is the freezing point of the base liquid.

Nanoparticle Reynolds number is defined as;

$$Re = \frac{2\rho_f k_b T}{\pi \mu_f{}^2 d_p} \quad (14)$$

Kb is the Boltzmann's constant. The effective dynamic viscosity of nanofluid;

$$\mu_{nf} = \mu_{bf}\,(1 + 2{,}5\,\varphi + 4{,}698\,\varphi^2) \quad (15)$$

4. Results and Discussions

In this section, numerical results were prepared for three parameters.

1) Effects of different Reynolds number rate for Rn/R1=1-1.33-1.67 to 1-1.17-1.33
2) Effects of TiO_2-water nanofluid with 25 nm sized particles for different particle diameter on heat transfer (D_p=10, D_p=25, D_p=40, D_p=80).
3) Effects of different nanofluids on heat transfer (TiO_2-water, Cu-Water, NiO-water).

Effects of variant Reynolds number

Numerical analysis was conducted for different water flow regime for Rn/R1=1-1.33-1.67 to 1-1.17-1.33 when particle diameter was 25μm and inlet temperature T_{inlet}= 20 ºC.

Table 2. Reynolds Numbers

	W_1(m/sn)	W_2(m/sn)	W_3(m/sn)	Re_1(jet-1)	Re_2(jet-2)	Re_3(jet-3)	Re_1/Re_1	Re_2/Re_1	Re_3/Re_1
1.phase	6	8	10	21440,42	28587,23	35734,03	1	1,33	1,67
2.phase	8	10	12	28587,23	35734,03	42880,84	1	1,25	1,5
3.phase	10	12	14	35734,03	42880,84	50027,65	1	1,2	1,4
4.phase	12	14	16	42880,84	50027,65	57174,46	1	1,17	1,33

Velocity vectors and Temperature contours for different Reynolds numbers are shown in Figure4 and Figure5.

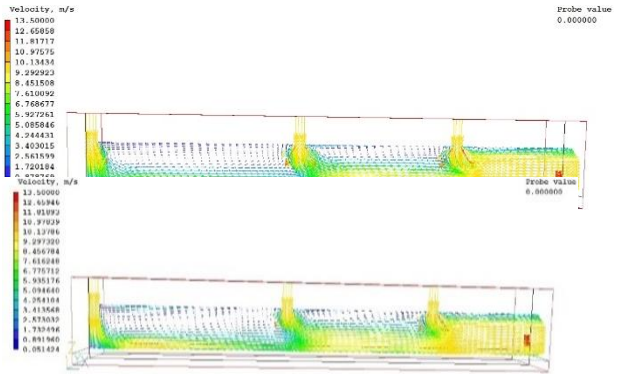

Figure 4. Velocity vectors for different Reynolds number (a) Rn/R_1=1-1.2-1.4 (b) Rn/R_1=1-1.17-1.33

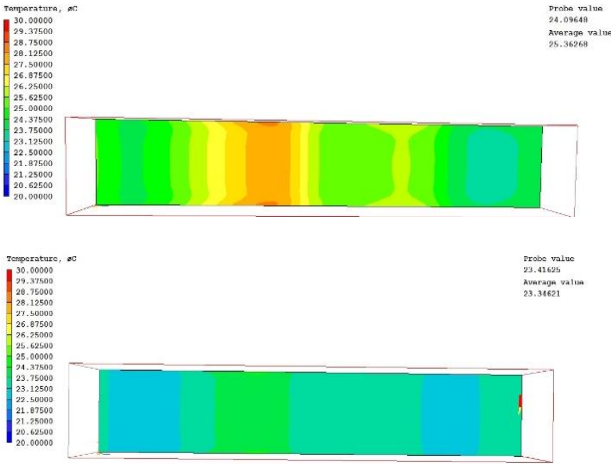

Figure 5. Temperature contours for (a) R_n/R_1=1-1.33-1.67 (b) R_n/R_1=1-1.2-1.4

It can be seen that increasing jet velocities from the first phase to the third phase local surface temperature decreases and local Nusselt number increases. But increasing jet velocities to the fourth phase causes an increase on surface temperature. The reason of this is that vortexes, which occurs at the bottom of the close side, enlarge while velocity on the first jet is increasing. And these vortexes reduce impinging effects and causes an increase on surface temperature and decrease on local Nusselt number. These effects continue at impinging region of second jet but effects of channel flow increases at this region. At the impinging region of the third jet there is not a significant difference between third and fourth phase because channel flow effects reduces impinging effects at this region by increasing velocities from third to fourth phase. So increasing jet velocities from the first phase to the third phase causes an increase of 49.9% on average Nusselt number but increasing jet velocities from the third phase to the fourth phase causes a decrease of 4.6% on ANN because of the effects of vortexes and the best velocity profile is the third phase. Local Nusselt number for different jet velocities are shown in Figure6

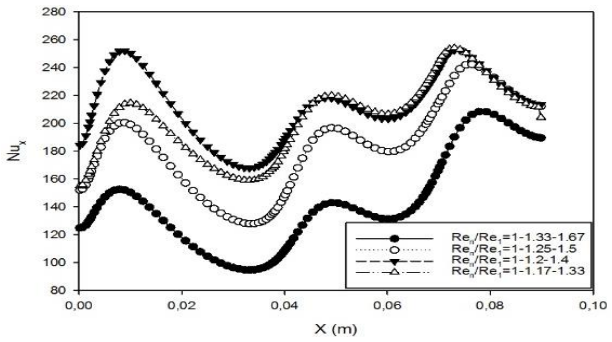

Figure 6. Local Nusselt number for different jet velocities

Effects of different nanoparticle diameters

Effect of different particle diameter (D_p=10, 25, 40, 80 nm) was analyzed numerically. It was observed that decreasing particle diameter from 80nm to 10nm causes a decrease on a surface temperature. Decreasing particle diameter from D_p=80nm to 10nm causes an increases of 2.9% between on ANN. These increase occurs 2.1% between D_p=40nm to 10nm. So increasing particle diameter from D_p=80nm to 40nm causes a slight decrease on ANN. So decreasing particle diameter causes an increase on ANN. Temperature contours on heated surface for different particle diameter are shown in Figure7.

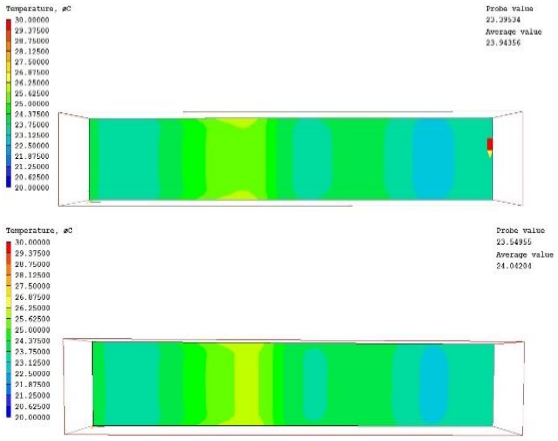

Figure 7. Temperature contours on surface for (a)D_p=10nm and (b)D_p=80nm

Variation of local Nusselt number for different particle diameter is shown in Figure8.

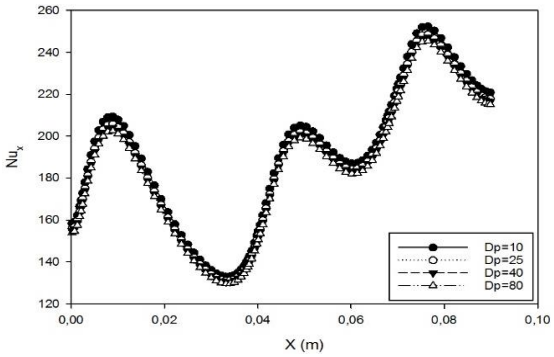

Figure 8. Local Nusselt number for different particle diameters.

Effects of different type of nanofluids

Numerical analysis is conducted for different type of nanofluids (CuO-water, TiO_2-water and NiO-water) with 25 nm particle size and volume fraction 2%. Calculated properties of nanofluids are shown in Table 2. Local Nusselt numbers on surface of heated place is shown in Figure9. For TiO_2-water, CuO-water and NiO-water. It was obtained that using NiO-Water nanofluid causes an increase of 1% on ANN with respect to CuO-Water and 2.8% with respect to TiO_2-water.

Table 3. Thermophysical properties of nanofluids at 293K

Nanofluid	Density (kg/m^3)	Specific heat (J/kgK)	Kinematic viscosity (m^2/s)	Thermal conductivity (W/mK)	Thermal expansion coefficient (1/K)
TiO_2-Water	1063.2	3902.5	0.000000982	0.6378	0.0001537
CuO-Water	1108.3	3754.3	0.000000943	0.6382	0.0001534
NiO-Water	1114.5	3744.6	0.000000937	0.6394	0.0001532

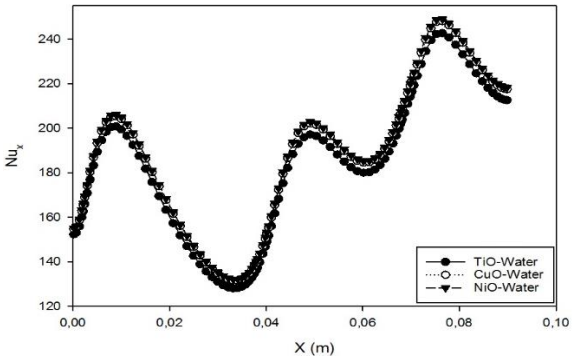

Figure 9. Local Nusselt number for different nanofluid

5. Conclusions

Present study is focused on numerical investigation of heat enhancement and fluid flow from a heated surface by using nanofluids and impinging jets. Effects of different Reynolds numbers, particle diameter and different types of nanofluids (TiO_2-water, CuO-water, NiO-water) on heat transfer and fluid flow were studied numerically. According to our constraints it is obtained that increasing jet velocities from the first phase to the third phase causes an increase of 49.9% on ANN but increasing jet velocities from the third phase to the fourth phase causes a decrease of 4.6% on ANN. Decreasing particle diameter from D_p=80nm to 10nm causes an increases of 2.9% between on ANN. These increase occurs 2.1% between D_p=40nm to 10nm. Using NiO-Water nanofluid causes an increase of 1% on ANN with respect to CuO and 2.8% with respect to TiO_2-water. Velocity of the third phase, D_p=10 nm and using NiO-water nanofluid shows better heat transfer performance. Research areas for future investigations can be investigation of effect of hybrid nanofluids with different base fluids on heat transfer with impinging jet geometry.

Acknowledgment

This work supported by the Adana Science and Technology University under Research Project (project no:16103021), Turkey.

Nomenclature

CP : Specific Heat (J/kgK)
ρ : Density(kg/m3)
φ : Nanoparticle volume fraction
μ : Dynamic viscosity(Pa.s)
Pr : Prandtl Number
Re :Reynolds Number
Nu_X : Local Nusselt number
k_{eff} :Effective Thermal Conductivity

References

1. Cakır, M.T, *Alamüna içeren Nanoakışkan kullanarak ısı borularının performanslarının iyileştirilmesi*, Journal of The Faculty of Engineering and Architecture of Gazi University, 2015. **30**: p.547-556.
2. Sun, B., Qu, Y., Yang, D., *Heat transfer of Single Impinging jet with Cu nonofluids*, Applied Thermal Engineering, 2016.**102**: p.701-707.
3. Teamah, M.A., Dawood M.M., Shehata A., *Numerical and experimental investigation of flow structure and behavior of nanofluids flow impingement on horizontal flat plate*, Experimental Thermal and Fluid Science, 2016. **74**: p.235-246.
4. Qu j., Wu H.Y., Cheng P.,*Thermal performance of an oscillating heat pipe with Al_2O_3-water nanofluids*, International Communication Heat and Mass Transfer, , 2010. **37**:p.111-115.
5. Chien, H.T., Tsia C.Y., Chen P.H., Chen P.Y., *Improvement on thermal performance of a disck-shape miniature heat pipe with nanofluid*, Proceedings of the fifth International Conference on Electric Packaging Technology, 2003,**17**:p.389-391.
6. Kang S.W.,Wei,W.C., Tsia S.H., Yang S.H., *Experimental Investigation of silver nano-Fluid on heat pipe thermal performance*, Applied Thermal Engineering, 2006. **26**: p.2377-2382.
7. Xuan Y., Li Q., *Heat transfer enhancement of nanofluids*, Int.Journal of Heat and Flouid Flow, 2000. **21**:pp.58-64.
8. Shang F.M., Liu D.Y., Xian H.Z., Yang Y.P., Du X.Z., *Flow and heat transfer characteristics of different forms of nanaometer particles in oscillating heat pipe*, Journal of Chemical Industry, 2007. **58**: p.2200-2204.
9. Manay E., Sahin B., Akyurek E.F., Comakli O. *Mikro kanallarda nanaoakışkanalrın kullanımı,* TMMOB MMO Mühendis ve Makina Dergisi, 2012. **53**: p.38-42.
10. Naphon P., Asssdamongkol P., Borirak T., *Experimental investigation of titanium nanofluids on the heat pipe thermal efficiency*, International Communication Heat and Mass Transfer, 2008. **35**: p.1316-1319.
11. Kilic, M., Çalışır, T., Başkaya, Ş, *Experimental and numerical study of heat transfer from a heated flat plate in a rectangular channel with an impinging Jet*, Journal of the Brazilian Society of Mechanical Sciences and Engineering, 2016**. 48**, p.1-16.
12. Kilic M., *Experimental and numerical study of heat transfer fro a heated flat plate in a rectangular channel with an impinging Jet*, PhD Thesis, Graduate School of Natural and Applied Science, Gazi Unıversity, Turkiye, Oct. 2013.
13. Corcione M., *Empirical correlating equations for predicting te effective thermal conductivity and dynamic viscosity of nanofluids.Energy Convers*. *Manag*, 2011. **52**(1), p.789-793.
14. Abdulvahitoğlu A, Evaluation of the fuel quality values of bay laurel ol as a biodiesel feedstock/title, Biofuels, 2018, **9**: p.95-100.
15. Abdulvahitoğlu A,Tüccar G., 2017, *Dizel Motorlarda Alternatif Yakıt Olarak Karpuz Çekirdeği Biyodizelinin Değerlendirilmesi,* Gazi Üniversitesi Mühendislik-Mimarlık Fakültesi Dergisi, 2017. **32**:p.211-216, 10.17341/gazimmfd.300610.
16. Abdulvahitoğlu A., Aydın K., *Performance and exhaust emission characteristics of a CI engine fueled with synthesized fuel blends*, Energy Education Science and Technology Part A: Energy Science and Research, 2012.**2**:p. 699-710.

Available online at www.dergipark.gov.tr

INTERNATIONAL ADVANCED RESEARCHES
and
ENGINEERING JOURNAL

Journal homepage: www.dergipark.gov.tr/iarej

e-ISSN: 2618-575X

International
Open Access

Volume 02
Issue 01

April, 2018

Research Article

Effect of Cu addition on microstructure and mechanical properties of NiTi based shape memory alloy

N. Arda Tanış[a], Hakan Gökmeşe[b]*, Bülent Bostan[c]

[a]*Kırıkkale University, Faculty of Engineering, Kırıkkale,Turkey*
[b]*Konya Necmettin Erbakan University, SeydisehirAhmet Cengiz Faculty of Engineering, Dept. of Metallurgy and Materials Eng. Seydisehir-Konya, Turkey.*
[c]*Gazi University, Faculty of Technology, Dept. of Metallurgy and Materials Eng. Ankara, Turkey*

ARTICLE INFO

Article history:
Received 25March 2018
Revised 07April 2018
Accepted 09April 2018

Keywords:
Multiphase microstructure,
NiTi alloy
Copper
Shape memory alloys

ABSTRACT

In this research paper, pre-alloyed NiTi based shape memory alloy and 4%Cu were used as starting powder materials. Starting powder materials were blended for 60 minutes by a turbula mixer. After mix processing, microstructure and phase transformations of powders were characterized using X-ray (XRD), elemental distribution spectrometry (EDS), scanning electron microscopy (SEM). Prepared powder mixtures as NiTi and NiTi+4%Cu alloys were pressed at 785MPa in a mold and then sintering process was applied to materials at different temperatures and time. Formation of multiphase's (Ni_3Ti, NiTi, Ti_2Ni, Ni_4Ti_3 and NiTiCu) and positive effects of Cu addition were obtained by sintering at different temperatures and time. And also, stabilized NiTi phase and increasing the value of micro hardness were determined with added 4%Cu powders.

1. Introduction

Shape memory alloys (SMA) have ability to return to a taught shape when applied to a proper thermo mechanical or magnetic variations. Due to unique and outstanding features of SMA, They have been used in most commercial applications in recent years which was supported by primary and practical investigation works [1].NiTi alloys consist of near-equatomic composition, exhibit shape memory, super elastic effects, which is commonly called Nitinol alloys. These alloys transform from austenite to martensite form by temperature and pressing effects. These could also be used as an implant material due to unique biocompatibility, corrosion resistance features and these materials nowadays play an important role in research laboratories [2-7].

NiTi alloys reversible and diffusionless transformation (martensite ↔ austenite) are coming about in the temperature range 50 to 100ºC as a function of Ni content of the matrix [8].

In NiTi binary balance systems, stable Ni-Ti phases appears in the region approximately equal percentage of NiTi [9,10]. NiTi alloys have exhibited poor mechanical properties and segregation problems in their molding process. For this reason, recently powder metallurgy method has attracted much attention for porous NiTi alloys [11,12]. However, Formed impurity increase in the manufacturing process by powder metallurgy technique should not been overlooked [13]. These negative effects could be solved with optimum sintering temperature and timesin the sintering atmosphere with controlled homogeneous atmosphere conditions which has an important place in production process [14-16].

In this study, Cu powders were added to the pre-alloyed NiTi alloy powders. The obtained experiment samples were sintered at different temperature and time conditions. Multiphase microstructures and increasing of the mechanical properties depending on sintering temperature and time were obtained with distribution of Cu contents in main phase

* Corresponding author. Tel.: +90-539-8761547; Fax: +90-332-5820450.
E-mail address: hgokmese@konya.edu.tr

2. Experimental Studies

NiTi pre-alloyed powders used in the experiments were produced by gas atomization technique and were obtained from Nanoval GmbH and Co.KG Company.The average grain size of nickel-rich pre-alloyed NiTi powders was 14µm .NiTi and 4% Cu powders were blended in a turbula mixer. And then blended powders were pressed in 10mm diameter spherical mold at 785MPa.The green parts were sintered at high purity argon gas atmosphere which was refined into hot copper chip (at 450ºC) to reduce oxidation and impurities. The schematic diagram of sintering stage under high purity argon atmosphere of NiTi and NiTi+%4Cu samples is shown in Fig 1. According to sintering diagrams (Figure 1), Pressed NiTi (14 µm) powder metal samples were sintered at 900ºC for 300 minute and 1050ºC for 60 minute. NiTi-4% Cu samples were sintered at 850ºC and 1000ºC for 60 minute and at 1050ºC for 300 minute (Figure 1).

After sintering process of samples, sanding, polishing and etching processes for metallographic investigations were applied to the sintered samples respectively. Etched samples were examined by optical microscope (LEICA) and scanning electron microscope (SEM). Also, electron distribution spectrometer (EDS) analyses were performed. XRD analyses was applied to the pre-alloyed powders and sintered parts for determine of phase transformations by APD 2000PRO version X-ray Diffractometer device. Hardness measurements (HV 0.5) of samples were performed by Shimadzu model micro hardnessdevice.

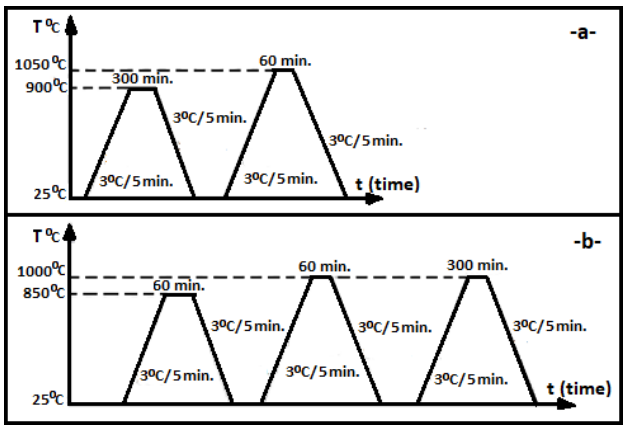

Figure 1. Sintering diagrams; a- NiTi samples, b- NiTi-4%Cu samples

3. Results and Discussion

Figure 2 shows SEM images of pre-alloyed NiTi powders (particle size-14µm) used in experiments. It could be identified to be uniform, spherical, pure and smooth surface structure of powders in Figure 2-a and b. This condition could be good affects on pressing ability and sintering behavior, as known [17]. The element distribution of powders (%55Ti, 45Ni and 49,9Ti, 50, 1%) is shown in Table 1 as weight and atomic ratio respectively.

DSC analysis was applied to pre-alloyed NiTi powders to determine of powder transformation temperatures (Figure 3). According to the DSC analysis in Figure 3, start and finish temperatures of powder austenitic transformations were determined at -15ºC and 4ºC respectively. XRD analysis of NiTi powders is given in Figure 4. According to X-ray diffraction (Figure 4), it was observed to exhibit only austenitic phase at ambient conditions of powders. When nickel intent increased above 50 at. %, the Af transformation temperature could be seen to decreased until - 40°C for 51 at. % nickel [18].

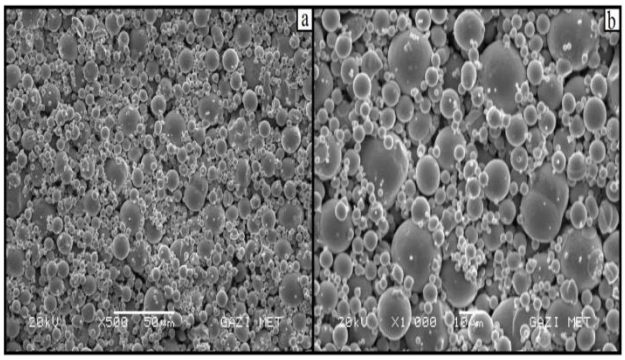

Figure 2. SEM images of pre-alloyed NiTi powders (particle size-14µm)

Table 1. The chemical composition of powders

Elements	Ti	Ni
Weight %	55	45
Atomic %	49.9	50.1

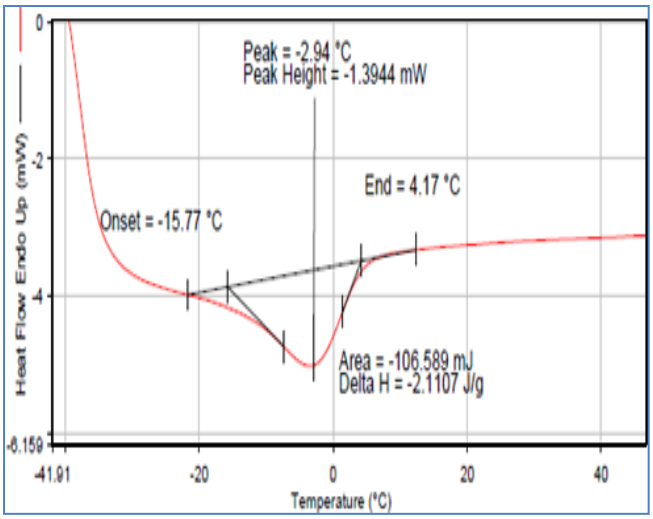

Figure 3. DSC analysis of powders

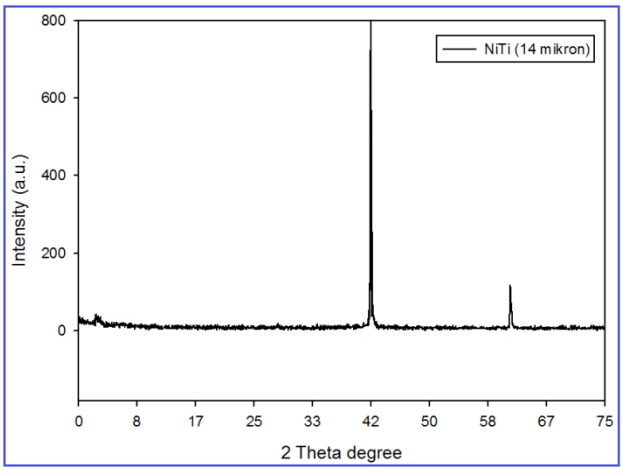

Figure 4. XRD analysis of NiTi powders

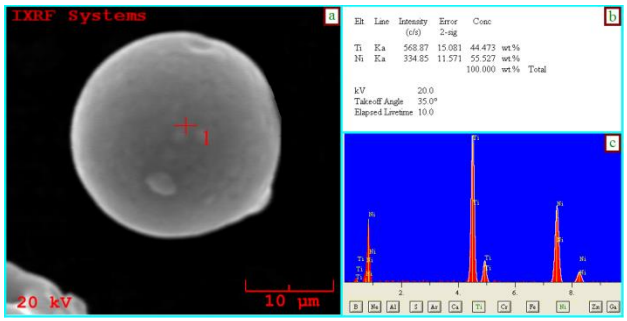

Figure 5.EDS analysis of NiTi powders; a-SEM image, b- wt.% elements dispersions, c- Ni and Ti peaks

In the present study, Ni content was only 50.1at. % (Table 1) and so the onset temperature could be decreased until -15ºC (Figure 3). The point EDS analysis on the SEM image of NiTi powder is given in Fig.5. According to EDS result in Fig.5, it was observed to be having only Ni and Ti content of powders with spherical and smooth surface characteristic. EDS analysis applied to powders supports XRD analysis and shows only austenitic phases in structure (Figure 5.b). Only Ti and Ni peaks were identified by EDS analyses in Figure 5-c. It was determined to belong to NiTi alloy of this peaks which define to B2austenitic phase (110, 200 and 211) [17].

Bulk density of pressed samples (NiTi powder) was measured approximately as 5 g/cm^3. Bulk density of NiTi samples added wt.4%Cu was measured as 5.21 g/cm^3. Density of NiTi samples added wt.4%Cu after sintering (850ºC-60 min.) was measured as 4.73 g/cm^3 (Figure 6). The value of increased density was measured as 5.063 g/cm^3 with increasing of the sintering temperature (1000ºC-60 min.). The value of density was determined as 5.235g/cm^3 after sintering process applied at 1000ºC for 300min in an another sample. The cause of the increased density value in samples could be considered as Cu powder content which affected to density of the structure with swelling effects at this temperature and then damping effects on the structure [19]. After sintering at 850ºC for 60 min., the hardness value of samples was measured as 532 HV, but increased with sintering temperature (1000ºC-60 min.) decreased hardness value and was measured as 523 HV, because of Cu contents swelling and damping effects. Increasing of the sintering time, increased the hardness value was measured as 730HVat 1000ºC for 300min. (Figure 6).

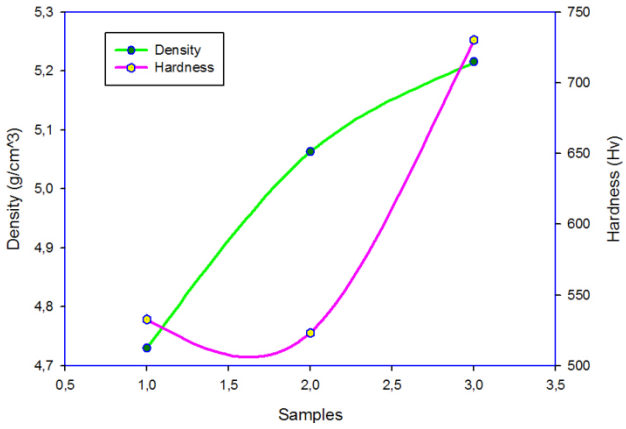

Figure 6. Density and hardness values of NiTi + 4%Cu samples after sintering; 1-850ºC-60 min., 2- 1000ºC-60 min., 3- 1000ºC-300 min.

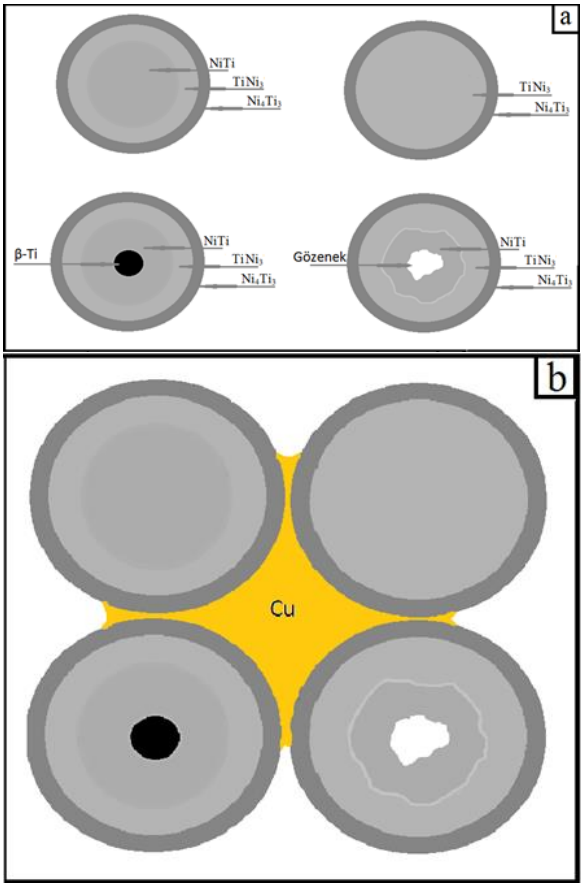

Figure 7. Illustration of the schematic phase occurred after sinter; a- Compounds, b- Shapes

Figure 7 shows schematic illustration of sintering process. When the schematic illustration was investigated, different multiphase structure was obtained with sintering process (as NiTi, $TiNi_3$, Ni_4Ti_3 and NiTiCu). Obtained phases in NiTi systems are recently illustrated with this type of schematic representation for clear expression [20,21].

Figure 8 shows XRD analysis of samples sintered at 1000ºC for 60 and 300 min. Intensity of Ni_3Ti phase in the XRD analysis (Figure 8) was obtained as the inner phase in NiTi phase structure with NiTi phase diagram (Figure 9). Table 2 shows phase ratio of NiTi + 4% Cu structure after sintering at 1000°C. Ni_3Ti ratio of samples sintered at 1000ºC for 60 min. and 300 min. was identified approximately 68% and 76% respectively. So it was determined that increasing Ni_3Ti ratio with increasing of sintering time (Table 2). This ratios and phases could be clearly observed in NiTi phase diagram (Figure 9) [22]. Ti_2Ni and Ni_3Ti formation were confirmed at slow cooling condition which used in this experiment. Gibbs energies of Ti_2Ni and Ni_3Ti phases are less thanNiTi phase and so it is difficult to obtain of only alone NiTi structure by solid – state diffusion [23, 24].

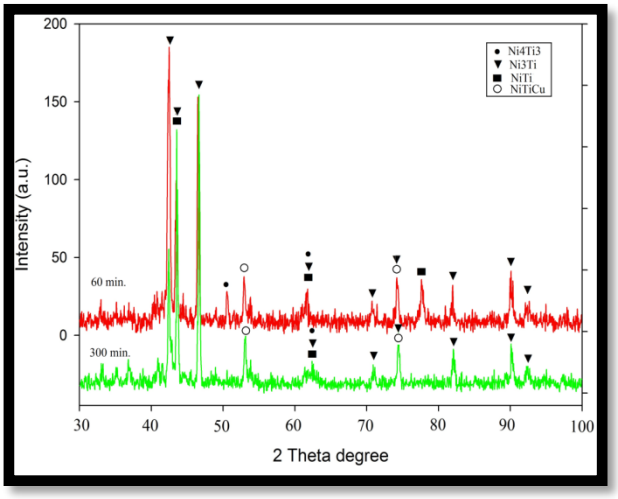

Figure 8. XRD analysis of NiTi+ 4% Cu structure after sintering at 1000°C

Table 2. Phase ratio of NiTi + 4% Cu structure after sintering at 1000°C

Sintering time (min.) at 1000°C	Phase rate (%)			
	NiTi	Ni_3Ti	Ni_4Ti_3	NiTiCu
60	20	68	10	2
300	16	76	6	2

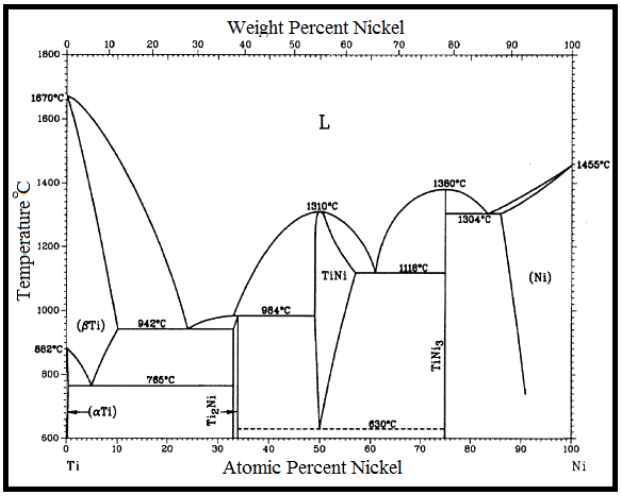

Figure 9. NiTi phase diagram (obtained of B_2 and Ti_3Ni_4phases) [25].

Figure 10-a and b illustrate microstructure of green pre-alloyed NiTi samples that sintered at 900ºC for 300 min. and 1050ºC for 60 min. When the microstructure images in Figure 10 were investigated, the change of the microstructure and phases with the effect of sintering temperature was observed. The appearance of liquid phase (Ti-$NiTi_2$ eutectic) with rising to 1050ºC of sintering temperature could be seen in Figure 9.

After sintering at 1050ºC, the appearance of liquid phase sintering (Ti-$NiTi_2$autectic) was identified with illustration of the schematic phase in Figure 7. As a result of this, It was expected to develop of a much more homogeneous microstructure with the disappearance of grain boundaries and diffusion towards the grain boundary of elements (Figure 10 b-d) [8].

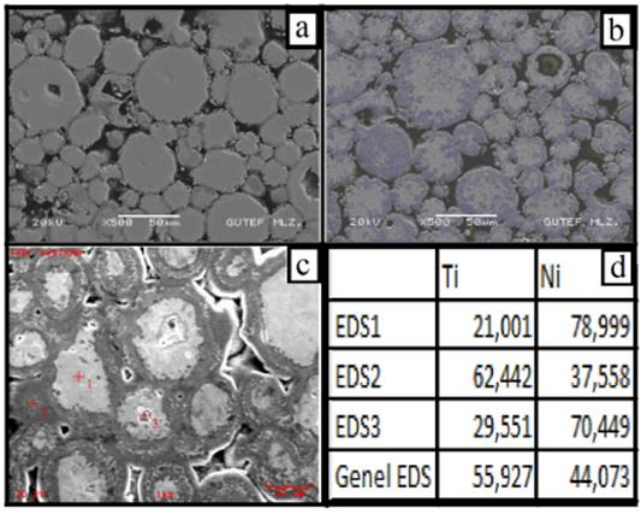

Figure 10. SEM images of pre-alloyed NiTi samples after sintering; a- 900°C-300 min., b- 1050°-60 min., c- EDS image (1050°C-60min.), d- Ni and Ti amounts

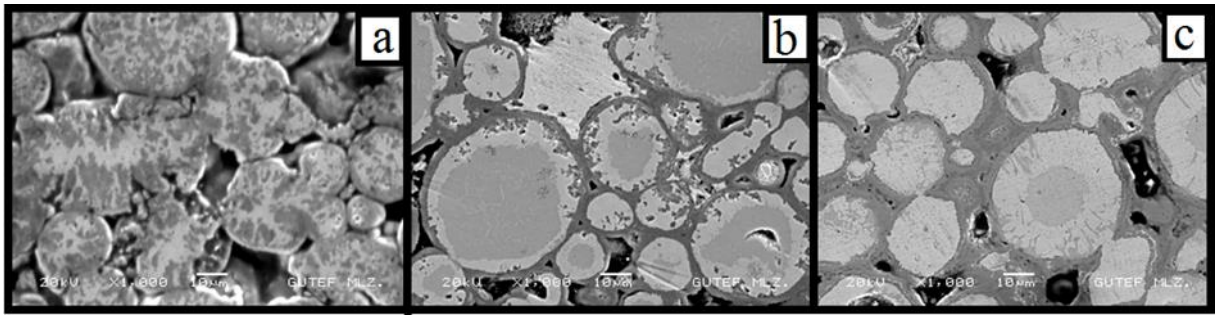

Figure 11. SEM images of sintered TiNi+%4Cu samples; a- 850°C-60min., b- 1000°C-60min., c- 1000°C-300min.

The formed multiphase structures ($TiNi_3$, NiTi, Ti_2Ni, Ni_4Ti_3) were determined after sintering at 1050ºC (Figure 10 c and d) [13]. The porosity was reduced with increasing of the sintering temperature to over of 1000ºC but was not removed under this temperature.

The reason for this situation, NiTi alloy exhibits an endothermic reaction at about 950°C (for ~ 49% NiTi alloy). Because of liquid phase sintering mechanism occur after 1020°C, endothermic reaction can become active (Figure 10 and 11) [26, 27]. In NiTi alloys, sintering temperature play an active role [28-31]. Sintering temperature after a certain point affects enhancing the mechanical properties and also could be seen to reduce the porosity[32]. Positive effects increased mechanical properties were obtained by multiphase structures of NiTiintermetallics formed by the addition of wt.4%Cu content [33]. Multiphase structures (as Ni_4Ti_3 phases) were obtained by Cu addition to sintered samples (NiTi) which was seen in figure 10 c and d. The obtained NiTi-4%Cu samples were sintered at 850ºC for 60 minute, 1000ºC for 60 and 300 minutes respectively (Figure 11 a-c).

The homogeneous and purity microstructure with increasing of sintering time in Figure 11-c were achieved. The dissolution of Cu in microstructure was affected directly by sintering time which could be seen in Figure 11 b, c and other literature investigations [34]. For determining the element distribution amount of the resultant multiphase structure, EDS analyses were applied to sintered parts at 850ºC and 1000ºC for 60 minutes and at 1000ºC for 300 minutes (Figure 12, 13 and 14).

When EDS analyses were examined, same compounds ($TiNi_3$, NiTi, Ti_2Ni, Ni_4Ti_3 and NiTiCu) and elements distribution ratio could be seen in XRD analyses (Figure 8). Obtained multiphase structures were directly affected the phase transformations. Previously several studies on NiTi alloys (wt. 49-51% Ni) show B2—B19 phase transformation after dissolution treatment. Added Cu content effects not only transformation temperature but also hysteresis interval [35]. Moreover, the effect increased hardness value with high corrosion resistance, narrow transformation intervals and increasing of the resistance provide with protection of the precipitates such as $TiNi_2$ after addition of copper [36,37].

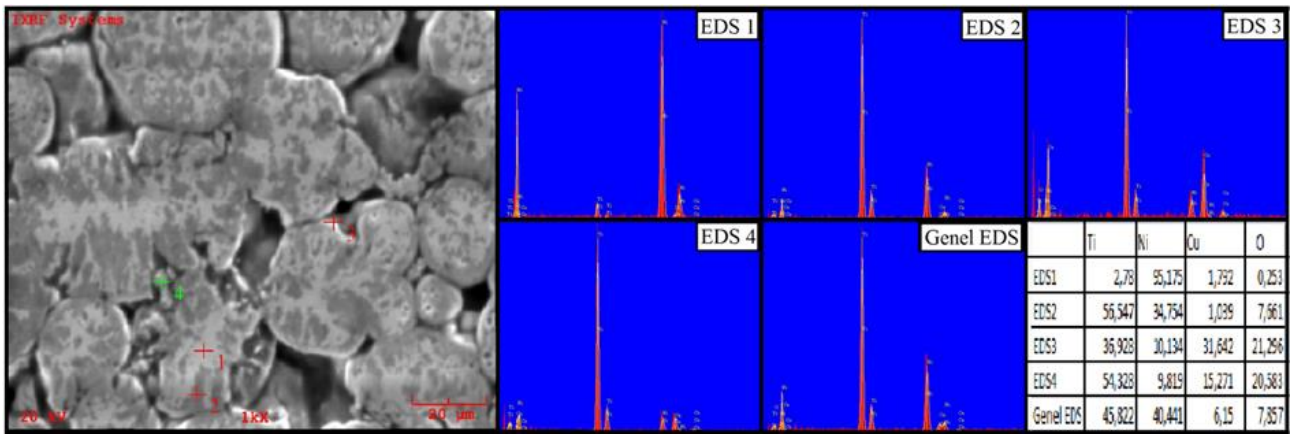

	Ti	Ni	Cu	O
EDS1	2,78	55,175	1,792	0,253
EDS2	56,547	34,754	1,039	7,661
EDS3	36,928	10,134	31,642	21,296
EDS4	54,328	9,819	15,271	20,583
Genel EDS	45,822	40,441	6,15	7,857

Figure 12. EDSanalyses of TiNi+Cu samples after sintering at 850ºC for 60 min.

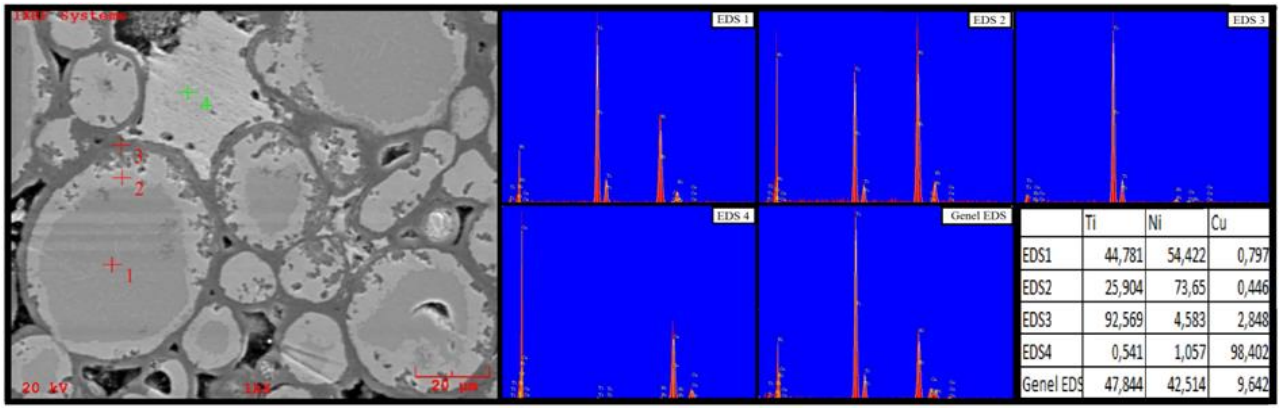

	Ti	Ni	Cu
EDS1	44,781	54,422	0,797
EDS2	25,904	73,65	0,446
EDS3	92,569	4,583	2,848
EDS4	0,541	1,057	98,402
Genel EDS	47,844	42,514	9,642

Figure 13. EDSanalyses of TiNi+Cu samples after sintering at 1000ºC for 60 min

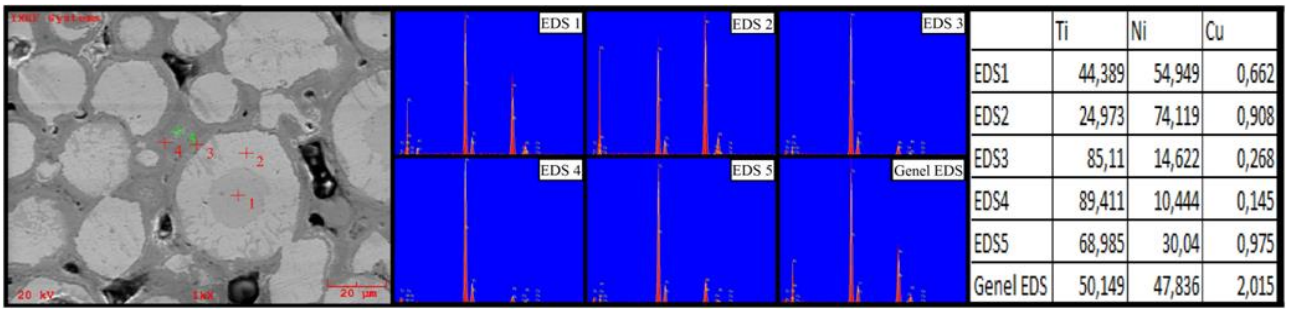

	Ti	Ni	Cu
EDS1	44,389	54,949	0,662
EDS2	24,973	74,119	0,908
EDS3	85,11	14,622	0,268
EDS4	89,411	10,444	0,145
EDS5	68,985	30,04	0,975
Genel EDS	50,149	47,836	2,015

Figure 14. EDS analyses of TiNi+Cu samples after sintering at 1000ºC for 300 min.

3. Conclusions

In this research paper, a homogeneous microstructure in the green powder metals (NiTi alloy) was confirmed with liquid phase sintering occurred with increasing temperature. Optimize sintering temperature and time of NiTi alloy + 4%Cu samples were obtained at 1000°C for 300 minute (5.235 g / cm^3). Hardness value was measured as 730 HV and an important significant increase in the hardness value was determined with multiphase structures ($TiNi_3$, NiTi, Ti_2Ni, Ni_4Ti_3 and NiTiCu) formed depending on the sintering temperature and time. It was determined that could be achieved of low porosity and good corrosion resistance, a homogeneous microstructure and martensitic transformation structures by the addition of wt.4%Cu content.

Acknowledgment

Due to the valuable contributions has shown to this study, We would like to thank Dr. Sinan Aksöz.

References

1. Jani J.M., Leary M., Subic A., Gibson M.A., A review of shape memory alloy research, applications and opportunities. Materials and Design, 2014. 56: p. 1078–1113.
2. Capek J., Vojtech D., Novak P., Preparation Of The NiTi Alloy By A Powder Metallurgy Technique. Metal 2012. Brno, Czech Republic.
3. Petrini L., MigliavaccaF., Biomedical applications of shape memory alloys. J. Metall, 2011.
4. Song C., History and current situation of shape memory alloys devices for minimally invasive surgery. Open Med Dev J., 2010. 2: p.24–31.
5. Morgan N.B., Medical shape memory alloy applications – the market and its products. Mater Sci Eng., A., 2004. 378: p.16–23.
6. Machado L.G., Savi M.A., Medical applications of shape memory alloys. Braz J Med Biol Res., 2003. 36: p. 683–91.
7. Duerig T, Pelton A, Stöckel D., An overview of nitinol medical applications. Mater SciEng, A., 1999. 273–275: p. 149–60.
8. Bram M., Ahmad-KhanlouA.,Heckmann A., Fuchs B., Buchkremer H.P., Stöver D., Powder Metallurgical Fabrication Processes For NiTi Shape Memory Alloy Parts. Material Science and Engineering: A, 2002. Volume 337, Issues 1-2, p. 254-263.
9. B. Thierry, M. Tabrizian, C. Trepanier, O. Savadogo, L.H. Yahia, Effect of surface treatment and sterilization processes on the corrosion behavior NiTi shape memory alloy. Journal of biomedical materials research, 2000. 51: p. 685-693.

10. Mentz J., Frenzel J., Martin F.- Wagner X., Neuking K., Eggeler G., Buchkremer H.P., Stöver D., Powder Metallurgical Processing of NiTi Shape Memory Alloys With Elevated Transformation Temperatures, Material Science and Engineering: A, 2008. Volume 491, Issues 1-2, p. 270-278.

11. Krone L., Shuller E., Bram E., Hamed O., Buchkremer H.P., Stöver D., Mechanical Behaviour Of NiTi Parts Prepared By Powder Metallurgical Methods. Material Science and Engineering: A, 2004. Volume 378, Issues1-2, p. 185-190.

12. Gökmeşe, H., Bostan, B., Microstructural characterization and synthesis by mechanochemical method of nanoparticle Al2O3/B4C ceramic phase, Journal of the Faculty of Engineering and Architecture of Gazi University, 2014. 29:2, p. 289-297.

13. Xu J.L., Jin X.F., Luo J.M., Zhong Z.C., Fabrication and properties of porous NiTi alloys by microwave sintering for biomedical applications. Materials Letters, 2014. 124: p.110–112.

14. Gökmeşe, H., Bostan, B., AA 2014 Alaşımında Presleme ve Sinterlemenin Gözenek Morfolojisi ve Mikroyapısal Özelliklere Etkileri, Gazi Üniversitesi Fen Bilimleri Dergisi Part C: TasarımveTeknoloji. 2013. 1(1): p. 1-8.

15. Yıldız, S., Köroğlu, M., Gökmeşe, H., Bostan, B., Al-%4.5Cu ve AA 2014 Toz Metal Parçalarının Sinterleme Tavrı ve Mekanik Özelliklerinin İncelenmesi. 7. Uluslararası Toz Metalurjisi Konferansı ve Sergisi, 2014. p. 225-226.

16. Nishida M., Hara T., Ohba T., Yamaguchi K., Tanaka K., and Yamauchi K., Experimental Consideration of Multistage Martensitic Transformation and Precipitation Behavior in Aged Ni-Rich Ti-Ni Shape Memory Alloys. Materials Transactions, 2003. 44: 12 p. 2631-2636.

17. Aydoğmuş T., Bor A.Ş., Production and characterization of porous TiNi shape memory alloys. Turkish J. Eng. Env. Sci. 2011. 35: p. 69 – 82.

18. Lagoudas D.C., Shape Memory Alloys-Modelling and Engineering Applicatio. Springer Science + Business Media LLC, Department of Aerospace Engineering, Texas A&M University, College Station, USA, 2008. p. 2-6, 23-41, 281.

19. German R.M., Editörler; Sarıtaş S., Türker M., Durlu N., "Toz metalurjisi ve parçacikli malzeme işlemleri. Bölüm 8, Sinterleme Kavramları, 2007. p.258, Uyum Ajans, Ankara.

20. Whitney M., Corbin S.F., Gorbet R.B., Investigation of the mechanisms of reactive sintering and combustion synthesis of NiTi using differential scanning calorimetry and microstructural analysis. Acta Materialia, 2008. 56: p. 559–570.

21. Chen G., Liss K.-D., Cao P., In situ observation and neutron diffraction of NiTi powder sintering. Acta Materialia, 2014. 67: p. 32–44.

22. Metals Handbook, Alloy Phase Diagrams. 1994. 9th ed., vol. 3. ASM.

23. Li Bing-yun, Li-Jian, Yi-Yi, Porous NiTi Alloy prepared from Elemental Powder Sintering. Chinese Academy of Science, 1998. Vol.13, No.10, p. 2847-2851..

24. Al-SaffarS.M., Al-Hassani E.S., Hussein R.A., "Characterization of Niti Super Elasticity ShapeMemory Alloys", Eng. &Tech. Journal, Vol. 31, Part (A), No.16, (2013).

25. Bram M., Ahmad-Khanlou A., Heckmann A. , Fuchs a B., Buchkremer H.P., Stöver D., Powder metallurgical fabrication processes for NiTi shape memory alloy parts. Materials Science and Engineering A, 2002. 337 : p. 254 – 263.

26. Corbin S.F., Cluff D., Journal of Alloys and Compounds. 2009. 487: p.179-86.

27. Cluff D., Corbin S.F., The influence of Ni powder size, compact composition and sintering profile on the shape memory transformation and tensile behaviour of NiTi. Intermetallics, 2010. 18: p. 1480-1490.

28. Zhang N., Khosrovabadi P.B., Lindenhovius J.H., Kolster B.H., Mater. Sci. Eng: A, 1992. p. 150:263.

29. Bertheville B, Neudenberger M., Bidaux J.E., Mater. Sci. Eng. A, 2004. p. 384:143.

30. Bertheville B., Bidaux J.E., J. Alloys Compd., 2005. 387: p. 211–216.

31. Corbin S.F., Cluff D., Determining the rate of (-Ti) decay and its influence on the sintering behavior of NiTi. Journal of Alloys and Compounds, 2009. 487: p. 179–186.

32. Ismail M.H., Goodall R., Davies H.A., Todd I., Porous NiTi alloy by metal injection moulding/sintering of elemental powders: Effect of sintering temperature. Materials Letters, 2012. 70: p:142–145.

33. Verdian M.M., Raeissi K., Salehi M., Sabooni S., Characterization and corrosion behavior of NiTi-Ti_2Ni-Ni_3Ti multiphase intermetallics produced by vacuum sintering. Vacuum, 2011. 86 : p. 91-95.

34. Goryczka T., Van Humbeeck J., Characterization of a NiTiCu shape memory alloy produced by powder technology. 2006. Volume: 17, issue: 1-2,

35. Rani S., Awan M.S., Qureshi I.N., Yasmin F. and Farooque M., Effect of Cu on Structural and FF-Behavior of NiTi Shape Memory Alloy. Key Engineering Materials, 2010. Vol. 442: p. 301-308.

36. Nam T.H., Saburi T., Nakata Y. and ShimizuK., Shape memory characteristic and lattice deformation In Ti-Ni-Cu alloys. Materials Transactions JIM, 1990. 31: p.1050-1056.

37. Fukuda F., Kakeshita T., Kitayama M. and Saburi K., Effect of ageing on martensitic transformation in a shape memory Ti40.5Ni10Cu alloy. Journal de Physique IV5, 1995. p. C8-717.

Available online at www.dergipark.gov.tr

INTERNATIONAL ADVANCED RESEARCHES
and
ENGINEERING JOURNAL

Journal homepage: www.dergipark.gov.tr/iarej

International
Open Access

Volume 02
Issue 01

April, 2018

e-ISSN: 2618-575X

Research Article

Feedback-based IKP solution with SMC for robotic manipulators: the SCARA example

Tolgay Kara[a]*, Ali Hussien Mary[b]

[a]*Department of Electrical and Electronics Engineering, University of Gaziantep, Gaziantep, Turkey*
[b]*Mechatronics Engineering Department, Al-Khwarizmi College of Engineering, University of Baghdad, Baghdad, Iraq*

ARTICLE INFO

Article history:
Received 26 February 2018
Revised 20 March 2018
Accepted 22 March 2018

Keywords:
Inverse kinematics problem
Multi-link robotic manipulators
SCARA robot

ABSTRACT

This paper presents a novel scheme for solving inverse kinematics problem (IKP) of a multi-link robotic manipulator. Important features of the proposed strategy are generality and simplicity regardless of the number of degrees of freedom (DOF) and geometry of the robot. The proposed method is a feedback strategy where the IKP solution is expressed as a dynamic control system whose goal is to maintain satisfactory trajectory tracking. As a simulation test to reveal the performance of proposed scheme, a four DOF Selective Compliance Assembly Robot Arm (SCARA) system is considered. Feedback law in proposed closed-loop solution method is selected as a combination of Sliding Mode Control (SMC) and Proportional-Derivative (PD) control for providing simplicity and robustness. Simulation results are used to show the efficacy of proposed IKP solution approach in comparison with commonly used neural networks (NN) based IKP solution method. Results reveal that proposed method yields the solution of IKP with satisfactory performance.

1. Introduction

Although different methods have been introduced to solve the IKP, still there are some weak points in these methods [1-3]. In recent years, many computational intelligence methods including NN based methods have been proposed and applied successfully for solving IKP faster than numerical methods [4-6]. Especially NN methods have been extensively preferred by researchers to solve the IKP [6-10]. Ability of fuzzy logic in modeling complex systems by generating rules based on human experiences motivated many researchers to use fuzzy logic with NN to reduce computation time required in training stage [11]. The methods mentioned above suffer from long computational time, complex computations and sensitivity to initial values.

A novel approach for the solution of the IKP is proposed in this study with a feedback structure in nature. In this approach, a feedback control system is considered where the set point is designated as the desired end-effector trajectory and the controlled variables are the joint trajectories. The solution of the IKP is achieved using a robust strategy based on PD and SMC.

2. Proposed Inverse Kinematics Solution

In this section, a novel method for solving IKP of the multi-link robotic arm based on SMC is presented. Drawbacks and disadvantages of important schemes such as NN and Jacobian based methods have been eliminated. Huge training dataset, and singularity are main drawbacks of NN and Jacobian based methods, respectively. The proposed method is a feedback strategy and for a known end effector position and orientation, a hybrid controller combining SMC with PD is proposed to minimize the error between desired and actual trajectories.

Important advantages of proposed method are:

- It is an on-line algorithm, which means it can be applied in real time.
- The solution is given in position level while most other methods are based on velocity and acceleration

* Corresponding author. Tel.: +90-342-317-2135; Fax: +90-342-360-1103.
E-mail address: kara@gantep.edu.tr
Note: This study was presented at International Advanced Researches and Engineering Congress 2017 (IAREC'17)

trajectories, which may be not be accurate due to measurement noise.

- Singularity problem is solved because proposed solution avoids determining inverse of Jacobian matrix.

SCARA robotic manipulator is used in simulations to demonstrate the effectiveness and generality of the proposed method.

2.1 Kinematic Analysis of SCARA Robot

The SCARA robotic manipulator is one of the most important and well-known robotic manipulators used successfully in many industrial applications such as packaging, cell manufacturing lines assembly, pick-and-place and so on. Figures 1 and 2 show the diagram of a 4-DOF SCARA robot in three dimensional (3D) and two dimensional (2D) views, respectively. In forward kinematics the end effector of robot arm motion with respect to the global coordinate system is studied. The origin of the global frame is located at the base of the robot arm as shown in Figure 3. Homogeneous transformation known as Denavit–Hartenberg (DH) notation is used to describe the forward kinematics of robot arm based on four parameters of each link as follows:

$$A_i = Rot(z,\theta_i)Trans(0,0,d_i)Trans(a_i,0,0)Rot(x,\alpha_i) = \begin{bmatrix} \cos\theta_i & -\sin\theta_i\cos\alpha_i & \sin\theta_i\sin\alpha_i & a_i\cos\theta_i \\ \sin\theta_i & -\cos\theta_i\cos\alpha_i & -\cos\theta_i\sin\alpha_i & a_i\sin\theta_i \\ 0 & \sin\alpha_i & \cos\alpha_i & d_i \\ 0 & 0 & 0 & 1 \end{bmatrix} \quad (1)$$

where θ_i represent joint angles from the X_{i-1} axis to the X_i about the Z_{i-1}, d_i refer to the distance between origin of the i[th] coordinate frame to the intersection of the Z_{i-1} axis along the Z_{i-1} axis, a_i represent the distance form intersection of the Z_{i-1} axis with the X_i axis to the origin of the i[th] frame along the X_i axis, and α_i are the angles from the Z_{i-1} axis to the Z_i axis about the X_i [12]. DH parameters of the SCARA robot are shown in Table 1.

Table 1. DH parameters of SCARA robot

i	q_i	d_i	a_i	α_i
1	q_1	L_{12}	L_{11}	0
2	q_2	0	L_2	0
3	0	d_3	0	π
4	q_4	L_4	0	0

$$A_{end-effector} = A_1.A_2.A_3.A_4 = \begin{bmatrix} n_x & s_x & a_x & p_x \\ n_y & s_y & a_y & p_y \\ n_z & s_z & a_z & p_z \\ 0 & 0 & 0 & 1 \end{bmatrix} \quad (2)$$

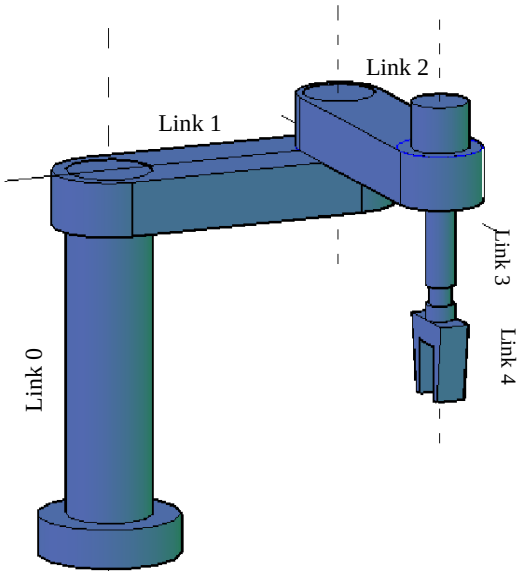

Figure 1. 3D view of the SCARA system

$$A_1 = \begin{bmatrix} \cos\theta_1 & -\sin\theta_1 & 0 & L_{11}\cos\theta_1 \\ \sin\theta_1 & -\cos\theta_1 & 0 & L_{11}\sin\theta_1 \\ 0 & 0 & 1 & L_{12} \\ 0 & 0 & 0 & 1 \end{bmatrix} \quad (3)$$

$$A_2 = \begin{bmatrix} \cos\theta_2 & -\sin\theta_2 & 0 & L_2\cos\theta_2 \\ \sin\theta_2 & \cos\theta_2 & 0 & L_2\sin\theta_2 \\ 0 & 0 & 1 & 0 \\ 0 & 0 & 0 & 1 \end{bmatrix} \quad (4)$$

$$A_3 = \begin{bmatrix} 1 & 0 & 0 & 0 \\ 0 & -1 & 0 & 0 \\ 0 & 0 & -1 & d_3 \\ 0 & 0 & 0 & 1 \end{bmatrix}, \quad (5)$$

$$A_4 = \begin{bmatrix} \cos\theta_4 & -\sin\theta_4 & 0 & 0 \\ \sin\theta_2 & \cos\theta_2 & 0 & 0 \\ 0 & 0 & 1 & L_2 \\ 0 & 0 & 0 & 1 \end{bmatrix}, \quad (6)$$

$$A_{end-effector=} \begin{bmatrix} \cos\theta_{124} & \sin\theta_{124} & 0 & L_2\cos\theta_{12} + L_{11}\cos\theta_1 \\ \sin\theta_{124} & -\cos\theta_{124} & 0 & L_2\sin\theta_{12} + L_{11}\sin\theta_1 \\ 0 & 0 & -1 & L_{12} + d_3 - L_4 \\ 0 & 0 & 0 & 1 \end{bmatrix} \quad (7)$$

where a short notation for trigonometric functions is used in (7) such as: $\cos\theta_{ijk}$ stands for $\cos(\theta_i + \theta_j - \theta_k)$, and $\cos\theta_{ij}$ stands for $\cos(\theta_i + \theta_j)$, etc. The end effector orientation can be described based on of the roll-pitch-yaw (RPY) rotations [12, 13]. The rotational angles around the X, Y, and Z axes are:

$$RPY(\varphi_x,\varphi_y,\varphi_z) = Rot(Z_0,\varphi_z)Rot(Y_0,\varphi_y)Rot(X_0,\varphi_x) = \begin{bmatrix} C_{\varphi_y}C_{\varphi_z} & S_{\varphi_x}S_{\varphi_y}C_{\varphi_z} - C_{\varphi_x}S_{\varphi_z} & C_{\varphi_x}S_{\varphi_y}C_{\varphi_z} - S_{\varphi_x}S_{\varphi_z} \\ C_{\varphi_y}S_{\varphi_z} & S_{\varphi_x}S_{\varphi_y}C_{\varphi_z} - C_{\varphi_x}C_{\varphi_z} & C_{\varphi_x}S_{\varphi_y}S_{\varphi_z} - S_{\varphi_x}C_{\varphi_z} \\ -S_{\varphi_y} & S_{\varphi_x}C_{\varphi_y} & C_{\varphi_x}C_{\varphi_y} \end{bmatrix} \quad (8)$$

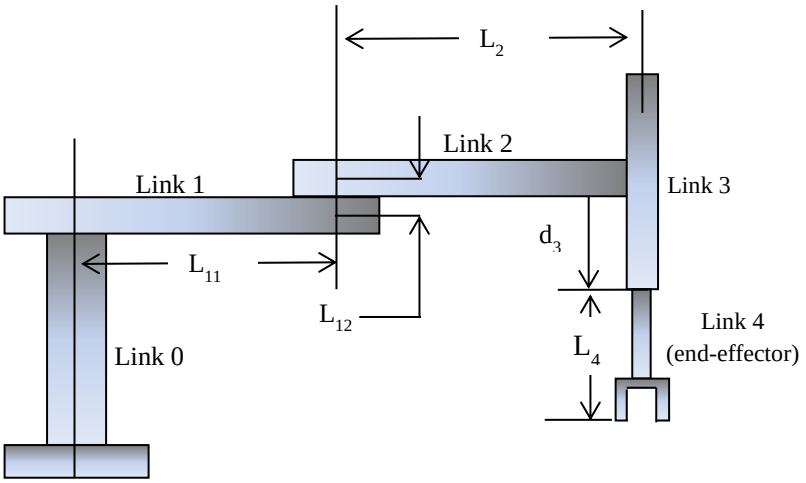

Figure 2. 2D diagram of the SCARA system

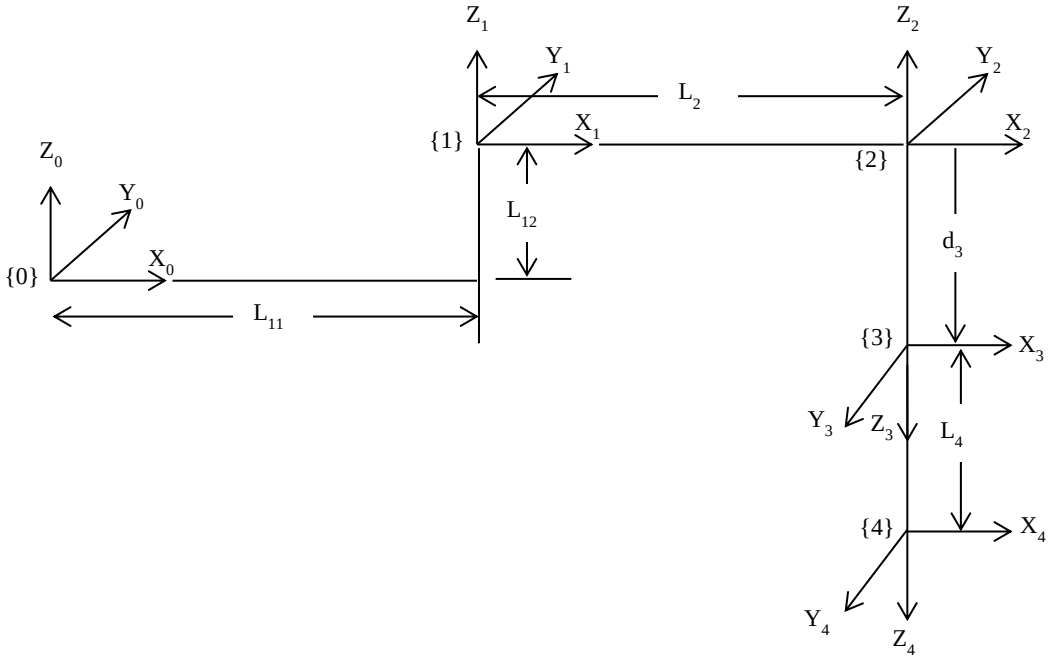

Figure 3. Frame assignment of SCARA system

These angles can be obtained by comparing (7) with the expression in (8).

$$\varphi_x = 0, \quad (9)$$

$$\varphi_y = \pi, \quad (10)$$

$$\varphi_z = \theta_{124}. \quad (11)$$

The forward kinematic of SCARA robot arm can be expressed as:

$$(X, Y, Z, \varphi_z) = F_{Fk}(\theta_1, \theta_2, d_3, \theta_4), \quad (12)$$

and the inverse kinematic for SCARA robot arm is:

$$(\theta_1, \theta_2, d_3, \theta_4) = F_{Ik}\,(X, Y, Z, \varphi_z). \quad (13)$$

2.2 Proposed Robust IKP Solution

The proposed technique for solving the IKP based on feedback theory with SMC by restating the IKP as a dynamic control problem is shown in Figure 4. The proposed method uses the desired Cartesian space trajectory as reference, and the control goal is to find a joint trajectory that can track the desired one. Desired input is the variables in Cartesian space $x_d = [X\ Y\ Z\ \varphi_z]$ while the output is the variables in joint space $\theta = [\theta_1\ \theta_2\ d_3\ \theta_4]$. The proposed method overcomes the drawbacks of previous methods that have been suggested to solve the IKP like complex computations, singularity problem and long time required in iteration methods as discussed above. The proposed control law for this tracking problem is:

$$u = u^{PD} + u^{smc}, \quad (14)$$
$$u^{PD} = k_p\, e(t) + k_d \dot{e}(t), \quad (15)$$
$$u^{smc} = Hsat(s, \emptyset), \quad (16)$$
$$e(t) = x_d(t) - x(t), \quad (17)$$
$$\dot{e}(t) = \dot{x}_d(t) - \dot{x}(t), \quad (18)$$
$$s(t) = \beta e(t) + \dot{e}(t), \quad (19)$$

where $e(t)$ represents the difference between the current and the desired Cartesian coordinates. Using saturation function for switching as given in (16) is a well-established technique in literature [14-16]. Here we propose combination of this technique with the conventionally used PD type sliding surface given in (15) [17, 18].

Remark: The control law depends only on the error signal, its derivative, and the sliding surface. As a consequence, proposed technique is applicable to all kinds of robotic manipulators.

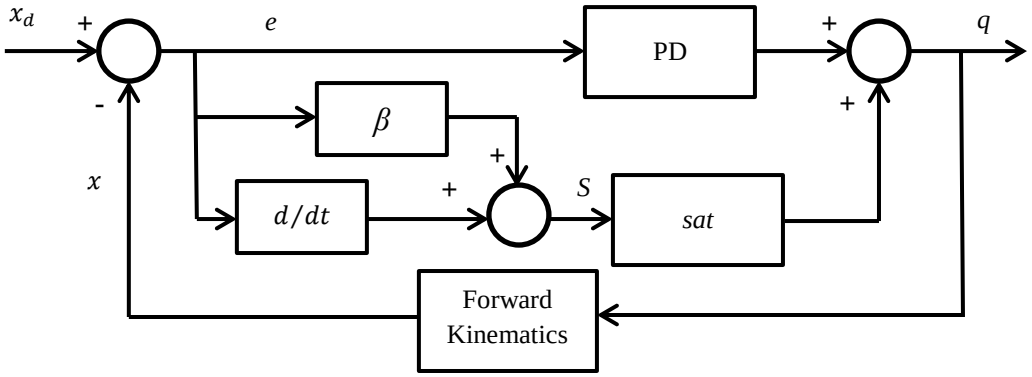

Figure 4. Block diagram of proposed robust IK solution

3. Simulation Tests

The performance of proposed method that is based on PD control with SMC for solving IKP is discussed in this section. In order to demonstrate effectiveness of the proposed IK solution scheme, computer simulation is used for solving IKP of SCARA robot. Performance of proposed method is compared with NN method, which has been used widely in solving IKP in recent years. Since the NN methods are offline, at first they must be trained to learn the map between variables in joint space and variables in Cartesian space. The values of DH parameters used in this simulation are as follows: $L_{11} = 1$, $L_{12} = 0.1$, $L_2 = 1$, and $L_4 = 1$. The gain parameters of proposed controller are $k_p = H = 500I_4$, $k_d = 10I_4$, $\emptyset = 0.01$. The following desired trajectory is used in this simulation:

$$x_d(t) = \cos\left(\frac{\pi}{3} + 0.1\sin(7t)\right) + \cos\left(\frac{\pi}{2} + 0.1\sin(7t) + 0.1\cos(t)\right) \quad (20)$$
$$y_d(t) = \sin\left(\frac{\pi}{3} + 0.1\sin(7t)\right) + \sin\left(\frac{\pi}{2} + 0.1\sin(7t) + 0.1\cos(t)\right) \quad (21)$$
$$z_d(t) = 1 + 0.1t. \quad (22)$$

Note that the tracking control is applied for a maximum simulation time of 10 seconds, which limits the motion along Z direction between 1 and 2. For practical implementation and longer simulation times, the reference trajectory in Z direction should be limited. Figure 5 shows the desired path of end effector in Cartesian space. Integral of the absolute value of the error (IAE) is used for comparison:

$$IAE = \int_0^{tf} |e(t)| dt. \quad (23)$$

Therefore the error along X, Y and Z axes can be determined as follows:

$$Err_x = \int_0^{tf} |e_x(t)| dt = \int_0^{tf} |x(t) - x_d(t)| dt \quad (24)$$
$$Err_y = \int_0^{tf} |e_y(t)| dt = \int_0^{tf} |y(t) - y_d(t)| dt \quad (25)$$
$$Err_z = \int_0^{tf} |e_z(t)| dt = \int_0^{tf} |z(t) - z_d(t)| dt. \quad (26)$$

Roll angle which represents orientation of the end effector is shown in Figure 6 and Cartesian space errors along the X, Y and Z axes are shown in Figure 7. As expected because the trajectory along Z axis is based only on d_3, the NN can easily approximate this relation therefore neural network method and also the proposed control method have very small error value in this axis. These results indicate clearly high accuracy of proposed method. Moreover, proposed method is an on-line method. Performance indices listed in Table 2 indicate superiority of proposed method, where the IAE values are very small for X and Y directions, and almost equal to zero in Z direction. Therefore, the actual Cartesian path is very close to desired Cartesian path with very small cumulative error.

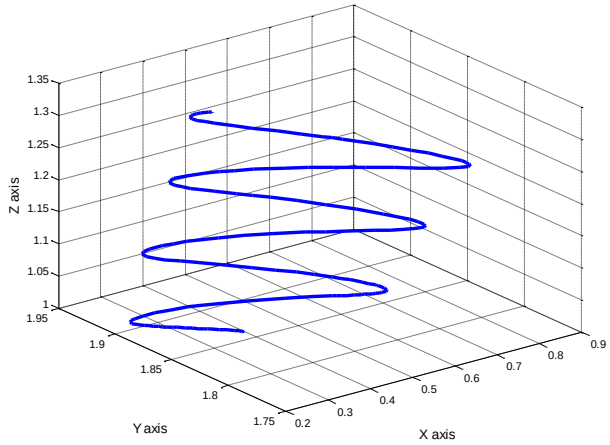

Figure 5. Desired trajectory in Cartesian space

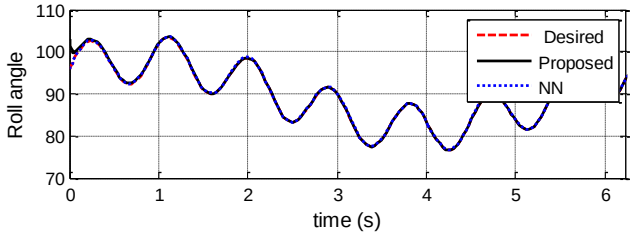

Figure 6. Variation of roll angle versus time

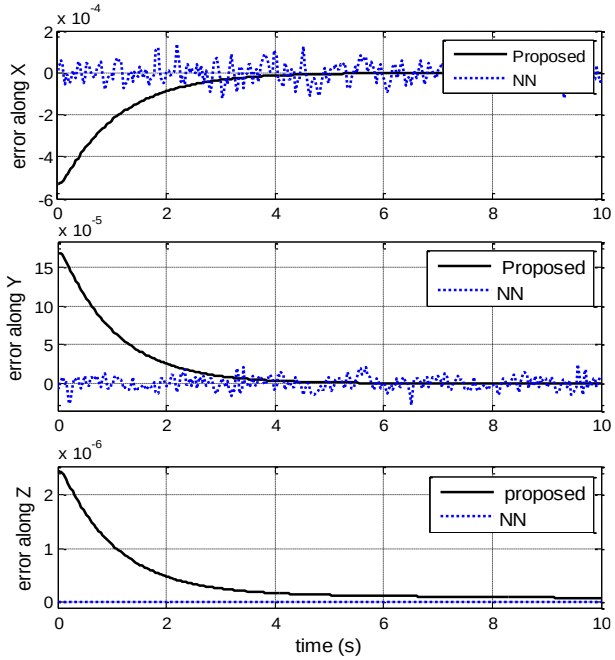

Figure 7. Variation of roll angle along Cartesian axes

Table 2. Performance index *IAE* values for three Cartesian axes

	Proposed	**NN**
Err_x	0.0014	0.0097
Err_y	0.0020	0.0048
Err_z	~0	~0

4. Conclusion

In this paper, a novel IKP solution method for multi-link robotic manipulators based on a feedback control strategy is proposed. The method relies on tracking control with a desired trajectory that represents the desired end-effector angle variation. Proposed method is independent from the degrees of freedom of the manipulator and it is applicable to all kinds of robotic manipulators. A robust scheme that combines PD and SMC is used in the feedback control law. Performance of the method in solving IKP of a SCARA system is illustrated via simulation test results in comparison with the common NN based IKP solution approach. Results prove applicability of proposed method with satisfactory performance.

References

1. Alavandar, S., and M. J. Nigam, *Inverse kinematics solution of 3DOF planar robot using ANFIS.* Int. J. of Computers, Communications & Control, 2008. **3:** p. 150-155.
2. Shen, W, J. Gu, and E. E. Milios, *Self-configuration fuzzy system for inverse kinematics of robot manipulators,* in IEEE Annual meeting of the North American Fuzzy Information Processing Society NAFIPS 2006: p. 41-45.
3. Tarokh, Mahmoud, and M. Kim, *Inverse kinematics of 7-DOF robots and limbs by decomposition and approximation.* IEEE transactions on robotics, 2007. **23**(3): p. 595-600.
4. Duka, A. V., *ANFIS based Solution to the Inverse Kinematics of a 3 DOF planar Manipulator.* Procedia Technology, 2015. **19**: p. 526-533.
5. Duka, A. V., *Neural network based inverse kinematics solution for trajectory tracking of a robotic arm.* Procedia Technology, 2014. **12**: p. 20-27.
6. Ma, C., Z. Yong, C. Jin., W. Bin, and Z. Qinjun, *Inverse kinematics solution for 6R serial manipulator based on RBF neural network.* In International Conference on Advanced Mechatronic Systems ICAMechS 2016: p. 350-355.
7. Mayorga, R. V., and P. Sanongboon, *Inverse kinematics and geometrically bounded singularities prevention of redundant manipulators: An Artificial Neural Network approach.* Robotics and Autonomous Systems, 2005. **53**(3): p. 164-176.
8. Pérez-Rodríguez, R, M-C. Alexis, C. Ursula, S. Javier, C. Cesar, O. Eloy, M. T. Josep, M. Josep, and J. G. Enrique, *Inverse kinematics of a 6 DoF human upper limb using ANFIS and ANN for anticipatory actuation in ADL-based physical Neurorehabilitation.* Expert Systems with Applications, 2012. **39**(10): p. 9612-9622.
9. Zou, X., G. Dawei, W. Liping, and G. Zhenyu, *A novel method to solve inverse variational inequality problems based on neural networks,* Neurocomputing, 2016. **173**(3): p. 1163-1168.

10. Assal, S. F. M, W. Keigo, and I. Kiyotaka, *Neural Network-Based Kinematic Inversion of Industrial Redundant Robots Using Cooperative Fuzzy Hint for the Joint Limits Avoidance.* IEEE/ASME Transactions on mechatronics, 2016. **11**(5): p. 593-603.
11. Lazarevska, E., *A Neuro-Fuzzy Model of the Inverse Kinematics of a 4 DOF Robotic Arm*, in IEEE 14th International Conference on Modelling and Simulation UKSim2012: p. 306-311.
12. Köker, R., *Reliability-based approach to the inverse kinematics solution of robots using Elman's networks.* Engineering applications of artificial intelligence, 2005. **18**(6): p. 685-693.
13. Rolf, M. and J. J. Steil, *Efficient Exploratory Learning of Inverse Kinematics on a Bionic Elephant Trunk.* Neural Networks and Learning Systems, IEEE Transactions on, 2013. **25**(6): p. 1147-1160.
14. Slotine, J-J E., and W. Li, *Applied nonlinear control.* Vol. 199. No. 1. Englewood Cliffs, NJ: Prentice hall, 1991.
15. Fallaha, C. J., M. Saad, H. Y. Kanaan, and K. Al-Haddad, *Sliding-mode robot control with exponential reaching law*. IEEE Transactions on Industrial Electronics, 2001, **58**(2), 600-610.
16. Kachroo, P. and M. Tomizuka, *Chattering reduction and error convergence in the sliding-mode control of a class of nonlinear systems.* IEEE Transactions on Automatic Control , 1996, **41**(7): p.1063-1068.
17. Eker, I., *Sliding mode control with PID sliding surface and experimental application to an electromechanical plant.* ISA transactions, 2006, **45**(1): p.109-118.
18. Parra-Vega, V., S. Arimoto, Y. H. Liu, G. Hirzinger, and P. Akella,(2003). *Dynamic sliding PID control for tracking of robot manipulators: Theory and experiments.* IEEE Transactions on Robotics and Automation, 2003, **19**(6): p. 967-976.

Available online at www.dergipark.gov.tr

INTERNATIONAL ADVANCED RESEARCHES
and
ENGINEERING JOURNAL

Journal homepage: www.dergipark.gov.tr/iarej

e-ISSN: 2618-575X

International Open Access

Volume 02
Issue 01

April, 2018

Research Article

Designing autopilot system for fixed-wing flight mode of a tilt-rotor UAV in a virtual environment: X-Plane

Mehmet Kürşat YALÇIN[a] and Erhan ERSOY[b,*]

[a]Niğde Ömer Halisdemir University, Department of Mechatronics Engineering, Niğde, 51240, Turkey
[b]Niğde Ömer Halisdemir University, Bor Vocational School of Higher Education, Niğde, 51700, Turkey

ARTICLE INFO

Article history:
Received 28 February 2018
Revised 25 March 2018
Accepted 30 March 2018

Keywords:
Autopilot controller
Raspberry Pi
Tilt-rotor
X-Plane flight simulator

ABSTRACT

This paper describes an autopilot system design to regulate the altitude, heading and forward speed in the fixed-wing flight mode of the Osprey V22 VTOL (vertical takeoff and land) tilt rotor UAV accordingly to a reference, which is generated the trajectory sub-block. X- Plane flight simulator developed by Laminar Research, is used to test and optimize the parameter values of the autopilot system, which is designed using feedback, feedforward and PID controllers in MATLAB / Simulink environment (Software in the Loop- SIL). The receiver and sender blocks to perform the data interactions between MATLAB / Simulink and X-Plane flight simulator are created in MATLAB / Simulink environment. The receiver block is used to transfer data from the X-Plane flight simulator to the controller, while the sender block is used to transfer control signals from the controller to the X-Plane flight simulator program. The data communication between the two is UDP. The autopilot system under test is embedded in the Raspberry-Pi minicomputer and a hardware-in loop (HIL) test system created. The reaction of the control algorithm running on the Raspberry-Pi minicomputer to the virtual sensor data generated by the X-Plane flight simulator investigated. It is observed that, the Osprey-V22 aircraft can perform tasks autonomously in the horizontal flight mode, from the experiments and the results obtained. This study also describes the first stage of an undergoing project which aims to develop a robust autopilot for Osprey V22 VTOL UAV.

1. Introduction

In the last few years, researchers have shown great interest in the field of VTOL (Vertical Take-Off and Landing) aerial vehicles [1]. However, most of them are related with quadrotors. Besides these well-known platforms, many researchers recently concentrate on the tilt rotor aerial vehicles combining the advantages of horizontal and vertical flights. Because these new vehicles have no conventional design basis, many research groups build their own tilt-rotor vehicles according to the desired technical specifications and objectives [9]. One of them is fixed-wing VTOL UAV.

The fixed-wing VTOL UAV has a large flight envelope than traditional VTOL UAV since it can hover, and maneuver in 3D space like a multi-rotor as well as fly level forward flight efficiently at high cruise speed [3]. Notable VTOL aircrafts include the Bell XV-15, Bell-Boeing V22 and so on [4]. The development of V-22 aircraft spurred a great research and development effort in tilt rotor aerodynamics, flight control etc [2, 11]. Conventional tiltrotor vehicles are mechanically complex systems since it employs a swashplate and differential rotor tilting to control pitch and yaw, respectively [5].

The model of tilt rotor UAV that is called Osprey V22, is given in Figure 1. Osprey V22 is composed of fuselage, two wings with two trailing edge flaps at each of the wing, nacelles mounted at the wings tips, rotors mounted in front of nacelles and horizontal stabilizer with three flaps and two vertical fins with one rudder mounted on each fin. All components of the aircraft are rigid. The rotors have three blades fixed to the shaft by pitch bearing. The pitch angles of rotor blades are controlled by swash-plates for constant

* Corresponding author. Tel.: *+90 537 218 1868*; Fax: *+90 388 311 8437*.
E-mail address: *erhan.ersoy@ohu.edu.tr*
Note: This study was presented at International Advanced Researches and Engineering Congress 2017 (IAREC'17)

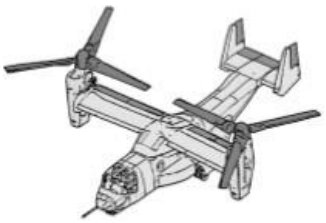

Figure 1. Osprey V22 tilt rotor UAV [23]

(collective) and harmonic (cyclic) components. The engine nacelles are placed at the tip of each wing. They may rotate about axis perpendicular to the fuselage plane of symmetry. [2]. The angle of nacelle rotation is between 0° and 97,5°.

The process of rotating the nacelles to transition between helicopter (vertical flight mode) and airplane (fixed-wing flight mode) modes is called conversion. Many scholars study on how to design the flight control system [12] for helicopter, airplane and conversion flight modes. The vertical and fixed-wing control mode of tiltrotor can be seen in Figure 2. There are some publications describing the mathematical modelling, simulation and control of the tilt wing and tilt rotor UAV [2,4,5,7,14-18]. For this reason, mathematical modeling will not be included in this study. Also, some researches are related with autonomous system performance maximization and minimum energy controller on tilt rotor UAV [25-26].

This paper describes an autopilot control design to change or maintain the altitude, heading and forward speed [20] in the fixed-wing flight mode of the Osprey V22 VTOL tilt rotor UAV accordingly to a reference, which comes from the trajectory generator block. Software-In-the-Loop (SIL) simulation is used to measure the performance of control algorithms. Thus, the controller parameters are set in a short time and with minimum cost. Raspberry Pi minicomputer, which is the hardware to be used in the system, was selected as the first step of creating the system necessary for Hardware-In-the-Loop (HIL) simulation and the necessary infrastructure for communication was established.

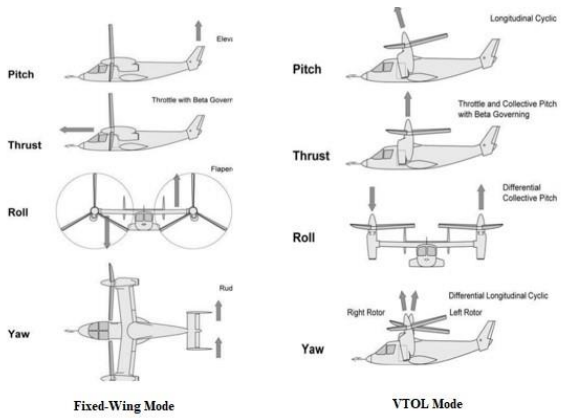

Figure 2. Fixed-wing and VTOL control modes [23]

2. X-Plane Flight Simulator and its Settings

X-Plane is the flight simulator with the world's most realistic flight model. X-Plane is used by industry-leading stakeholders such as air force, aircraft manufacturers to predict flight characteristics of fixed and rotary wing aircraft with high accuracy. The existing aircraft models can be changed by the user, but the user can create custom plane or helicopter designs with Plane Maker software. In addition, the X-Plane simulation environment supports programming languages such as C / C++, MATLAB / Simulink, and Python [6]. There are settings on the X-Plane that need to be set for proper operation of the aircraft, and the configuration of the flight-model per frame is one of these settings. This can be done with the Operations & Warnings tab under the Settings menu in the X-Plane flight simulator program.

Value of this parameter is taken as 10 which is indicated in Figure 3 to guarantee that the model performs better during simulations.

Another excellent property of the X-Plane is its skill to transmit and receive information with the outside world via UDP (User Datagram Protocol) [7]. MATLAB / Simulink provides blocks ready for UDP communication. Communication between X-Plane and MATLAB / Simulink can be achieved on the same computer using the internal address "127.0.0.1" of the network card, and two different computers can be used in case of setting the IP addresses of the sender and receiver blocks. Due to the fact that the communication will be done with UDP, MATLAB / Simulink and X-Plane flight simulator program can run on different computers.

In the “VTOL_Control_Example” model created in MATLAB / Simulink, the IP addresses of the sender and receiver blocks are "192.168.0.100" which is the IP address of the computer running the X-Plane flight simulator program. The network configuration on the X-Plane is shown in Figure 4 and Figure 5.

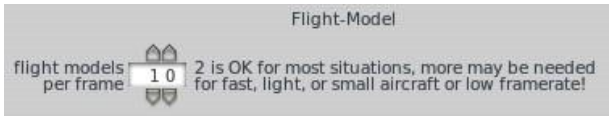

Figure 3. Flight model per frame

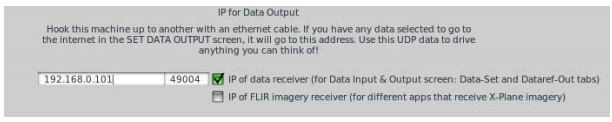

Figure 4. IP configuration

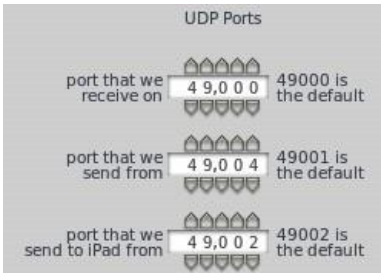

Figure 5. Port configuration

The data package of the X-Plane follows a standard format, which requires a header and a data set sequence. The header shown in Table 1 shows the following bytes [7]:

1. 0-3 bytes contain "DATA" characters indicating that it is a data packet [7].

2. The 4th byte is a internal (I) code and is not used for data transmission. It is normally defined as zero [7].

3. The bytes after the 4th byte in Table-1 are of interest to the state of the aircraft and the input and output data to be intervened can be defined by selecting appropriate places on the table in Figure 6.

The parameter selection in Figure 6 can also be done with automatically. The necessary specifications like IP number, Port number, Waypoint data and Input/Output data, which uses by UDP, can be written in PostLoadFcn under the model properties of Simulink.

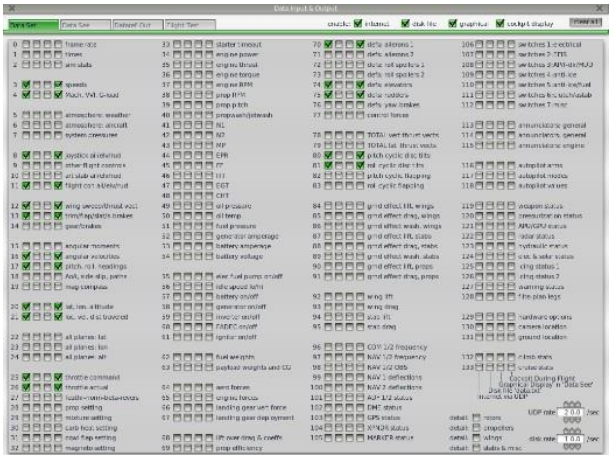

Figure 6. Selected parameters (input and ouput data)

3. MATLAB/Simulink Program and its Settings

Simulink is a block diagram based environment for model-based design that simulates multi-disciplinary systems. In Simulink environment; system level design, simulation, automatic code generation, continuous testing, and verification of embedded systems can be done. Simulink offers a graphical editor, customizable block library and solvers for modeling and simulating dynamic systems. Simulink integrated with MATLAB, you can use MATLAB algorithms in the model and move your simulation results to the MATLAB environment for further analysis [8]. The communication interface blocks are given in Figure 7. These two blocks consist of three sub-block. These are respectively UDP send/receive block, byte pack/unpack block and last one is embedded MATLAB functions. There are some settings on the Simulink that need to be set for proper communication with X-Plane flight simulator. One of them is IP and port configuration of UDP receive-send blocks. The communication block configurations of Simulink are given in Figure 8.

Figure 7. The communication blocks of sender and receiver

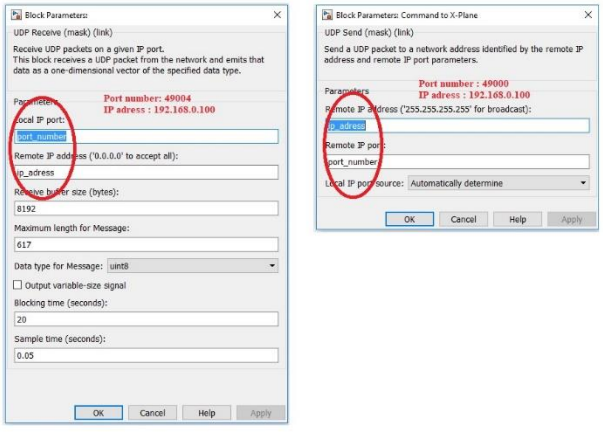

Figure 8. UDP communication blocks (receive and send) ports configuration

Table 1 X-Plane data package pattern

Bytes	0	1	2	3	4	5	6	7	8	9	10	11	12	13	14	15	16	.	.	.	.	.	.	.	.	.	38	39	40	41
Value	D	A	T	A	I	L_1	L_2	L_3	L_4	B_{11}	B_{12}	B_{13}	B_{14}	B_{21}	B_{22}	B_{23}	B_{24}	.	.	.	.	.	.	.	.	.	B_{81}	B_{82}	B_{83}	B_{84}

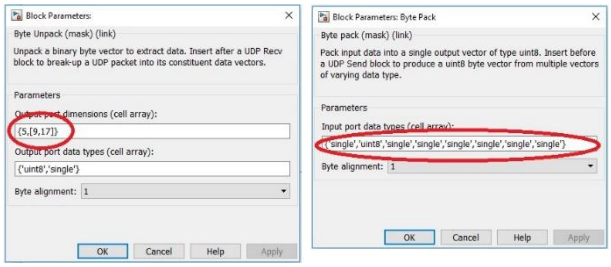

Figure 9. Byte unpack and pack settings

Also some settings are needed for byte pack and unpack blocks. Byte pack block is used just to pack the data in an array of bytes [7]. The configuration of the byte pack block is given right side of the Figure 9. Byte unpack block is used to unpack the data coming from X-Plane flight simulator through the UDP Receive block. Byte unpack block configuration is shown left side of the Figure 9. The unpack block is configured to output 5 bytes (the header), plus a matrix of 17 set of data [7] with 9 fields. With this configuration, the maximum length of the message will be 617 (5 bytes header + 17 set of data * 9 fields * 4 bytes each). This data can be seen left side in Figure 8. The input of the byte pack block is respectively header; internal code (generally zero) and the others are commands, which will be send to X-Plane flight simulator with UDP send block.

The embedded function is responsible to convert quadruple bytes into a single format floating point, which are then converted into double format to be used by the following blocks [7].

4. Design of the Trajectory Generator and Control System

The Simulink model consist of four part, these are trajectory generator block, controller block, communication interface block, and finally visualizer block. This Simulink model can be seen from Figure 10. The trajectory generator block, given in detail at Figure 11, is responsible to generate references for the aircraft in order to perform the desired mission. For this reason, a MATLAB function is written in Simulink. This function consists of two basic algorithms. These are waypoint switching and heading reference generation. The trajectory generator block creates heading reference for the attitude controllers in order to drive the aircraft to the next waypoint.

Waypoints are made up from three parts, i.e., latitude, longitude and altitude. The reference value of altitude directly comes from the waypoint list, but the heading reference angle must be computed. The heading angle can be computed by using line of sight (LoS) formula, given in Equation (1).

$$LoS = atan2\left[\frac{Lon_{wp} - Lon_{vtol}}{Lat_{wp} - Lat_{vtol}}\right] * 180/\pi \quad (1)$$

By using Equation (1), the reference-heading angle is found between -180° and 180°. Bu the actual heading angle of aircraft, which is read from X-Plane via UDP, is between 0° and 360°. So it must be shifted to the interval, -180° and +180°, in order to follow the shortest path. For this reason, a short code is written in MATLAB.

Way point switching scheme is explained as follows. A variable, called as waypoint index, holds the current active target waypoint, and its initial value is one. When the aircraft reach the waypoint, the waypoint index is increased. But how the system decide a waypoint is reached. First of all a distance variable (D) between plane and active target waypoint is defined and computed by using Equation (2), and the unit of D is degree. The distance (D) is then converted from degree to meter by using "Haversine" formula (given Appendix A). When the distance is less than or equal to a threshold R ($D \leq R$ in Figure 12), it is understood that the waypoint is reached. R is computed by Equation (3). Here β is the bank angle and V is the airspeed of the aircraft.

$$D = \sqrt{\left(Lon_{wp} - Lon_{vtol}\right)^2 + \left(Lat_{wp} - Lat_{vtol}\right)^2} \quad (2)$$

$$R = 0.3048 * \left[\frac{V^2}{11.26 * tan\,(\beta)}\right] \quad (3)$$

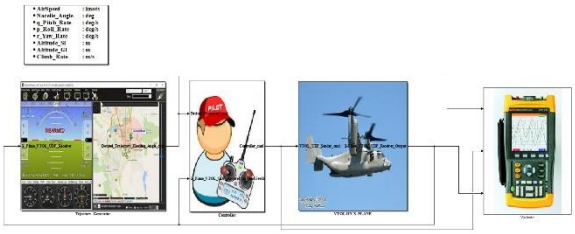

Figure 10. Simulink model of VTOL fixed-wing UAV control system for airplane mode

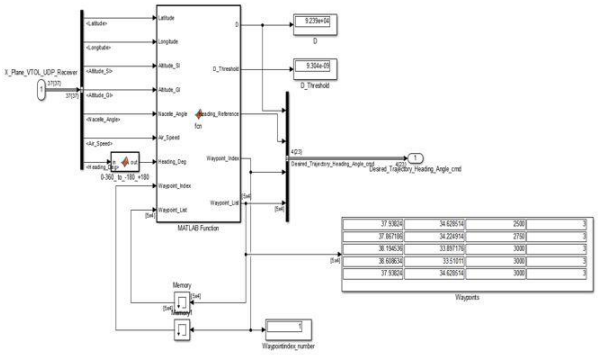

Figure 11. Trajectory generator block

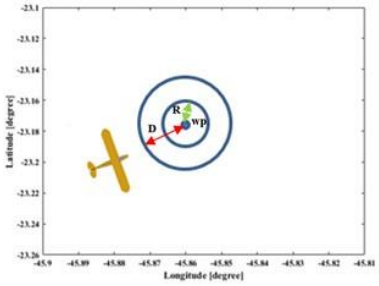

Figure 12. Distance between VTOL and waypoint [7]

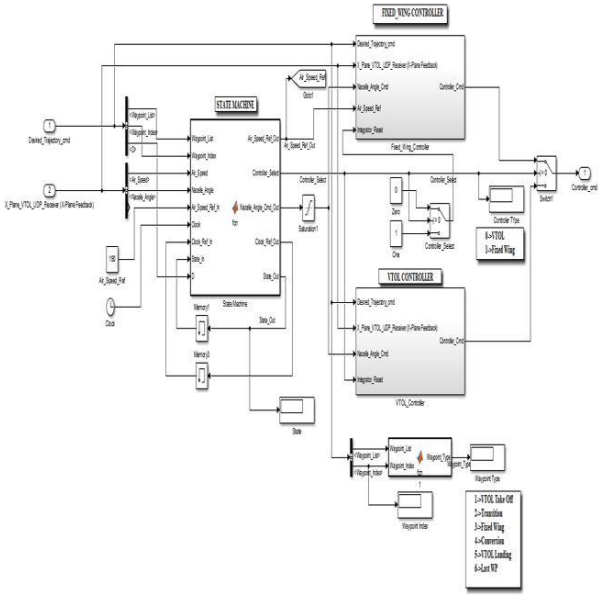

Figure 13. Controller model at MATLAB/Simulink

The control block is designed to alter and stabilize the VTOL aircraft altitude, heading, and forward speed in order to track their references [20], which comes from the waypoint list in trajectory generator block. The controller model at the MATLAB / Simulink is given in Figure 13. The controller block includes both feedback and feedforward control scheme. The feedback control loop is responsible for longitudinal, lateral direction of the aircraft.

The feed-forward terms are used to correct errors caused by coupling movements [20-22]. The control algorithms for the altitude and attitude, i.e., roll, pitch and yaw, of the VTOL tiltrotor aircraft are designed based on PID controller. All controllers contain inner and outer loops. Heading angle is indirectly controlled by aileron through roll angle (Figure 14). The reference roll signal is generated accordingly the error between reference heading angle and current heading angle. The reference-heading angle comes from trajectory generator block. The output of the outer loop is the reference signal for inner roll controller and is saturated in the interval, $[-45^{\circ}, 45^{\circ}]$. The roll controller is responsible for stabilizing the aircraft's roll angle. It utilizes ailerons to alter the roll angle of the aircraft [20]. Aileron commands are sent to X-Plane and are limited to -1 to +1 by software. All parameters of heading controller is given in Table 2.

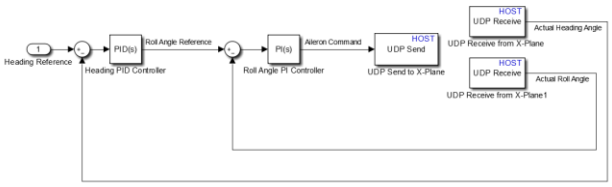

Figure 14. Inner and outer feedback loops for heading controller.

Table 2. Parameters for heading controller.

Heading PID	K_p	3.5
	K_i	1.0
	K_d	0.5
Roll PI	K_p	0.01
	K_i	0.0002

The longitudinal control system emphasizes the altitude and the forward speed. The altitude controller is implemented in a cascade form (Figure 15). The output of this controller is the reference for pitch controller inner loop. Then the output of pitch controller is the angle of the elevator control surface. Thus, both pitch angle and altitude of the aircraft are ensured to be under control [20]. The maximum pitch angle is limited to -10° to +15° by software. These values should be transformed to X-Plane elevator control surface commands in some limits that is -1 and +1. All parameters for altitude controller is given in Table 3. For forward speed control PI control is implemented and the parameter values of the controller are Kp=0.02 and Ki=0.1, respectively. In addition, a feed forward control gain (Kpff=0.015) is multiplied by altitude error and then added to the output of the forward speed controller to compensate the loss of the altitude.

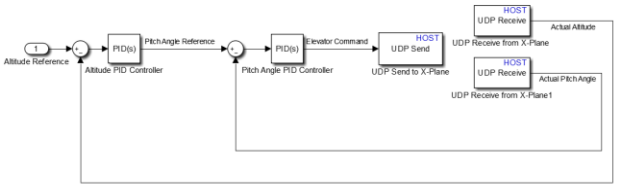

Figure 15. Inner and outer feedback loops for altitude controller.

Table 3. Parameters for altitude controller.

Altitude PID	K_p	0.2
	K_i	0.02
	K_d	0.01
Pitch PID	K_p	0.1
	K_i	0.1
	K_d	0.01

5. Implementation and Application Results

In this study, a laptop, a PC and Raspberry Pi are used as to develop control architecture, to run flight dynamics and to implement controller respectively, as shown in Figure 16. The Raspberry Pi is a low cost, credit-card sized computer that plugs into a computer monitor or TV, and uses a standard keyboard and mouse. It is a capable little device that enables people of all ages to explore computing, and to learn how to program in languages like C, Scratch and Python [24]. The Raspberry Pi can be seen on Figure 17.

Simulink Support Package for Raspberry Pi Hardware enables to create and run Simulink models on Raspberry Pi hardware. The support package includes a library of Simulink blocks for configuring and accessing I/O peripherals and communication interfaces. After creating Simulink model, it can be simulate, tune algorithm parameters until get it just right, and download the completed algorithm for standalone execution on the device. With the MATLAB Function block, MATLAB code is incorporated into the Simulink model. With Simulink support package for Raspberry Pi, the algorithm developed in Simulink can be deployed to the Raspberry Pi using automatic code generation [19].
At the end of this process, an embedded control system was made and autopilot control system is then run on the Raspberry Pi in a standalone fashion.

Figure 16. Implementation of autopilot test platform

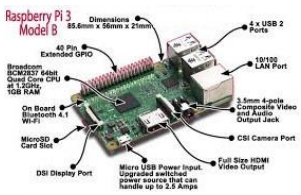

Figure 17. Raspberry Pi 3

Communication between Raspberry Pi and X-Plane occurs through ethernet port using via UDP.

The parameter of the Waypoint List is given in Table 4 for testing the autopilot performance. The list consist of five waypoints. First and last is the same point but the altitude is different each other. We requested to move around the waypoint by coming to the fifth waypoint through the transition points from the autopilot. For this reason, the simulation is started by using "Get Me Lost" function of the X-Plane flight simulator. In Figure 18, the simulated flight path according to the "Waypoint List" data is given on the Google Maps. The straight lines show the references and dashed line shows the real path of the aircraft. In addition, the 3D flight path on X-Plane is also given in Figure 19. The result, which is taken in Figure 18-19, represents one tour on the route. The responses of the controller for the flight path are given in Figure 20-29. In the Figure 20, the altitude behavior of the controller is given.

Table 4. Waypoint List

Waypoints List	Latitude (°)	Longitude (°)	Altitude (m)
Waypoint_1	37.938240	34.628514	2500
Waypoint_2	37.867186	34.224914	2750
Waypoint_3	38.194536	33.897176	3000
Waypoint_4	38.608634	33.510110	3000
Waypoint_5	37.938240	34.628514	3000

The blue line represents the altitude reference and dashed red line is altitude response of the controller with respect to sea level in meters. Some overshoot occurs instant the switching of waypoint, because the lift of the wing is decreasing. For this reason, pitch of the aircraft increases to maintain the altitude and airspeed increases for a short time. Figure 21 shows the airspeed response of the all flight path.

The maximum overshoot of the airspeed is less than 6 percent, and then airspeed is decreased by the controller and tracks the reference value.

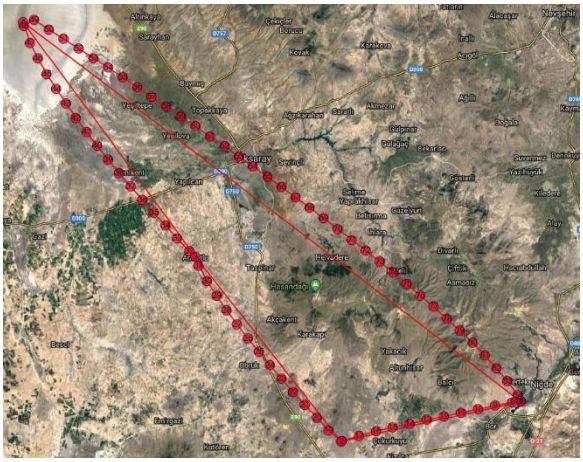

Figure 18. Flight path for waypoint list on X-Plane

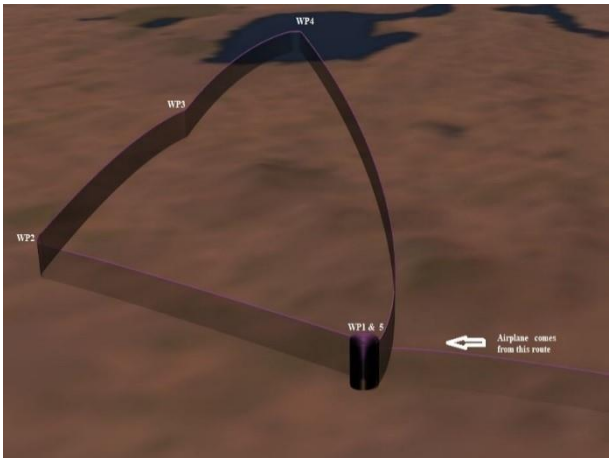

Figure 19. 3D Flight path for waypoint list on X-Plane

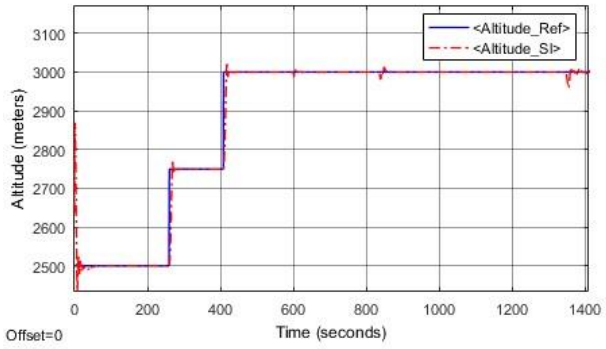

Figure 20. Altitude response

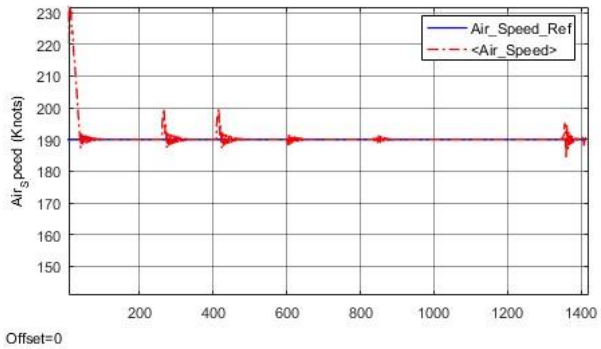

Figure 21. Forward speed response

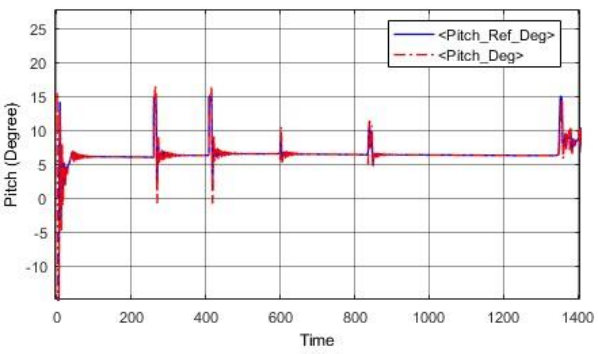

Figure 22. Pitch response

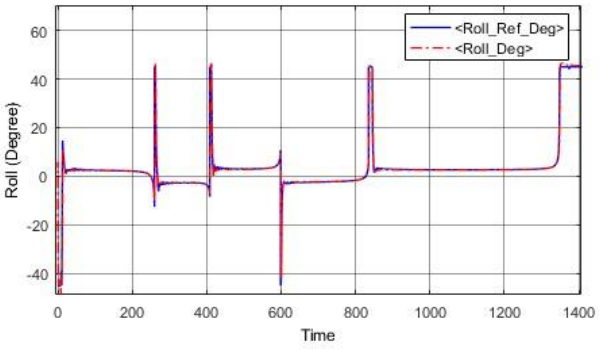

Figure 23. Roll response

The solid blue lines of the Figure 22, 23 and 28 represent the reference values of the pitch, roll and heading, respectively. Dashed red lines are the response of the aircraft. The pitch value is limited between -10° and +15° and the roll value is limited between -45° and +45°. The heading angle is changing between -180° and +180°.

In airplane mode due to a combination of having zero angle of incidence in the wing and the thrust line being above the centerline of the aircraft, the pitch reference of the Osprey V22 about 7 degrees. The aileron and elevator command and surface deflections are given through between 0 and 1400 sec in Figure 24-25. It is clear from the Figure 24, aircraft tracks the aileron reference command, which is generated by the inner loop of the roll controller block.

Elevator command and surface response looks like not tracking each other in Figure 25. The reason is related the elevator trim value, which is produced with altitude error by a cross coupling gain.

Figure 26-28 is related with heading response of the heading controller. The reference latitude and longitude values and the controller response for these values are given in Figure 26 and 27, respectively. In addition, the detailed reference values of latitude and longitude can also be found at Table 4.

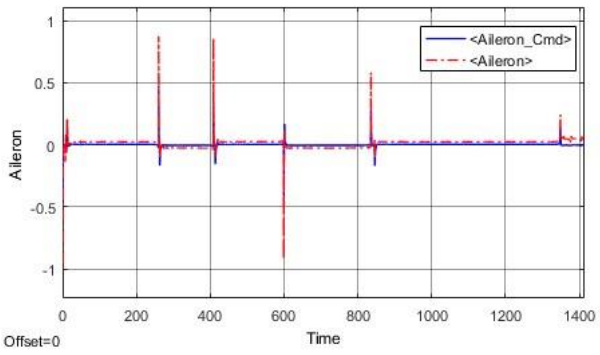

Figure 24. Aileron surface response

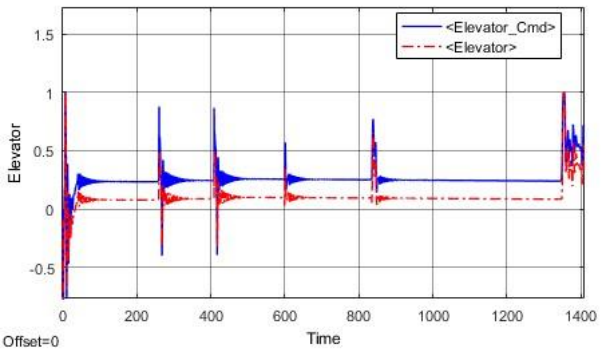

Figure 25. Elevator surface response

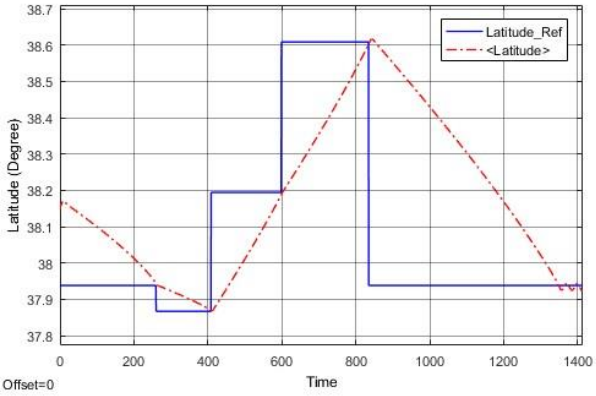

Figure 26. Latitude reference and response of the lateral controller

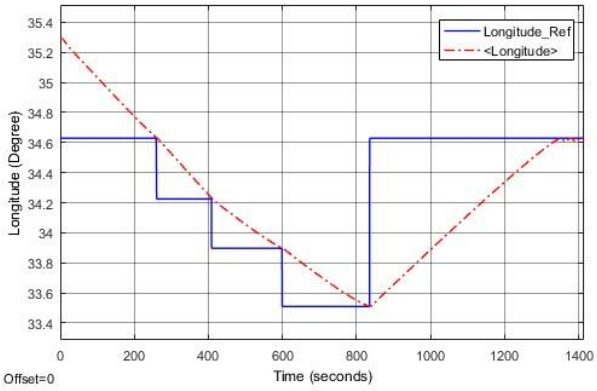

Figure 27. Longitude reference and response of longitudinal controller

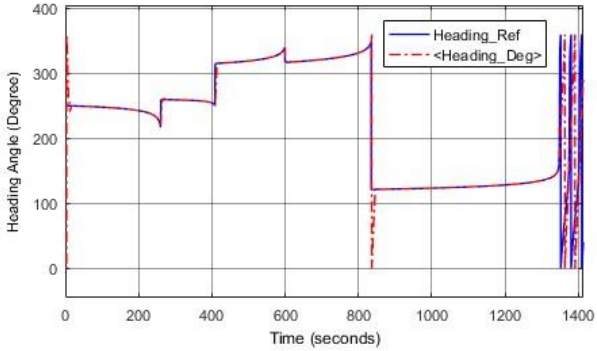

Figure 28. Heading response

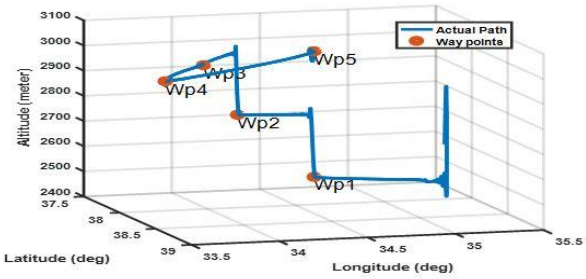

Figure 29. 3D Flight path of waypoint list

The heading response of the heading controller is given in Figure 28. It is clear from the Figure 28; aircraft tracks the reference-heading angle, which is generated by the trajectory generator block. Actually, heading reference is changing between -180 and +180 degree, but we convert this data to 0-360 degree because we get the data from X-Plane like this. In Figure 28, approximately at 825 seconds one spike is shown. However, this data is actually the same data (360 degree equals 0 degree) and it occurs from the discontinuity. Last part of the Figures 20-28 belong to loiter mode of the aircraft that is turn around the waypoint 5 at 3000 m sea level.

Figure 29 shows, the 3D vehicle position of the trajectory-tracking task. As it can be observed, the vehicle tracks the desired trajectory.

Figure 30. Roll and pitch response of the aircraft

In Figure 30, a snapshot of the aircraft is given during the flight.

6. Conclusions and Future Works

With this study, an autopilot control design is made to change or maintain the altitude, heading and forward speed in the fixed-wing flight mode of the Osprey V22 aircraft accordingly to a reference, which comes from the trajectory generator block. Software-In-the-Loop (SIL) simulation is used to evaluate the controls and algorithms, because it is easy and fast way to verify the controller, leading to minimize the cost and time. Raspberry Pi minicomputer, which is the hardware used in the system, was selected as the first step of creating the system necessary for Hardware-In-the-Loop (HIL) simulation. An embedded control system is made such that successful implementation of an autopilot

system is then run on the Raspberry Pi as a standalone application. Communication between Raspberry Pi and X-Plane is provided through their Ethernet port using UDP.

The future work will be based on developing robust controller, instead of classical PID, for vertical take-off /landing and transition mode for Osprey V22 aircraft. Then, a platform will be built, which aid autopilot systems study and design. This platform will allow to us to monitor the aircraft responses for a designed autopilot system with high degree of realism.

Acknowledgment

This work is supported by the Research Project Unit of Niğde Ömer Halisdemir University under Research Project (project no: FEB 2016/28 DOKTEP), Turkey.

Nomenclature

VTOL : Vertical Take-off and Landing
UAV : Unmanned Air Vehicle

References

1. Escareño, J., Salazar, S. and Lozano, R., *Modelling and Control of a Convertible VTOL Aircraft.* Proceedings of the 45th IEEE Conference on Decision & Control, San Diego, CA, USA, 2006 : p 69-74.
2. 43r5Miller, M. and Narkiewicz, J., *The application of General Model of Moving Object for Tiltrotor Stability Analysis*, Journal of Theoretical and Applied Mechanics, Warsaw, 2006, Vol. 44 No. 4, p 881-906
3. Malang, Y., *Design and control a Vertical Takeoff and Landing Fixed-Wing UAV*, Master of applied Science 2016. University of Toronto.
4. Sanchez, A., Escareño, J., Garcia, O. and Lozano, R., *Autonomous Hovering of a Noncyclic Tiltrotor UAV: Modeling, Control and Implementation.* Proceedings of the 17th World Congress The International Federation of Automatic Control Seoul, Korea, 2008. p 803-808.
5. Yongzhong, L., Danping, Y. and David, L., *Parameter Estimation Of Vertical Takeoff And Landing Aircrafts By Using A PID Controlling Particle Swarm Optimization Algorithm*, Applied Intelligence, 2016. 44: p 793-815.
6. Meyer, A. *X-Plane 9/10. X-Plane Operation Manual*, 2011.
7. Bittar, A., Figuereido, H.V., Guimaraes, P.A. and Mendes, A. C., *Guidance Software-in-The-Loop Simulation Using X-Plane and Simulink for UAVs*, 2014 International Conference on Unmanned Aircraft Systems (ICUAS), 2014. Orlando, FL, USA. p 993-1002
8. Figes Engineering, *Simulink Technical Source*, http://www.figes.com.tr/matlab/E-Technical-Kit. Simulink / index.html
9. Öner, K.T., Çetinsoy, E., Sırımoğlu, E., Hançer, C., Ünel, M., Akşit, F., Gülmez, K. and Kandemir, İ., *Mathematical Modeling and Vertical Flight Control of a Tilt-Wing UAV*, Turk J Elec Eng & Comp Sci, Vol.20, No.1, 2012. p 149-157.
10. McVeigh, M.A., Nagib, H., Wood, T. Kiedaisch, J. Stalker, A. and Wygnanski, I., *Model & Full Scale Tiltrotor Download Reduction Tests Using Active Flow Control*, 60th Annual Forum, Paner No 1, Baltimore, 2004. P 181-192.
11. J.M. Weakley, K.M. Kleinhesselink, D.H. Mason and D.G. Mitchell, *Simulation Evaluation of V-22 Degraded-Mode Flying Qualities*, 59 AHS Forum 2003, Paper No 135, Phoenix, AZ, USA, 2003.
12. Yonghua, F. and Jun, Y., *Design of Tiltrotor Flight Control System Using Optical Control*, Proceedings of the 26th Chinese Control Conference 2007, Zhangjiajie, Hunan, China, 2007. p 687-691
13. Muraoka, K., Okada, N., Kubo, D. and Sato, M., *Transition Flight of Quad Tilt Wing VTOL UAV*, 28th International Congress Of The Aeronautical Sciences, 2012. p 1-10.
14. Yüksek, B., Vuruskan, A., Özdemir, U., Yükselen, A. and İnalhan, G., *Transition Flight Modeling of a Fixed-Wing VTOL UAV*, Journal of Intelligent & Robotics Systems, vol 81, No. 1 International Publishing, 2016. p 1-23
15. Warsi, F., Hazry, D., Ahmed, S., Joyo, M. and et.al, *Yaw,Pitch and Roll Controller Design For Fixed-Wing UAV under Uncertainty and Perturbed Condition*, Signal Processing and its Applications, IEEE 10th International Colloquium, 2014. p 151-156.
16. Casau, P., Cabecinhas, D. and Silvestre, C., *Hybrid Control Strategy for Autonomous Transition Flight of a Fixed –Wing Aircraft*, IEEE Transactions on Control Systems Technology, vol 21, No.6 IEEE, 2013. p 2194-2211.
17. Papachristos, C., Alexis, K., Nikolakopoulos, G. and Tzes, A., *Model Predictive Attitude Control of an Unmanned Tilt-Rotor Aircraft*, IEEE International Symposium, Gdansk, Poland, 2011. p 922-927
18. Riberio, R.L. and Oliveria, N.F., *Using Autopilot Controllers Test Platform Using MATLAB/Simulink and X-Plane*, 40th Frontiers in Education Conference (FIE), Washington, DC, USA, 2010.
19. MathWorks, *Raspberry Pi Programming with MATLAB and Simulink*, https://www.mathworks.com/discovery/raspberry-pi-programming -matlab-simulink.html
20. Bittar, A. and Oliveira, N. M. F., *Central Processing Unit for an Autopilot: Description and Hardware-In-the-Loop Simulation*, J Intell Robot Syst, *2013*. Vol. 70. p 557-574
21. Andrievsky, B. and Fradkov, A., *Combined Adaptive Autopilot for an UAV Flight Control*. In 2002 IEEE International Conference on Control Applications,2002. p. 290–291.
22. Wu, H.Y., Zhou, Z.Y. and Sun, D., *Autonomous Hovering Control and Test for Micro Air Vehicle.* In Proceedings of the International Conference on Robotics and Automation, Taiwan, 2003 p. 528–533.
23. https://www.globalsecurity.org/military/systems/aircraft/v-22-flt-cntrl.htm [Available: 2018 29 June]
24. https://www.raspberrypi.org/help/what-%20is-a-raspberry-pi/ [Available: 2018 29 June]

25. Oktay T., Uzun M., Çelik H., Konar M., "*PID based hierarchical autonomous system performance maximization of a hybrid unmanned aerial vehicle* (HUAV)", Anadolu University Journal of Science and Technology, cilt.4, ss.1-10, 2017.
26. Oktay T., *"Performance Of Minimum Energy Controllers on Tiltrotor Aircraft*", Aircraft Engineering and Aerospace Technology, vol.86, no.5, pp.361-374, 2014

Appendix

A. Haversine Formula Matlab M.File

```
function d = haversine (lat1,lon1,lat2,lon2)
R = 6378.137;                % Radius of earth in km
dlat  = radians(lat2- lat1);
dlon = radians(lon2- lon1);
lat1= radians(lat1);
lat2= radians(lat2);
a = (sin(dlat./2))^2+cos(lat1)*cos(lat2)*(sin(dlon/2))^2;
c = 2 * asin(sqrt(a));
d = R * c * 1000;            %meters
end
```

Available online at www.dergipark.gov.tr

INTERNATIONAL ADVANCED RESEARCHES
and
ENGINEERING JOURNAL

Journal homepage: www.dergipark.gov.tr/iarej

International
Open Access

Volume 02
Issue 01

April, 2018

e-ISSN: 2618-575X

Research Article

A different method of using nitrogen in agriculture; Anhydrous ammonia

Cihangir Saglam [a], ***Fulya Tan*** [a,*]

[a]*Department of Biosystem Engineering,Faculty of Agriculture, Namık Kemal University, Tekirdağ, 59030, Turkey*

ARTICLE INFO

Article history:
Received 26 February 2018
Revised 20 March 2018
Accepted 25 March 2018

Keywords:
Fertilizer
Anhydrous ammonia
Nitrogen
Nitrogenous fertilizer

ABSTRACT

Nitrogen fertilization in vegetable production in agriculture is an inevitable application for plant growth and yield. The use of urea (46%)and nitrate (23-26%) for nitrogen fertilization is common in our country's agriculture. Nitrogen fertilization is carried out two or three times in different periods to meet the nitrogen requirement of the soil in wheat farming. Nitrogen fertilization is performed once in the pre-sowing period in developed countries such as America and Canada. Studies have also been carried out in order to ensure the use of similar nitrogen fertilization methods under the conditions of our country. Anhydrous ammonia, which is a raw material of nitrogenous fertilizers with 82.2% nitrogen content, was used for fertilizing as an environmental and economic method. The biggest problem in this application is the lack of equipment that can place the fertilizer into the soil due to the chemical properties of Anhydrous ammonia. In our work, we have developed equipment for the application of anhydrous ammonia and have carried out experiments on wheat farming in the region. Two different methods have been studied in the research; Anhydrous ammonia methods and traditional methods. The anhydrous ammonia method is a more advantageous method than the farmer condition method in terms of the parameters examined. Anhydrous ammonia method is a more environmentally and economical method due to the use of less fertilizer.

1. Introduction

The use of nitrogen fertilizer is necessary to ensure that production in agriculture is efficient and profitable. In our country, only 2 971 000 tones of nitrogenous fertilizer is used to meet 661 000 tones of pure nitrogen demand in cereal production [3]. As is known in our agriculture for the purpose of nitrogen fertilization; urea (46%), ammonium nitrate (26-34%), ammonium sulphate (21%) and compound fertilizers are used. In wheat production, fertilization is carried out in three different periods using different nitrogenous fertilizers. Anhydrous ammonia has been used for many years as a nitrogen source in cereal production especially in developed countries such as USA and Canada. Anhydrous ammonia accounts for 32% of the nitrogenous fertilizers used in agriculture [7]. In this study, traditional fertilization method and anhydrous ammonia fertilization method are compared. Nitrogen fertilizers and nitrogen content used in agriculture are given in Table 1.

Table 1. Nitrogenous fertilizers used in agriculture

Fertilizer	Formula	N content (%)
Ammonia	NH_3	82.2
Ammonium nitrate	NH_4NO_3	26-34
Ammonium sulphate	$(NH_4)_2SO_4$	21
Ammonium chloride	NH_4Cl	26
Urea	$(NH_2)_2CO$	46
Calcium nitrate	$Ca(NO_3)_2$	15.5
Sodium nitrate	$NaNO_3$	16
Calcium cyanamide	$CaCN_2$	20.6

Anhydrous ammonia (NH_3) has the highest amount of nitrogen with 82.2%. However, it is used as a raw material of nitrogenous fertilizers. Due to the chemical properties of anhydrous ammonia, its use is very limited [1]. Ammonia, classified as a chemical substance, is liquid under pressure. When the effect of the pressure is removed, it is in gas form [5,8]. Because of its chemical properties, ammonia application equipment must be in special construction. Due

* Corresponding author. Tel.: +90-530-775-3517
E-mail address: ftan@nku.edu.tr
Note: This study was presented at International Advanced Researches and Engineering Congress 2017 (IAREC'17)

to all these factors, the use of anhydrous ammonia as a nitrogen fertilizer is not yet available.

Within the scope of the project (TAGEM / 13-AR-GE / 45), we designed an equipment capable of applying ammonia fertilizer to the soil for nitrogen fertilization and we used for wheat farming. In this study, the advantages and disadvantages of traditional and anhydrous ammonia fertilization methods were evaluated.

2. Material and Method

2.1 Anhydrous ammonia

The physical and chemical properties of the anhydrous ammonia fertilizer used in the nitrogen fertilization method are given in Table 2 [5].

Because of these properties, anhydrous ammonia, which is assessed in the chemical class, requires the use of materials resistant to storage and abrasion under special conditions. Ammonia is used as a coolant in the air conditioning in our homes. For this reason, the most suitable use area for ammonia is agricultural fields with open application area.

2.2 Anhydrous ammonia application equipment

The anhydrous ammonia application equipment developed by our project team under the project is shown in Fig 1.

The equipment is arranged so that anhydrous ammonia fertilizer can be applied under the soil. The Knife type injection unit is shown in Fig 2.

Table 2. Physical and chemical properties of anhydrous ammonia

Physical form	Gas (liquid under pressure)
Color	Colorless
Smell	Heavy
Molecular weight	17.031 g / mol
Gas density	0.73 kg / m^3
The liquid density (-33.3 ° C)	681.9 kg / m^3
Critical temperature	132.44 ºC
Critical pressure	113 bar

Figure 1. Anhydrous ammonia application equipment

Figure 2. Knife type injection unit

Table 3. The properties of the equipment

Width	2200	mm
Tank volume	500	liter
Tank pressure	10	bar

The equipment consists of main frame, tank, feet, fasteners, dosing unit and control valves [2]. All the materials used in the equipment were resistant to anhydrous ammonia. The properties of the equipment are given in Table 3.

The main frame is made of 4 + 5 + 5 and the anhydrous ammonia is applied to the soil with only 4 front legs. The task of the rear legs is to cover the soil and prevent possible nitrogen losses.

2.3 Anhydrous ammonia application method (AAM)

In this method, anhydrous ammonia was applied once to the soil before sowing. Ammonia was applied at a dose of 22 kg da^{-1} according to soil analysis results. The anhydrous ammonia was injected 15-20 cm beneath the soil surface with application equipment and between 50 cm rows.

2.4 Traditional method (TM)

In the traditional method practiced by farmers, the application periods of fertilizers, the types of fertilizers used and the amount of fertilizers applied were recorded. It has not been intervened in the application condition of the farmer. The amounts and periods of fertilizer applied in wheat cultivation in the traditional method are given in Table 4.

As shown in Table 4, nitrogen fertilization in the traditional method was carried out in three different periods.

Table 4. The amounts and the periods of fertilizer applied in the traditional method

Period	I	II
Pre- sowing	10 kg urea (46 %)	10 kg TSP+10 kg urea
Tillering	18 kg urea (46 %)	20 kg urea (46 %)
Stemelongation	23 kg CAN (26%)	25 kg nitrate (26%)
Total nitrogen	18.9 kg da^{-1}	20.3 kg da^{-1}
Total fertilization	51 Kg	55 Kg

3. Results and Discussion

According to soil analysis, the amount of nitrogenous fertilizer that should be given to the soil was determined as 18 kg da^{-1}. The types of fertilizer used and the amounts used are given in Table 5. The total fertilizer usage amounts according to the methods are shown in Fig 3.

As shown in Table 5, 22 kg da^{-1} of anhydrous ammonia was used in the AAM method in two years to apply 18 kg da^{-1} pure nitrogen.

The total amount of nitrogen fertilizer used in the TM method was calculated as 51 kg in the first year and 55 kg in the second year. In TM method, the most used fertilizer type as nitrogen fertilizer was urea.

Fertilization was done three times in the TM method, but fertilization was done only once in the AAM method. This causes the farmer to use the tractor + equipment three times. This causes the consumed human energy and fuel consumption to be much higher.

The application of fertilizer in three periods also causes many disadvantages. These can be listed as cost increase, deterioration of soil porosity, increase of field traffic, use of excess fuel and negative environmental effects. It also causes the farmer to spend a lot more time.

Table 5. Quantities and types of fertilizers used in methods

Year	AAM	TM
I	Anhydrous ammonia	10 kg urea (46%) 18 kg urea (46%) 23 kg CAN (26%)
Application	1	3
Total	22 kg da^{-1}	51 kg da^{-1}
Difference	29 kg da^{-1}	
II	Anhydrous ammonia	10 kg TSP + 10 kg urea 20 kg urea (46%) 25 kg nitrate (26%)
Application	1	3
Total	22 kg da^{-1}	55 kg da^{-1}
Difference	33 kg da^{-1}	

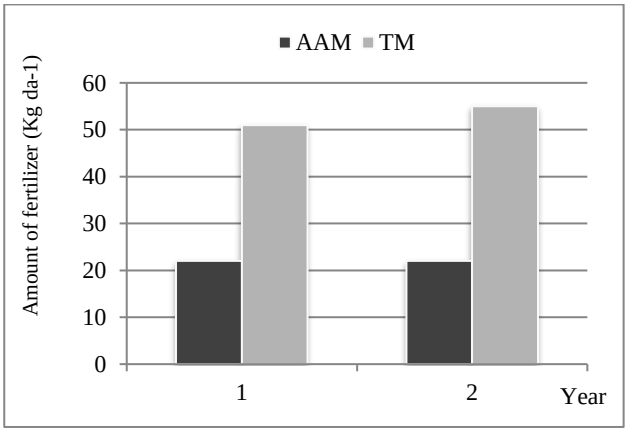

Figure 3. Amount of fertilizer according to methods

In the TM method, more fertilizer use was determined than in the AAM method. This amount was determined as 29 kg in the first year and 33 kg in the second year. It is clear from the results that in the TM method, much more fertilizer was used compared to the AAM method.

The grain yields according to the methods are shown in Table 6.

The AAM method showed positive results in terms of all the parameters examined according to TM method. Farmers usually prefer varieties with higher plant height. This is due to the increase in wheat stalk prices used in animal feeding in recent years. Wheat stalk is an important feedstock for livestock operations. However, due to insufficient production, wheat stalks gain value.

According to the AAM method, the plant height was 10 cm longer than the TM method.

In the AAM method; the most positive results were calculated in terms of characteristics such as spike length, number of grain in spike and grain weight in spike, which are important effects on yield.

Total grain yields (kg da^{-1}) according to the methods are shown in Fig. 4.

Table 6. The grain yields according to the methods

	Parameter	AAM	TM	Diff.
I	Plant height (cm)	103.56±6.1	93.40±2.6	10
	Spike length (cm) (cm)	8.54±0.82	8.11±1.0	0.43
	Number of grain in spike (number/spike)	42.56±7.14	33.80±8.66	8.76
	Grain weight in spike (g/spike)	2.41±0.47	1.93±0.59	0.48
	Gluten (%)	35.33±2.06	30.83±3.0	4.5
	Grain yield (kg da^{-1})	**892.15**	**728.33**	**163.82**
II	Plant height (cm)	95.73±10.1	90.08±4.5	5.65
	Spike length (cm) (cm)	8.36±0.84	7.11±1.0	1.25
	Number of grain in spike (number/spike)	43.73±7.18	35.63±9.11	8.1
	Grain weight in spike (g/spike)	1.59±0.29	1.28±0.42	0.31
	Gluten (%)	29.83±3.6	24.5±2.6	5.33
	Grain yield (kg da^{-1})	**744.80**	**695.44**	**49.36**

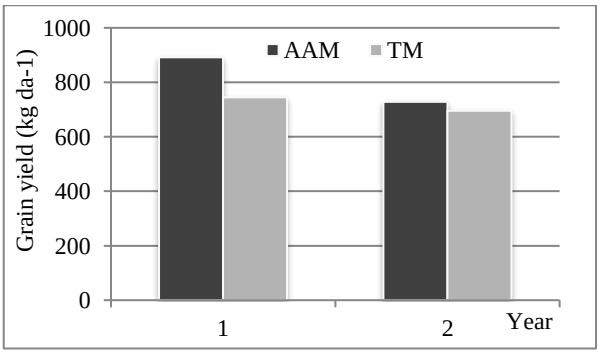

Figure 4. Total grain yields (kg da^{-1}) according to the methods

The grain yield in the AAM method were 163.82 kg da^{-1}, 49.36 kg da^{-1} higher than the TM method in year I and II, respectively. Similar results were found by [8, 9]. While it is known that nitrogen fertilizer application increases grain yield, application method and amount is also important [6 ,1, 9].

Compared with the TM, the number of grain in spike increased by 8.76 (number/spike) in year I and by 8.1 (number/spike) in year II.

Gluten values (%) according to the methods are given in Fig 5. The gluten value, which is a quality parameter, was found to be high in the AAM method. It was stated that the content of gluten for high-quality dough in bread making should be 28% [4].

In this respect, although nitrogen fertilization was applied once in the AAM method, the gluten content of wheat in AAM method was higher than the TM method. The gluten content in the AAM method were 4.5%, 5.33% higher than the TM method in year I and II, respectively.

The fertilizer and fertilizer costs according to the methods are given in Table 7.

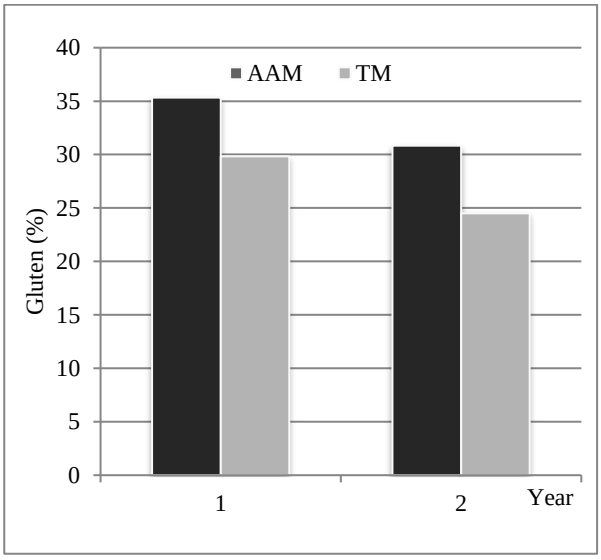

Figure 5. Gluten values (%) according to the methods

Table 7. The fertilizer costs according to the methods

Year		AAM	TM
I	Cost per unit ($/Kg)	0.25	0.32
	Fertilizer Cost($/da)	22.19	25.43
	Total Fertilizing Cost ($/da)	28.58	39.13
	Total cost ($/da)	165.57	176.12
II	Cost per unit ($/Kg)	0.25	0.29
	Fertilizer Cost($/da)	17.86	21.73
	Total Fertilizing Cost ($/da)	23.01	32.76
	Total cost ($/da)	151.69	161.43

* Prices are calculated according to the unit prices of the year 2014-2015.

There are significant differences between the methods in terms of cost for nitrogen fertilizer in wheat farming.

Total Fertilizing Costs in the AAM method were 10.55 $, 9.75 $ more economical than the TM method in year I and II, respectively. This shows that farmers spend more money on unit product costs. The advantages and disadvantages of methods are given in Table 7.

When the advantages and disadvantages of the methods are listed in terms of the examined parameters, the AAM method is found to be more advantageous than the TM method.

When all these results are evaluated; anhydrous ammonia can be used in the cultivation of our country for nitrogen fertilization. However, the biggest problem in the use of anhydrous ammonia in agriculture is that the application equipment is not available on the market. Anhydrous ammonia application areas in agriculture should be increased. In addition, intensive chemical use in agricultural applications causes environmental and groundwater pollutions. The use of fertilizer in intensive quantities increases the harmful effects by contamination of both soil and groundwater. It is known that the use of fertilizer is inevitable for high yield. For this reason, effective use of fertilizer is important.

In this study, positive results were determined in the anhydrous ammonia method according to the parameters examined.

3. Conclusions

According to the results of this study; use of anhydrous ammonia is recommended in terms of yield parameters and economic factors.

Acknowledgment

This study supported by the Republic of Turkey Ministry of Food, Agriculture and Livestock under research and development project Research Project (project no: 13/45), Turkey.

Table 8. Advantages and disadvantages of methods

	AAM	**TM**
Amount of fertilizer	🙂	🙁
Human work power	🙂	🙁
Environmental impact	🙂	🙁
Field traffic	🙂	🙁
Yield	🙂	🙁
Cost	🙂	🙁

Nomenclature

AA	:	Anhydrous ammonia
AAM	:	Anhydrous ammonia method
TM	:	Traditional method
TSP	:	Triple super phosphate
CAN	:	Calcium ammonium nitrate
NH_3	:	Ammonium

References

1. Akar, G., Tan, F., Sağlam C., Aksoy A., *Susuz Amonyak Gübresinin Uygulama Olanakları ve Uygun Ekipman Geliştirilmesi*. TAGEM /13/AR-GE/ 45. Araştırma-Geliştirme Destek Programı Proje Sonuç Raporu. 2016, Tekirdağ**.**
2. Akar, G., Tan, F., Sağlam C., Aksoy A., *Susuz Amonyak Uygulama Ekipmanının Geliştirilmesi ve Tarla Denemeleri*. 29. Ulusal Tarımsal Mekanizasyon ve Enerji Kongresi Bildiri Kitabı. 2-5 Eylül 2015.,S.247- 253. Diyarbakır.
3. Colakoglu, H., Cokuysal, B. and Cakıcı, H. *Production and Consumption of Fertilizers in Turkey*. The place and importance of potassium in agriculture. Workshop, 2005. October, 3-4. Eskisehir,Turkey.
4. Erenkul O., Oncan F., Erenkul A., Yava İ., Engün B., Koca Y.O. *İleri Ekmeklik Buğday Hatlarında Verim ve Bazı Kalite Özelliklerinin Belirlenmesi.* Türkiye VI. Tarla Bitkileri Kongresi, 5-9 Eylül 2005, Antalya Cilt,I, Sayfa 111-116.
5. Hanna, M. 2001. *Improving the uniformity of Anhydrous ammonia application*. Iowa State University Extension. PM 1875.
6. Öztürk İ. ve Gökkuş A. *Azotla Gübrelemenin Bazı Ekmeklik Buğday Çeşitlerinin Verimi ve Kalitesine Etkileri*. Ankara Üniversitesi Ziraat Fakültesi Tarım bilimleri dergisi 2008, 14 (4) 334-340.
7. Terry, D. L. and B. J. Kirby, *Commercial fertilizers*. 2006. Association of American Plant Control Officials Inc. and The Fertilizer Institute. Lexington, KY.
8. Woli, K.P. Femandez, F.G. Sawyer, J.E. Stamper, J.D. Mengel, D.B. Barker, D.W. and Hanna M.H. *Agronomic Comparison of Anhydrous Ammonia Applied with a High Speed-Low Draft Opener And Conventional Knife Injection in Corn*. 2014. Agronomy Journal, 106(3), 881-892.
9. Wyckoff, M.R. *Evaluatıon of Anhydrous Ammonıa Applıcatıons ın Wınter Wheat*. 2009. Kansas State Unıversıty Masters of Science. Manhattan, Kansas.

Available online at www.dergipark.gov.tr

INTERNATIONAL ADVANCED RESEARCHES
and
ENGINEERING JOURNAL

Journal homepage: www.dergipark.gov.tr/iarej

e-ISSN: 2618-575X

International
Open Access

Volume 02
Issue 01

April, 2018

Research Article

Effects of pretreatments on the production of biogas from cow manure

Esin Hande Bayrak Işık [a,*], Fatih Polat [a]

[a]*Gaziosmanpaşa University, Almus Vocational School, Tokat, Turkey*

ARTICLE INFO

Article history:
Received 09 January 2018
Revised 03 February 2018
Accepted 06 February 2018

Keywords:
Biogas
Cow manure
Pretreatments
Water solubility

ABSTRACT

In this study, some pretreatments were applied to cow manure to determine water solubility and biogas production. Aqueous phases containing 10 % solids by mass were prepared in the study. Chemical substances (NaOH), which were as much as 10, 15, and 20 % of the solids by mass, were added to the aqueous phases, and then they were subjected to microwave and hotplate thermal pretreatments separately (for 15, 30, 60 minutes). Following the pretreatments, the water solubility percentages of the solid materials were determined in the un-pretreated and pretreated aqueous phases. The pH of the aqueous phases, which yielded the highest water solubility, was adjusted to 7 using acid. Afterwards, the aqueous phases were incubated at 35 °C for 32 days in an incubator, and biogas and methane measurements were made in aqueous phases every 4 days. As a result of the study, maximum water solubility was found to be 92.8% (by mass), maximum biogas yield 378 mL/1g, and dry solids and maximum methane content values 41%.

1. Introduction

Biogas is a gas mixture which is produced by the fermentation of organic-based waste/residues in an anaerobic environment. It is colorless - odorless, lighter than air. It burns with a bright blue flame and comprises 40-70% methane, 30-60% carbon dioxide, 0-3% hydrogen sulfide, and very little nitrogen and hydrogen depending on the composition of organic substances in its composition.

The thermal value of the biogas comes from the flammable methane gas in its composition. The amount of heat obtained from 1 m^3 biogas is 4700-5700 kcal/m^3 [1].

The effective heat of 1 m^3 biogas is equivalent to the following energy values:
0,62 liter of kerosene
1,46 kg of charcoal
3,47 kg of wood
0,43 kg of butane gas
12,3 kg chip
4,70 kWh electric energy

Fuel equivalents of 1 m^3 biogas:
0,66 liter diesel
0,75 liters of gasoline
0,25 m^3 propane [1].

Various wastes such as animal waste (feces of cattle, horses, sheep, and poultry animals, wastes from slaughterhouses, and waste from the processing of animal products), vegetal waste (unprocessed parts of plants and waste from the processing of vegetal products such as finely chopped stalks, straw, stubble and corn residues, sugar beet leaves and grass residues), and urban and industrial wastes with organic content (sewage and bottom sludge, waste from paper industry and food industry, dissolved organic matter and highly concentrated industrial and domestic wastewater) are used in biogas production.

Table 1 presents biogas yields and methane quantities in biogas that can be obtained from various sources [1].

Solid animal wastes are regarded as the ideal source for biogas production (65% methane, 35% CO_2) after a

* Corresponding author. Tel.: +90 356 252 1616 (5511); Fax: +90 356 411 3030.
E-mail address: esinhande.bayrak@gop.edu.tr
Note: This study was presented at International Advanced Researches and Engineering Congress 2017 (IAREC'17)

biological treatment. The resulting biogas is of great significance for both electricity and heat generation [2].

Daily and annual wet manure quantities that can be obtained on the basis of animal weight are as follows:

- 5-6% kg-wet manure/day of live weight of cattle
- 4-5% kg-wet manure/day of live weight of sheep-goat
- 3-4% kg-wet manure/day of live weight of chicken [1].

Table 2 presents the amounts of annual wet manure that can be obtained on the basis of animal weight and Table 3 presents the biogas quantities that can be produced by the type of manure [1].

Table 1. Biogas yields that can be obtained from various sources and methane quantities in biogas [1].

SOURCE	Biogas Yield (liter/kg)	Methane Ratio (% by volume)
Cattle Manure	90-310	65
Poultry Manure	310-620	60
Pig Manure	340-550	65-70
Wheat Straw	200-300	50-60
Rye Straw	200-300	59
Barley Straw	290-310	59
Corn Stems and Residues	380-460	59
Flax, Hemp	360	59
Grass	280-550	70
Vegetable Residues	330-360	Variable
Various Agricultural Residues	310-430	60-70
Peanut Shell	365	-
Fallen Tree Leaves	210-290	58
Algae	420-500	63
Wastewater Mud	310-800	65-80

Table 2. Annual wet manure quantities that can be obtained on the basis of animal weight [1].

Number of Animals	Animal Species	Wet Manure Quantity (ton/year)
1	Cattle	3,6
1	The ovine	0,7
1	Poultry	0,022

Table 3. Biogas yield that can be produced depending on manure type [1].

Manure Type	Manure Quantity	Biogas Quantity that can be Obtained (m^3/year)
Cattle	1 ton	33
The ovine	1 ton	58
Poultry	1 ton	78

When Turkey's energy statistics are examined, it can be seen that animal and vegetal residues make up 9% of the total energy production and 4% of the total energy consumption. The share of animal manure among other items is big. In our country, animal chip is utilized for heating and cooking. The use of animal manure on agricultural lands is more economical than converting it to energy by burning. Animal manure has superior properties in comparison to artificial fertilizers. In addition to providing soil nutrients, it also improves soil structure. Preventing the burning of animal chip and ensuring its use in agricultural lands is only possible by giving an energy substitute to the rural area. This substitute energy is biogas, which can also be obtained from animal manure [3].

Utilization of animal wastes as biogas is also important from an environmental point of view.

The unpleasant smell which is one of the biggest problems arising from animal husbandry facilities will be removed by anaerobic digestion of waste. Raw manure that is kept outdoors in farm raising animals can leak into ground or surface water with rainwater or wind. This causes eutrophication in surface waters and pollution in ground waters. With biogas investment, these negative effects will come to a halt.

During the maturation of the manure in biogas generators, an environment based on a natural decomposition basis is created, and so reproduction of harmful parasites and pathogenic microorganisms become impossible and thus waste environment can not threaten the environment and human health [4].

A review of the related literature in the light of these facts has yielded the following findings:

Kearney et al. found the daily biogas production produced by some bacteria found in cattle manure in an anaerobic medium in the laboratory at 35 °C, for 25 days, and at pH 7.6 conditions as 510-620 ml/day and the methane ratio as 42-50% [5].

Pound et al. conducted a study to compare the amounts of biogas produced from cattle manure mixed with urea and urea-free compressed sugar cane in anaerobic conditions. It was found that when they increased the percentage of compressed sugar cane in the mixture, the pH of the slurry in fermentation decreased, and then biogas production slowed down respectively. It was determined as a result that biogas production was directly proportional to the amounts of pH of the slurries [6].

Sözer and Yaldız determined an optimum biogas production yield by mixing banana greenhouse wastes and cattle dung at various ratios. The study was conducted by adding 15%, 30%, 45%, 60% and 75% banana greenhouse wastes into cattle dung at 37 ºC, in laboratory biogas generators with continuous flow, for

15-day waiting period. As a result, the highest raw material specific methane production rate was determined as 0,149 L g^{-1} organic dry matter/day from 30% banana greenhouse waste and 70% cattle dung mixture [7].

Kobya studied biogas production from cattle dung at different temperatures (20, 25, 30, 35 °C). In the study, T_{Gaz}, T_{CH4}, TOM changes were examined for various temperatures and time periods and related model equations were obtained. It was found that at 35 °C, a total of 8.630 liters of biogas was obtained from 80g dry cattle dung, while 9.670 liters of biogas were obtained from 80g fresh cattle dung. It was found as a result of the study that as the temperature increased, the degradation rate of T_{Gaz}, T_{CH4}, TOM increased by time [8].

By using laboratory scale biolithic reactors, Aslanlı tried to determine the effect of boron compounds on biogas production from animal wastes. Boron compounds were added to the reactors at different doses and at different temperatures. Cattle dung was diluted with tap water at a ratio of 1:1 g/ml and then incubated for 35 days in anaerobic conditions at 25, 37 and 50 °C for biogas production. Ammonium tetraborate, borax, boric acid, lithium tetraborate and potassium tetraborate were added to the reactors at different doses. Effective biogas production was observed in the reactor with maximum level ammonium tetraborate (0,50 g/L) at 25 °C incubation and the reactor with borax (0,86 g/L) at 37 °C. On the other hand, boron compound was observed to have no effect on biogas production [9].

Varinli determined the optimum thermal pretreatment temperature for the maximum biogas production from apple marc and evaluated the methane production potential as a function of the thermal pretreatment temperature. Thermal pretreatment was applied at 11 different temperatures such as 25 °C, 50 °C, 70 °C, 80 °C, 90 °C, 100 °C, 110 °C, 120 °C, 130 °C, 150 °C and 170 °C. Measurements were made in reactors operated for 42 days and the biogas content of gas samples taken at periodic intervals was determined by gas chromatography. The highest biogas production was obtained from samples pretreated at 150 °C, while the lowest was obtained from pretreatment samples at 110 °C. More gas production was achieved in samples with thermal pretreatment than the samples without thermal pretreatment. Experimental studies have shown that thermal pretreatment has a positive effect on biogas and methane production from apple marc [10].

Ardıç studied increasing the biogas production yield from cow dung. To do this, he separately added H_2SO_4, H_3PO_4, HNO_3, NaOH and KOH as much as 5%, 10%, 15% and 20% of the solid matter in the mixture to aqueous mixtures containing solids as much as 10% of cow dung, and then thermal and thermochemical pretreatments were applied at one, two and three hour-intervals at room temperature and water boiling temperature. The aqueous phases which yielded the maximum water solubility were applied anaerobic treatment at pH=7 and 30 °C for 30 days, and then their biogas and methane volumes were determined by time. At the end of the study, the maximum water solubility of the solid material in the cow dung was found to be 29,7% and the maximum methane production yield was 352,37 $mLCH_4/gKM$. This value was obtained from a three-hour thermochemical pretreatment using NaOH, it was observed that pretreatments conducted using NaOH were found to improve the water solubility of the solid material in cow dung and the biogas, methane production efficiency from cow dung [11].

In this study, cow manure was pretreated so that water solubility and biogas production could be determined. The slurry with 10% solid content added no chemical substance and the slurry with 10% solid content added a chemical substance were subjected to microwave and hotplate thermal treatment at room temperature.

2. Material and Method

2.1. The Pretreatments

Cow manure used as raw material in the study was prepared by drying, grinding and subjecting it to sieve analysis to ensure homogeneity. In the experiments, aqueous phases containing 10% solids by mass were used. An alkaline pretreatment was carried out by adding NaOH solution of 50% as much as 10%, 15%, and 20% of the solids to the aqueous slurry containing 10% solids by mass.

The thermal pretreatments, on the other hand, were carried out by keeping the slurry with 10% solid content by mass in a 700 W microwave oven under a reflux or on a hotplate under a reflux for 15, 30 and 60 minutes.

2.2. Determining Water Solubility and Biogas Yield

The pretreated aqueous cow manure samples were filtered through glass cotton whose fixed weight was measured. The filtration process in the aqueous mixtures continued until the filtered water was transparent. The solid collected in the glass cotton after the filtration process was dried at 70°C - 80°C in the incubator until it was possible to get the weight and their weights were recorded to find the percentage of water solubility. The transactions were made in triplicate.

Samples with the highest water solubility were selected for analysis after dissolution experiments in water. To adjust the pH of the selected aqueous phases to 7, H_2SO_4 solution was added to the aqueous phases which had been subjected to basic pretreatment. The bottles to be filled in 10% aqueous phases obtained from the pretreatment conditions were wrapped with foil to prevent light transmission so that anaerobic disintegration

could take place. All aqueous phases were grafted to achieve methane formation. The bottles in which the samples and the vaccine solution were filled in were capped. Certain amounts of nitrogen gas were filled into the capped bottles in which certain amounts of samples were placed so that the oxygen in the bottles can be removed completely. Bottles were left to anaerobic biodegradation in an incubator set at 35 °C to ensure optimum conditions. The volume of biogas and methane emerging in the bottles placed in the incubator was measured with Orsat Gas Analyzer.

First of all, the biogas volume was determined at this device. The entire biogas was then taken up in the absorption column on the device with a CO_2 absorber 33% KOH solution through a level bottle, and then the gas was flushed several times with this solution to assure the absorption of all CO_2.

The reaction of CO_2 with KOH is given in the following equation.

$$CO_2 + 2KOH \rightarrow K_2CO_3 + H_2O \quad (1)$$

The remaining gas was then passed to the burette where the other gas level on the instrument was measured, and the methane volume was read here.

3. Results and Discussion

Figure 1 shows the change in the water solubility percentages by mass based on the applied pretreatments.

PRETREATMENTS (Water Solubility):

1. Un-pretreated raw manure
2. 30 minutes MD
3. 15 minutes HP
4. 10% NaOH addition
5. 20% NaOH addition + 15 minute HP
6. 10% NaOH addition + 15 minute MD
7. 15% NaOH addition + 15 minute HP
8. 15% NaOH addition + 30 minute MD

As is shown in Figure 1, the best pretreatment condition in which cow manure dissolved was 20% NaOH addition for 15 minutes HP pretreatment with 92.8% value. All pretreatments increased the water solubility of solid material.

According to pretreatments, the change in the volumetric cumulative biogas amounts per gram of dry solids in standard conditions is given in Figure 2.

PRETREATMENTS (Biogas Production):

1. 10% NaOH addition
2. 15% NaOH addition + 30 minute MD
3. 20% NaOH addition + 15 minute HP
4. 10% NaOH addition + 15 minute MD
5. 15% NaOH addition + 15 minute HP
6. 30 minutes MD
7. 15 minutes HP
8. Un-pretreated raw manure

When the cumulative biogas amounts obtained at the end of the anaerobic treatment was examined, it was observed that the highest amount of biogas was obtained from 15% NaOH addition + 30 min MD pretreatment condition with 378 mL value. The methane content of the biogas obtained in this pretreatment condition was 41%. Under all conditions, there was an increase in the amount of biogas production compared to that of the unprocessed raw cow manure.

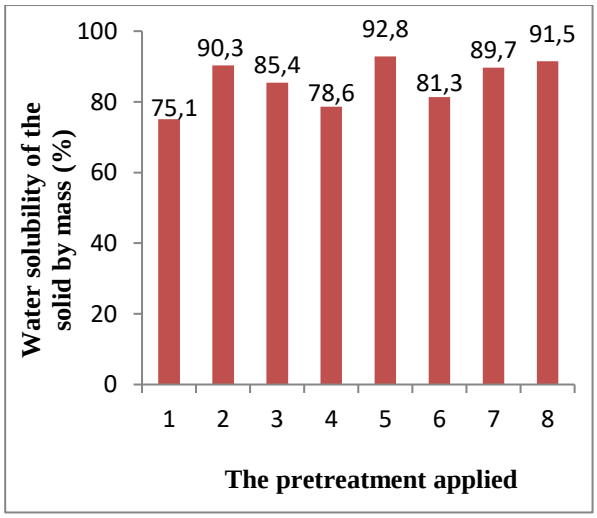

Figure 1. The change in water solubility percentage of solid material as a result of pretreatments

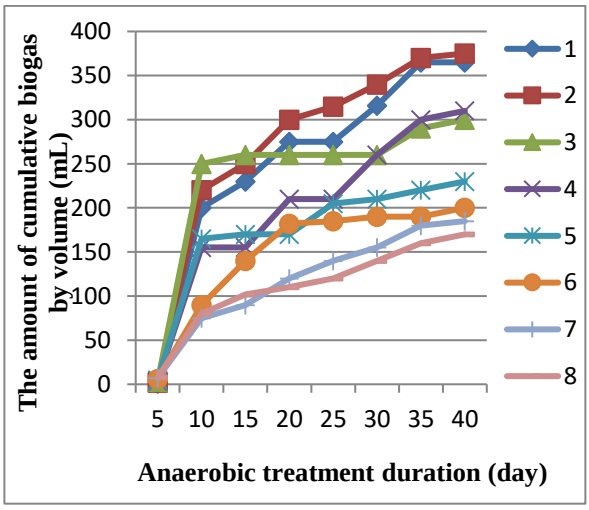

Figure 2. The change in cumulative biogas quantities

4. Conclusion

As a result of the study, it was found that the best water solubility was achieved with 20 % NaOH addition + 15 minutes HP pretreatment which yielded 92.8% achievement. All the pretreatments were shown to increase water dissolution.

The highest amount of cumulative biogas was obtained from 15% NaOH addition + 30 min MD pretreatment condition with 378 mL value. The biogas production yields obtained from all pretreatments were higher than that of the un-pretreated sample. All pretreatments increased biogas production efficiency as well as increasing water dissolution. Thus, the positive effects of pretreatments on the biogas production efficiency were revealed.

When compared to similar studies, the results of this study indicated that pretreatments increased water dissolution and biogas production. Given the positive effects of both chemical and thermal pretreatments on biogas production, applying these pretreatment conditions in biogas production plants will make a great contribution to production and provide economic benefits.

In conclusion, biogas production from animal wastes provides both electricity and heat production, as well as providing many positive social, economic and environmental results.

References

1. EIE web page. [cited 2017 29 June]; Available from: http://www.eie.gov.tr/yenilenebilir/biyogaz.aspx
2. Tolay, M. and Yamankaradeniz, H., *Biogas Production from Animal Wastes*, VII. National Clean Energy Symposium, UTES'2008, Istanbul, p.259-264.
3. Alibaş, K., Ulusoy. Y, and Tekin. Y, *Biogas Production*, 2006.
4. Gümüşçü, M. and Uyanık, S., *Biogas and Biofuels Outcome from Animal Wastes in Southeastern Anatolia*, TMMOB Institutional Engineering Review, Issue: 118, 2010, p.59-65.
5. Kearney, T. F., Larkin, M.J. and Levett, P.N. *Metabolic Activity of Pathogenic Bacteria During Semicontinuous Anaerobic Digestion Applied*, Applied and Environmental Microbiology, 1994, vol.60, No.10, pp. 3647-3652.
6. Pound, B., Done, F. and Preston, T.R. *Biogas Production from Mixture of Cattle Slurry and Pressed Sugar Cane Stalk, with and without Urea*, CEDIPCA, CEAGANA, 1981, Aptd 1256 Santo Domingo, Dominican Republic, Trop. Anim. Prod., pp.1-6.
7. Sözer, S., and Yaldız, O., *A Study on the Determination of the amount of Biogas that can be Produced as a result of Mesophilic Fermentation from Banana Greenhouse Wastes and Cattle Dung Mixtures*, Akdeniz University, The Journal of Agricultural Faculty, 2011, 24 (2): 75-78.
8. Kobya, M., 1992, *Biogas Production from Cattle Dung and Design of a Biogas Plant for Erzurum Conditions*, Atatürk University, Graduate School of Natural and Applied Sciences, Department of Environmental Engineering, Master Thesis, 75s.
9. Aslanlı, Ş., 2009, *Investigation of the Effectiveness of Various Boron Compounds on Biogas Production from Animal Wastes*, Harran University, Graduate School of Natural and Applied Sciences, Department of Biology, Master Thesis, 85s.
10. Varinli, F., 2010, *Effect of Thermal Pretreatment on the Production of Biogas and Methane from Apple Marc*, Erciyes University, Graduate School of Natural and Applied Sciences, Department of Environmental Engineering, Master Thesis, 54s.
11. Ardıç, İ., 2009, *Investigation of the Effects of Thermal, Chemical and Thermochemical Pretreatments on Biogas Production Yields from Cow*, Mersin University, Graduate School of Natural and Applied Sciences, Department of Environmental Engineering, Doctorate Thesis, 228s.

Available online at www.dergipark.gov.tr

INTERNATIONAL ADVANCED RESEARCHES
and
ENGINEERING JOURNAL

Journal homepage: www.dergipark.gov.tr/iarej

e-ISSN: 2618-575X

International
Open Access

Volume 02
Issue 01

April, 2018

Research Article

Treatment of fruit juice concentrate wastewater by electrocoagulation: Optimization of COD removal

Habibe Elif Gulsen Akbay [a]*, ***Ceyhun Akarsu*** [a], ***Halil Kumbur*** [a]

[a] *Mersin University, Engineering Faculty, Department of Environmental Engineering, 33343, Mersin, Turkey*

ARTICLE INFO

Article history:
Received 03 February 2018
Received 09 April 2018
Accepted 10 April 2018

Keywords:
COD removal
Electrocoagulation
Fruit juice
Operating cost
Optimization
Wastewater treatment

ABSTRACT

Depending on the growing population and the developing industry, wastewater is encountered with different characteristics and higher temperatures each passing day. For this reason, researches are under way for new treatment methods that will respond to needs in terms of cost and remediation. In this study, treatment of fruit juice concentrate wastewater has been examined by electrocoagulation (EC). For this purpose, the optimum conditions for the best COD removal were investigated. In the EC process, different electrodes (aluminum, iron and steel), pH (5.5,7, 8 and 9) and current (0.6, 0.8 and 1.0 A) were studied, respectively. The results showed that the optimum COD and color removal were obtained as 66%, 98% respectively when the applied electrode pair were Al(+)/Fe(-), cell current was 0,8A and wastewater pH was 5.5 in 10 min. Also, the operating cost was calculated for the optimized treatment conditions of 1 m^3 fruit juice wastewater as 2.69 US$.

1. Introduction

High amount of water is used in the juice industry thus it produces a high amount of wastewater [1]. These wastewater contain high concentrations of organics due to usage of fruits or sugar [2]. The typical juice industry produces 10 L wastewater per litter of juice. A wide range of fruits are used to manufacture juice. These include apple, apricot, rosehip, peach, cherry, oranges. So far, conventional treatment methods such as aerobic and anaerobic [3-5], combination of biological and chemical processes [6], membrane filtration [7], proton exchange membrane fuel cell [8], membrane bioreactor [9] have been applied for fruit juice wastewater.

If it is considered that so many different fruits and more than one species of each fruit participate in production; it can be said that the wastewater contains chemicals in a very wide range of different structures. Also, it contains a lot of organic acids which were added as preservatives and additives during fruit juice production. Therefore, there is a need for alternative treatment methods that can treat different characteristic wastewaters.

Recent studies have shown that electrochemical techniques can provide a good opportunity to prevent and remedy pollution problems due to strict environmental regulations. The use of electrochemical technologies for the treatment of organic pollutants contained in industrial wastewaters has received a great deal of attention in recent years [10]. Electrocoagulation (EC) is an emerging technology that combines the functions and advantages of conventional coagulation, flotation, and adsorption in wastewater treatment [11]. Studies show successful results in treatment of textile wastewater [12-14], food and protein wastewater [15], landfill leachate wastewater [16], pulp and paper mill wastewater [17,18], arsenic in wastewater [19], pesticides in wastewater [20], tannery wastewater [21], oil refinery wastewater [22] by electrocoagulation process. According to literature, the EC process can be put forward as an advanced treatment method because of its efficiency, low energy requirement, and lower and more stable sludge production compared with conventional treatment methods [23].

The objective of this research was treatment of an actual industrial wastewater by electrocoagulation and determine

* Corresponding author. Tel.: +90 (324) 361 0001-17100; Fax: +90 (324) 361 0032.
E-mail address: elifgulsen@mersin.edu.tr
Note: This study was presented at International Advanced Researches and Engineering Congress 2017 (IAREC'17)

optimum operating conditions. Also, cost efficiency was calculated based on parameters such as electrode mass loss, voltage, current etc. and obtained results were compared with the conventional treatment methods in the literature.

2. Materials and methods

2.1 Wastewater characteristics

The studies were carried out on the treatment of fruit-juice concentrate production wastewater with a low (1920 mg/L) COD content for this kind of industries. The wastewater used in this study was collected from a fruit juice factory which located in Mersin, Turkey. The wastewater characteristics are listed in Table 1.

Table 1. Wastewater characteristics

Parameter	Unit	Value
pH	-	5.53
Alkalinity	mg $CaCO_3$/L	46
Color	Pt-Co	290
Conductivity	µS/cm	817
TN	mg/L	10.06
COD	mg/L	1920
TS	mg/L	2976
VS	mg/L	1666.60
TSS	mg/L	1334.10
VSS	mg/L	452.0

2.2. Chemicals and analytical method

Sodium hydroxide (NaOH; 98%) and sulphuric acid (H_2SO_4; 98%) used in the experiments were obtained from Merck. In addition, NaCl was used to adjust the conductivity value in the EC experiments. The pH value of the samples was adjusted with the WTW Multi 340i portable multiparameter meter. Velpa Multi Position magnetic stirrer was used for the EC experiments. AA Tech ADC 3303D power supply was used as the current and voltage regulating source and iron, aluminium, steel electrodes were used to perform the electrocoagulation experiments. A Hettich EBA 20 centrifuge (6000 rpm, 5 min) was used to separate the sludge from the samples at the end of the EC experiments. The Hach Lange DR 3900 VIS spectrophotometer was used for the colour removal analysis of the EC experiments. All the chemical analyses were carried out in accordance with the Standard Methods for Examination of Water and Wastewater [24].

2.3. Electrocoagulation (EC) experiments

In order to determine the maximum removal efficiency of COD in EC process, various parameters such as pH (5.5, 7-8-9), current (0.6-0.8-1.0 A) and electrode combinations (aluminium, iron and steel) were investigated in different time intervals (10-20-30-40-50-60 min). Each experiment was carried out in a 1000 mL glass reactor and 800 mL of wastewater was used for the experiments. The reactor contains two electrodes of the same dimensions of 60 mm x 90 mm; one anode and one cathode electrode. The total effective anode electrode area was 54 cm^2, and the distance between electrodes was 2 cm for the each EC reactor. All the experiments were repeated twice and the average values have been reported. The experimental setup is shown in Figure 1.

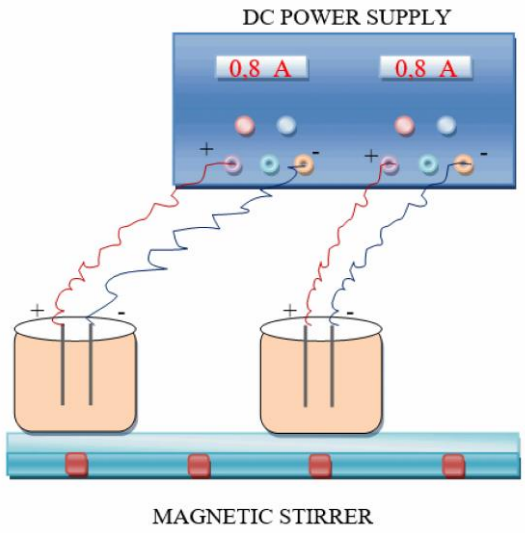

Figure 1. The experimental setup

3. Results and discussion

3.1 Optimum electrode determination

In the first stage of the EC process, the electrode pair that provides the best COD removal was determined. For this purpose, different electrode combinations such as Fe(+)/Al(-), Fe(+)/St(-), Al(+)/Al(-), Al(+)/St(-), Fe(+)/Fe(-), Al(+)/Fe(-) were investigated by keeping pH (5.5), conductivity (2000µS/cm) and current (0.8 A) constant. The best COD removal was achieved with a pair of Al(+)/Fe(-) electrodes at a rate of 66% in 10 min. Therefore, the next experimental step was continued with this electrode pair. The effect of electrode pairs on COD removal is presented in Figure 2.

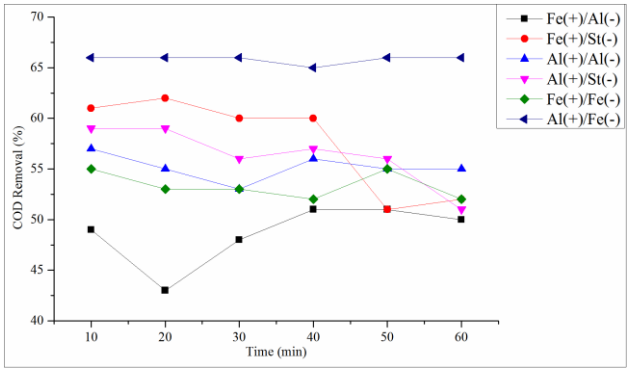

Figure 2. The effect of electrode pairs on COD removal

3.2 Effect of pH

pH is an important operating factor affecting the performance of the EC process also the pH of the medium is constantly changing during the wastewater treatment. In some studies, the desired yield is obtained at a wide pH range and no initial pH regulation is needed in the system [25]. In this study, neutral and basic pH values such as 7, 8 and 9 have also been examined for the reason that the present wastewater sample is already at acidic pH (5.5). Initial pH values were adjusted with 0.1 M H_2SO_4 and 0.1 M NaOH solutions. Conductivity was set to 2000 µS/cm and the power supply is operated at 0.8A. It has been determined that the best COD removal (66%) occurs at the original pH of the wastewater in acidic conditions in 10 min. Can (2014) also found a similar result for this kind of wastewater. The researcher reported that removal efficiency reached the highest value (52%) at pH 6 in 60 min[26]. The effect of initial pH value on COD removal is given in Figure 3.

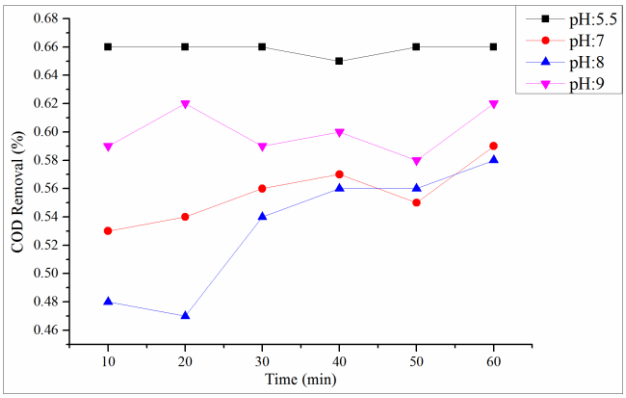

Figure 3. The effect of initial pH value on COD removal

3.3. Effect of current on electrocoagulation

The amount of current density affects the production rate of metal ions dissolving in the anode, the bubble velocity and the size of the cathode. Accordingly, the quantity, structure and formation of the flocks are also affected. Also, the current density should be checked to avoid excessive oxygen and possible temperature increase [27]. Because of the formation of small bubbles at low current densities, sedimentation is more dominant than flocculation in the removal of contaminants [28].

Experiments were carried out at 0.6 A, 0.8 A and 1.0 A in the study. Conductivity was set to 2000 µS/cm and the pH was 5.5. It has been determined that the best COD removal (66%) occurs at the 0.8 A in 10 min. The effect of current on COD removal is given in Figure 4.

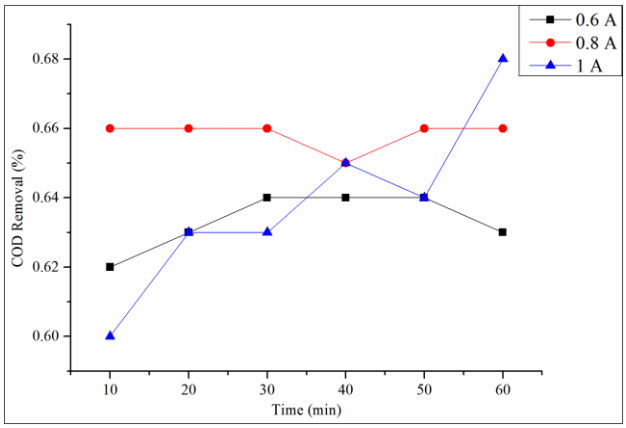

Figure 4. The effect of current on COD removal

3.4. Operating cost

The operating cost includes electrode cost, electrical energy cost, labor, maintenance and etc. In this study, energy and electrode material costs are taken into account as major cost items, in the calculation of the operating cost as kWh per m^3 wastewater of COD removed. The calculations were made by using Equation (1);

$$\text{Operating cost} = a^* C_{encrgy} + b^* C_{electrode} \quad (1)$$

Where C_{energy} and $C_{electrode}$, are consumption quantities per kg of COD removed, which are obtained experimentally. Unit prices, a and b, given for Turkey Market, September 2017, are as follows:

(a) electrical energy price 0.06 US$/kWh.

(b) electrode material price 4.57 US$/kg for aluminium (anode)

Cost calculations showed that, in the case of aluminium electrode, operating cost is approximately 2.69 US$ per kg COD removed.

4. Conclusion

In this study, it has been tried to treat fruit juice wastewater by advanced treatment methods. Experiments were carried out using electrocoagulation process as the advanced treatment method. Chemical oxygen demand and colour were used as optimization parameters. Various operating parameters, such as current density, initial pH, and electrode type were evaluated to define optimum conditions.

According to the obtained results; the most efficient combination was found as Al/Fe electrodes for removing COD and colour. The Optimum COD and colour removal were obtained as 66%, 98% respectively when reaction time was 10 minutes, cell current was 0.8 A and wastewater pH was 5.5. In experiments performed for electrode optimization, the increase in the time seemed to have no effect on removal efficiency. When we compared the results of 10th and 60th minutes, removal efficiencies were either stable or decreased. Meanwhile in the pH optimization studies, it has been determined that the best recovery

efficiency is at the original pH of the water. It has been found that the recovery efficiency increases as the current increases. Although the recovery efficiencies are close to each other, the cost is taken into consider and thus 0.8 A is used for optimization. The cost of treating 1 m^3 fruit juice wastewater is calculated as 2.69 US$.

When all these studies are examined, we have come to the conclusion that electrocoagulation can provide much more preliminary treatment than the final treatment of wastewater plants.

Nomenclature

A : Ampere
Al : Aluminium
COD : Chemical Oxygen Demand
EC : Electrocoagulation
Fe : Iron
St : Stainless Steel
TN : Total Nitrogen
TS : Total Solids
TSS : Total Suspended Solids
VS : Volatile Solids
VSS : Volatile Suspended Solids

References

1. Durán, A., J.M. Monteagudo, J. Gil, A.J. Expósito and I. San Martín, *Solar-photo-Fenton treatment of wastewater from the beverage industry: Intensification with ferrioxalate*. Chemical Engineering Journal, 2015. **270**: p. 612-620.
2. Al-Mutairi, N.Z., M.F. Hamoda, I. Al-Ghusain, *Coagulant selection and sludge conditioning in a slaughterhouse wastewater treatment plant.* Bioresour Technol., 2004. **96** (2): p. 115-119.
3. Ozbas, E. E., N., Tufekci, G., Yilmaz, S., Ovez, *Aerobic and anaerobic treatment of fruit juice industry effluents.* JSIR, 2006. **65**(10): p. 830-837.
4. Hala E., A., Tawfik, M., Mahmoud and H., Abdel-Halim, *Treatment of high strength wastewater from fruit juice industry using integrated anaerobic/aerobic system.* Desalination, 2010. **253**(1): p. 158-163.
5. Austermann-Haun, U., C. F. Seyfried, K., Rosenwinkel, *UASB-reactor in the fruit juice industry.* Water Science and Technology, 1997. **36**(6): p. 407-414.
6. Amor, C., M.S., Lucas, A.J., Pirra and J.A. Peres, *Treatment of concentrated fruit juice wastewater by the combination of biological and chemical processes.* Journal of Environmental Science and Health, 2012. **47**(12).
7. Ildikó Galambos, J.M., Molina, P., Járay, G., Vatai and E., Bekássy-Molnár, *High organic content industrial wastewater treatment by membrane filtration.* Desalination, 2004. **162**: p. 117-120.
8. González del Campo, A., F.J., Fernández, P., Cañizares, M.A., Rodrigo, F.J., Pinar, J., Lobato, *Energy recovery of biogas from juice wastewater through a short high temperature PEMFC stack.* International Journal of Hydrogen Energy, 2004. **39**(13): p 6937-6943.
9. Blöcher, C., T., Britz, H.D., Janke, H., Chmiel, *Biological treatment of wastewater from fruit juice production using a membrane bioreactor: parameters limiting membrane performance.* Water Science and Technology, 2003. **3**(5-6): p. 253-259.
10. Comninellis,C., G., Chen, *Electrochemistry for the Environment.* Springer, New York, NY, 2010.
11. Kuokkanen, V., U., Lassi, T., Kuokkanen, J., Rämö, *Recent Applications of Electrocoagulation in Treatment of Water and Wastewater*—A Review. Green and Sustainable Chemistry, 2013. **3**: p. 89-121.
12. Lin S. H. and M.L., Chen, *Treatment of Textile Wastewater by Chemical Methods for Reuse.* Water Res, 1997. **31**: p. 868.
13. Lin, S.H. and C. F., Peng, *Treatment of Textile Wastewaters by Electrochemical Method.* Water Res, 1994. **28**: p. 276.
14. Can O.T., M., Kobya, E., Demirbas, M. Bayramoglu, *Treatment of The Textile Wastewater by Combined Electrocoagulation*. Chemosphere, 2006. **62**(2): p. 181-187.
15. Vik E.A., D.A., Carlos, A.S., Eikum, E.T. Gjessing, *Electrocoagulation of potable water*. Water Res, 1984. **18**(11): p. 1355-1360.
16. Tsai C. T., S.T., Lin, Y.C., Shue, P.L., Su, *Electrolysis of Soluble Organic Matter in Leachate from Landfills.* Water Res, 1997. **31**(12): p. 3073-3081.
17. Mahesh S., B., Prasad, I.D., Mall, I.M., Mishra, *Electrochemical degradation of pulp and paper mill wastewater*, Part 2. Characterization and Analysis of Sludge. Ind. Eng. Chem. Res, 2006. **45**(16): p. 5766-5774.
18. Mahesh S., B., Prasad, I.D., Mall, I.M., Mishra, *Electrochemical degradation of pulp and paper mill wastewater.* Part 1. COD and Color Removal. Ind. Eng. Chem. Res., 2006. **45**(8): p. 2830-2839.
19. Song, P., Z., Yang, G., Zeng, X., Yang, H., Xu, L., Wang, R., Xu, W., Xiong, K., Ahmad, *Electrocoagulation treatment of arsenic in wastewaters: A comprehensive review.* Chemical Engineering Journal, 2017. **317**: p. 707-725.
20. John, S., P.A., Soloman, P.A. Fasnabi, Study on *Removal of Acetamiprid from Wastewater by Electrocoagulation.* Procedia Technology, 2016. **24**: p. 619-630.
21. Elabbas, S., N., Ouazzani, L., Mandi, F., Berrekhis, M., Perdicakis, S., Pontvianne, M-N., Pons, F., Lapicque, J-P., Leclerc, *Treatment of highly concentrated tannery wastewater using electrocoagulation: Influence of the quality of aluminium used for the electrode.* Journal of Hazardous Materials, 2016. **319**: p. 69-77.
22. Hernández-Francisco, E., J., Peral, L.M., Blanco-Jerez, *Removal of phenolic compounds from oil refinery wastewater by electrocoagulation and Fenton/photo-Fenton processes.* Journal of Water Process Engineering, 2017. **19**: p. 96-100.
23. Pouet M.F., A., Grasmick. *Urban wastewater treatment by electrocoagulation and flotation*. Water Sci. Technol, 1995. **31**(3): p. 275.
24. APHA (American Public Health Association), *Standard methods for the examination of water and wastewater*, 20th

ed., American Public Health Association, Washington, DC, 1998.

25. Kobya M., E. Demirbas, O.T. Can, M., Bayramoglu. *Treatment of levafix orange textile dye solution by electrocoagulation.* Journal of Hazardous Materials, 2006. **132**: p.183-188.
26. Can, O.T. *COD removal from fruit-juice production wastewater by electrooxidation electrocoagulation and electro-fenton processes*. Desalination and Water Treatment, 2014. **52**(1-3): p.65-73.
27. Sengil, I.A., S. Kulac, M., Ozacar, *Treatment of tannery liming drum wastewater by electrocoagulation*, Journal of Hazardous Materials, 2009. **167**:p.940-946.
28. Holt, P.K., G.W., Barton, M. Wark, A.A., Mitchell, *A quantitative comparison between chemical dosing and electrocoagulation.* Colloid Surface,2002. **211**: p. 233-248.

Available online at www.dergipark.gov.tr

INTERNATIONAL ADVANCED RESEARCHES
and
ENGINEERING JOURNAL

Journal homepage: www.dergipark.gov.tr/iarej

e-ISSN: 2618-575X

International
Open Access

Volume 02
Issue 01

April, 2018

Review Article

Investigation of usage potentials of global energy systems

Saban Bulbul [a,*], ***Gorkem Ertugrul*** [b], ***Fatih Arli*** [c]

[a]*Necmettin Erbakan University, Seydişehir Ahmet Cengiz Engineering Faculty, Konya, 42370, Turkey*
[b]*Dumlupınar University, Engineering Faculty, Kütahya, 43100, Turkey.*
[c]*Yıldırım Beyazıt University, Graduate School of Natural Sciences, Ankara, 06010, Turkey.*

ARTICLE INFO

Article history:
Received 24 February 2018
Revised 20 March 2018
Accepted 21 March 2018

Keywords:
Energy demand
Energy systems
Fossil energy
Renewable energy

ABSTRACT

Throughout history, mankind has made progress in social and technical areas by finding many energy sources and developing energy systems. For this reason, energy is a necessary and indispensable issue. Today, due to the increasing demands, the energy requirement has increased even more than in the past. In order to increase this energy capacity, researches and studies have been carried out on the use of energy systems more efficiently. They will be also carried out in the future. In the new global world, great progress has been made in the energy systems technology and very different systems have been found. It is clear that these systems provide high benefits in many sectors, especially in the industrial and transportation sectors. In order to use the energy for their internal consumption, and also export it, the developed countries have power plants with large production capacity. For this reason, the developed countries are competing with each other in energy issues. Producing mechanical and electrical energy, using underground energy sources and alternative energy sources are the major factor which keeping pace with the changing world. In this study, it has been tried to give technical and statistical information about the use of natural energy, natural gas, coal and nuclear energy sources and renewable energy systems such as wind, solar, hydro and biomass. We emphasized which energy system the world head toward for certain years. In addition, the advantages and disadvantages of these systems have been demonstrated.

1. Introduction

Energy experts say that very soon, the major emphasis will be on the running out of fuel resources in the world. Petroleum, coal and natural gas have been taken out from the earth for million years. It is estimated that petroleum will be used up within 100 years and coal will run out approximately within 500 years. Ignoring the minor issues, today's researchers examine the future supply-demand changes related to energy systems in detail. (Debates and polemics about energy do not affect) The mechanical power is arisen from our energy reserves. The world loses its energy capital, and this situation does not raise enough concern in the society [1].

Planning energy systems depends on economical, environmental, constraints, and other factors. These factors are important challenge around the world. Natural energy resources are not infinitive and nowadays many countries need a lot of energy. To get expressive and much more energy, many experts have found new energy systems and developed new energy policies [2]. In the economic system of global energy market, first and last suppliers chain includes countries and companies generating energy and also countries and companies consuming it. Fiscal and income surveys are important for intermediate production and final consumption. In addition, these surveys are interdependent with certain agreements in using of the direct and indirect energy that involved in commercial activities in the economic system [3]. Depending on the energy system, the technology and the energy source, the economic factors of energy production vary. Energy resources have certain characteristics. There are definite statistical distributions. Depending on wells, minefields, river beds and mountains areas etc., these distributions may change.

* Corresponding author. Tel.: *+90-332-582-6000*; Fax: *+90-332-582-0450.*
E-mail address: *sabanbulbul42@hotmail.com*

Because of this change, productivity and economic factors are modified. Assessment of energy is elaborated for all (country and industrial) economies. [4, 5].

Environmental policies direct the designing of energy systems. For example, the global warming and climate changing are two of the most important environmental problems. They usually result because of the greenhouse gas (GHG). GHG is the most important factor affecting the amount of energy generation from different energy systems. According to the research conducted in the last two decades, energy production from the fossil sources has had negative impact on the environment. However, it can be thought that this issue may open the way for policies leading clean energy production. Energy experts emphasize that new technologies should be developed to fix the negative impacts of climate change, GHG and carbon emissions on the energy economy. Some researchers say that new energy presentation programs need to be developed for clean and efficient energy planning [6, 7].

Energy organizations and investors ought to get new or improved energy systems for efficient energy and in order to decrease environmental problems. In these studies, a new global energy system management may be found out. By using qualitative performance of the energy system, quantitative and qualitative assessments on the demand and production values can be achieved. In order to investigate structure of global energy systems, regional activities (economic and technical) and investment affair can be analyzed. They have key roles. Rebound effect can be thought in energy system issues. It can cause increasing of energy efficiency and diminishing GHG. So that, by using energy, the economic growth can be enhanced [8, 9, 10].

The usage policies of energy systems lead to global energy scenarios. Most of these scenarios include focusing on renewable energy (RE). But, scope of energy sanctions is not definite and based on investigation in the present research. In addition, many energy scenarios usually do not reflect the real current demand and production values because economic factors and the amount of the demand change over the time [11, 12]. This situation relies on development of the world.

Energy is used by different economic entities in global supply chains, including the exploiter, producer, consumer, intermediate trader and final trader. The chains of energy systems can be evaluated by many factors. The systems of input-output analysis method is adopted to trace the direct and indirect energy use associated with both intermediate production and final consumption activities in the economic system. In the world economy, 15% of the energy use embodied in trade turns out to be induced by final consumption, and 85% is attributed to intermediate production [3].

Global energy expenditure has been swiftly increased in last 50 years, and it will be going on to expand over the next half century. Using of fossil fuels stimulated the increasing of industrialization in North America, Europe and Japan for cheap energy in the past. In addition to these countries, energy consumptions of the other countries also continue to increase. Thus, this consumption is going to effect the industrialization and energy planning of next 50 years. Technologies of China and India have improved rapidly due to the energy usage because they represent approximately a third of the world's human population. The depletion of oil resources in the near future is an expected situation. The advantage factors of the RE technologies of wind biofuels, solar thermal, and photovoltaics (PV) have finally showed maturity and the ultimate promise of cost competitiveness [1].

According to International Energy Agency (IEA), total primary energy usage in North America and Europe has come down, and the increase in the global average energy use has arisen about 2.8 % during the last decades [13,14,15,16].

Even, with a 2% increase in energy usage per year, the primary energy demand of 12,271 MTOE in 2008 would double by 2043 and triple by 2063. Of course, the global energy usage cannot continue to increase at the same rate forever. It is estimated that the global energy usage will increase at an average annual rate of 1.2 until 2035. It may be even optimistically estimated that the growth rate will be 1.2 %. Reaching a value of 16.934 MTOE/year, the global energy usage will increase by 38% until 2035 [13, 16]. World energy demand values are shown in Figure 1 and Table 1.

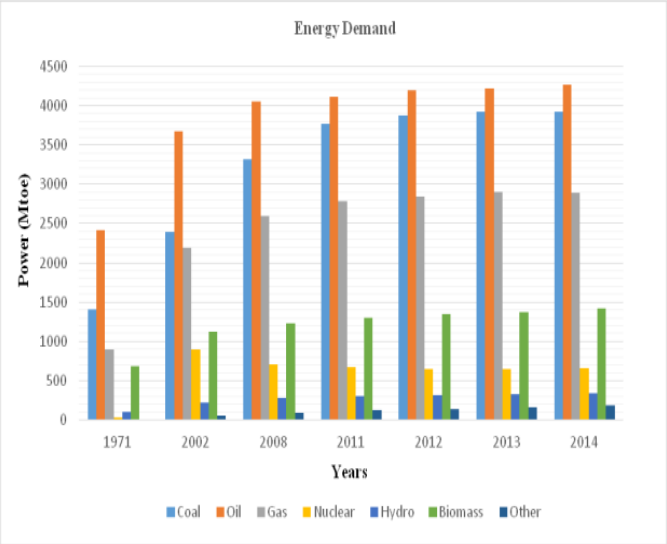

Figure1. Changing in world energy demand for the last decades [17, 18, 19, 13, 14, 15, 16]

Table 1. Energy demand of the last decades in the world [17, 18, 19, 13, 14, 15, 16]

Energy Production (Mtoe)							
Year	Coal	Oil	Gas	Nuclear	Hydro	Bio	Other
1971	1407	2413	892	29	104	687	4
2002	2389	3676	2190	892	224	1119	55
2008	3315	4059	2596	712	276	1225	89
2011	3773	4108	2787	674	300	1300	127
2012	3879	4194	2844	642	316	1344	142
2013	3929	4219	2901	646	326	1376	161
2014	3926	4266	2893	662	335	1421	181

In this paper, the production quantities of the world's energy systems over the years and the change in demand figures have been shown. In recent years, it has been attempted to explain to which energy systems the world give importance and why. They have been given up step by step. Energy production and demand distributions within the last ten years in major energy production regions around the world were examined in comparison with the numerical values for each energy system, and the energy systems selected by these regions.

2. Global Energy Resource

In order to meet the basic energy demands perfectly in next 40 years, besides identifying the targets, perfectly use of traditional energy sources (such as fossil and uranium) is also important. The restriction fixed them for the reasons of environmental policies [1].

2.1 Natural Gas Energy

Natural gas is a one of the fossil energy resource that can be found in nature reserves. Although it occurs in a similar way with oil, it differs from oil. This energy resource is supposed to play an important role in the progression of a cleaner and more flexible fossil energy system [20]. Natural gas chemical composition is a mixture of light hydrocarbons, generally alkanes, which are normally gaseous at room temperature. It is the cleanest and the least carbon-intensive natural energy resource. Methane (CH_4) is the most abundant gas, accounting for more than 85% of the natural gas. In addition to the other components of natural gas, they are light alkanes and hydrocarbon compounds such as ethane, propane, butane and others. Natural gas attracts the interest of many area (such as energy and environment). It contains a lot of methane that has been considered as an input in the production of other high value products (such as syngas and high purity hydrogen). Considering the environmental protection trend in the world, the usage of naturel gas is emphasized as a clean and sustainable energy generation. So, it can be said that the interest of researchers on natural gas will increase importantly in near future [21, 20]. In the last about 20 years, GHG emissions have been rising continuously. These emissions value have been steady about 32 billion tons of carbon dioxide (CO_2) equivalent and resulted due to fuel combustion ($GtCO_2$-eq) since 2014. Because combination of mix natural gas and renewable energy intensity and changing are low ratio, separate energy generation should be assessed. Decreasing in energy intensity equaling to 77 % of the impact on world emissions has been caused by global domestic product improvements since 2014. And, remaining ratio (23 %) is offset by changing fuel mix. As it can be understood from this, energy efficiency has a key role for steadying and reducing emissions [22]. For these reasons, not only positive environmental impact of natural gas has been considered but also the annual production of natural gas has been increased in some regions (Table 2).

Table 2. World natural gas production [17, 18, 19, 13, 14, 15, 16]

Some Years of Energy Production (BCM)							
Region	2000	2002	2008	2011	2012	2013	2014
North America	788	759	815	869	901	924	941
Europa	482	491	555	525	507	512	462
Asia Oceania	122	130	170	202	218	221	221
Eurasia	609	635	701	703	692	691	657
Asia	136	209	341	410	433	461	484
Middle East	201	219	335	399	404	420	441
Africa	53	69	100	111	120	119	131
Latin America	105	102	131	149	156	159	165
World	2527	2622	3149	3370	3432	3507	3502

2.2 Coal Energy

The usage of the coal utilized as a heating fuel for thousands of years has been increased after invention of steam machines in the 19th century. Even though environmental policies have been adopted in the energy sector today, it has become an indispensable energy source in many countries. Coal is one of the solid natural energy resource which is kind of fossil fuels. It has variety organic (Carbon) and inorganic (such as hydrogen and oxygen) materials in its structure [23, 24]. During geological ages, coal was formed like sedimentary rocks. And, quality of the coal was determined by geological activities, different chemical reactions and environmental conditions during those ages. In other words, these factors are very important for the heat generation capacity (energy) of coal [25, 23, 26]. Regarding these factors, two different kinds of coals emerge underground. First hard coal (Anthracite and Bituminous) which has high calorific value. Second, Brown coal (Sub-bituminous coal and Lignite) that has lower calorific value than hard coal [26].

Coal is the most controversial fuel for good reasons. On the one hand, it provides almost 30% of global primary energy, and it is the world's most popular fuel for generating electricity, producing steel and making cement. It is also relatively affordable and widely available. On the other hand, coal use is responsible for 45 % of energy-related CO_2 emissions, as well as over 40 % of SO_2, around 15% of NO_x and emissions of fine particulate matter. As a result, analysis on coal too often tends to be one sided; highlighting either the negative environmental consequences or its positive contributions to economic growth. It is critical that in order to understand the

important role that coal plays in the global energy system, we should examine both sides of the coin. That is, while we are thinking about the implications of climate policies on the future of coal, we should also take in to account what coal is doing and will continue to do for energy security, economic growth and energy access in developing and emerging economies. In recent years, coal has been seen as a dying industry as a result of a greater awareness about climate change as well as growing competition of other energy sources like natural gas or renewables. In the last few years, global coal demand has stalled. However, there was a notable change showing a 4% annual growth from 2000 to 2013. Therefore, it is too early to say that coal is dead. Sluggish economic growth and energy efficiency improvements are restraining the power demand around the world [27].

Combined with the deployment of wind and solar photovoltaic (PV), these global forces squeezes conventional generation -- including coal. At the same time, carbon prices and other policies make the gas increasingly attractive, particularly in the United States. In this environment defined by the United States and Western Europe, new coal power plants are rare and the existing fleet steadily disappear. But there is another picture to consider, that of emerging economies with growing populations and prospects of robust economic growth. Some of them are dealing with frequent blackouts. Others are unable to provide electric power for everyone. For these countries, (most of them are in South and Southeast Asia) coal can provide affordable and secure electricity. For instance, although more than one quarter of the world's population are living in India, Indonesia, Pakistan and Bangladesh, , they have only 7 % of total global electric usage, and a large part of their population have no access to electricity. These four countries possess significant coal reserves. New coal power generation capacity could lock-in large amount of CO_2 emissions for the next decades. Yet it could also help in bringing modern energy services to millions of people. This is the contradiction of coal. And this is why we need to find ways to make the use of coal more environmentally sustainable by ensuring that all countries decide to use coal-fired power plants only to build the latest ultra-supercritical technologies and plan for carbon capture and storage in the future [27]. Coal burning processes can cause various environmental problems. For instance, as a result of coal burning, GHG occurs. SO_x in the burning coal gas reacts with water vapor in order to form acid rain [28]. Combustion of coal causes air pollutant particulate matter. Because of these environmental problems, many developed countries, such as England and France, have given up energy generated from coal. Because accepted environmental considering is formed by many countries, nowadays coal production and energy generation from coal are gradually diminished in comparison to the past years in the world (Table 3).

2.3 Geothermal Energy

Geothermal energy can be defined as boiling water stored underground in rocks and RE resource. It is a sustainable source of energy generation. Geothermal energy has been used for heating, cooking, bathing and other works for a long time in human history [29, 30]. First of all, geothermal was used for energy generation in 1904. And, this year was managed to start new geothermal energy epoch in the Lardarello area in Tuscany [31, 30]. Hence, geothermal energy took place in energy market.

Table 3. World coal production [17, 18, 19 13, 14 15, 16]

Some Years of Energy Production							
Region	2000 (Mtoe)	2002 (Mt)	2008 (Mtce)	2011 (Mtce)	2012 (Mtce)	2013 (Mtce)	2014 (Mtce)
North America	579	1051	883	826	767	745	757
Europa	319	822	258	248	246	294	225
Asia Oceania	184	364	337	323	348	382	412
Eurasia	213	469	401	429	461	435	423
Asia	1153	1864	2717	3377	3538	3623	3549
Middle East	7	15	2	1	1	1	1
Africa	91	174	208	209	218	218	224
Latin America	23	30	79	85	88	85	88
World	2355	4791	4880	5497	5667	5723	5680

Very hot flow resources of geothermal energy occur as mantle and core activities in the earth. These flows are taken upward and outward from deep subsurface. They may contain radioactive materials (uranium and thorium etc.). But when precautions are taken, they are harmless for the environment. Geothermal energy systems cannot be affected by weather and climate. Principle of geothermal energy is independent from sun and other conditions [32, 1]. Heat, permeability and water content features of geothermal resource are important factors in order to establish geothermal power plants generating energy by using geothermal systems. The most important of these properties is heat value. For the commercial energy generation purposes, heat value must be at least about 149 ^oC (300 ^oF). While the temperature increases, energy generation also increases. [1]. Energy generation may be significant for investors if geothermal resource heat is above 300 ^oC. Yet, Energy generation may be insignificant for investors if geothermal resource heat is below 150 ^oC. Reason of this is that energy generation (kW/h) increases in direct proportion to the increase in temperature [1, 33]. Whole Earth geothermal resource provides 50000 times more energy than all oil and gas resource do, and geothermal energy systems will increasingly continue to develop [34, 35]. Energy generation from geothermal systems has many benefits. For example, it contributes to reducing the impact of global warming, stopping GHG releasing to atmosphere, decreasing the public health risks and getting energy independently from fossil energy resources [36, 37]. RE technologies can ideally provide energy demand without any problems. But, sometimes energy investors see many barriers and risks discouraging them to get into the sector. Governments of countries had better ensure a positive policy and regulatory environment for research, development and innovation, and they should provide activities needed to support the sector (installers, service companies, etc.). Successfully policy development

provides not only the ability to assess which technologies have an important potential for the demanded energy, but also economic, sustainable energy and non-pollution. [19, 38, 32, 37, 39].

Nowadays, geothermal power technology has been continuing to improve; in 2015, its energy generation capacity reached to 12.7 gigawatts (GW) and the generated electric was 80.9 terawatt-hours (TWh) all over the world. Costs of energy generated by geothermal power plants vary between 1870 USD and 5050 USD per kilowatt. Likewise, costs of electric generation in geothermal power plant vary between 0.04 USD to 0.14 USD per kilowatt-hour. This situations contribute to benefits for economic issues [40]. Electric generation from geothermal power is shown in Table 4.

Table 4. World geothermal energy exploiting [18, 19, 13, 14, 15, 16]

Consumptions Value	
Years	Electricity generation (TWh)
1990	36
2002	57
2008	65
2011	69
2012	70
2013	72
2014	77

2.4 Oil Energy

Oil is a fossil energy resource which has been used since engine technology was invented in 19th century. Due to the development of engine technology and the advanced industrial activities (such as motor vehicle industry), importance of oil energy has boomed around the world. Depending on industrialization conditions, global oil companies have established and they have started to manage most of the energy market. Then, Complex oil transport systems have been established around the world for oil energy supply and oil companies and petroleum producing countries have gotten a great advantage for their economies [41]. Therefore, oil has taken part in the modern world. Oil has an important role in the modern world economy. It constitutes greatest energy trades of world. Approximately 33% of the world transportations depends on oil. Oil mainly provides cheap transportation goods and logistic to our world economies [41]. Oil demands have boomed three times in history. First, there was a great demand between 1859 and 1911; that period was called as Kerosene Era. Rapid industrialization and the need for raw materials caused an increase in demand in this period. Second period was named OPEC (Texas) Era (1973-2008). OPEC was established in 1960. And, the oil market grew more in this era. The global oil companies in central Texas wanted to erode price stability. In order to keep prices stable at high levels, oil regulators and global oil companies realized oil quotas, oil pooling arrangements, oil price formulas and market share agreements. Last era is called Bust Era (2009-). When OPEC members met in September 2008, they stated that the price of crude oil was dropped from $ 147 to $ 106 per barrel. But it has been never fulfilled. This incident caused disagreements among many OPEC members [42]. Primarily oil, coal and natural gas have been kept going as main energy resources. When fossil energy sources are compared to RE sources and nuclear energy resources, energy experts estimate that they will provide about 50 % of world energy source. Because of non-combusted transportation, oil demand rates have decreased step by step (Table 5). Yet, World oil demand continues to increase. And, world oil demand rating is not seen to be decline in the next years. [43, 16, 15, 14, 44, 45, 46, 47].

Oil energy has notable debate and disagreement on the estimates of ultimate recoverable. In addition, it is appeared as a good compromise on the amount of oil reserves in the world energy sector. However, concerns on the issues, such as GHG, global warming, climate change, air quality, and other environmental factors, affects the demand and generation of oil negatively. Some expert said that environmental changing (climate, air and water) will be inevitable in the future. But, eco-friendly activities have been made (production electrical cars, hybrid energy systems development and trending green energy-such as solar and wind systems- etc.). These activities are partially successful. The exploiting of oil will have been continued about the next two decades [43, 41, 48, 49, 42, 50, 51].

Table 5. World oil energy source demand (mb/d) [52, 19, 14, 15, 16]

Region	1990	2000	2013	2014	2015
North America	19.4	23.1	21.9	21.9	21.8
Europa	12.6	13.9	12.7	12	11.5
Asia Oceania	6.9	8.0	7.0	7.7	7.3
Eurasia	9.3	4.1	4.6	4.9	4.9
Asia	6.3	11.4	16.3	19.7	20.8
Middle East	2.8	4.3	6.5	7.6	7.6
Africa	1.9	2.2	3.0	3.6	3.7
Latin America	3.1	4.2	5.3	5.7	5.9
World	66.1	76.7	84.0	90.1	90.6

2.5 Nuclear Energy

New energy era has been launched for nuclear energy systems due to arising the GHG emissions from the use of fossil energy systems, sustainable energy planning and the concern about the reduction of fossil energy resources [53, 54, 55]. Nuclear energy, which was first noticed in the 1930s and 1940s, is a sustainable system. In those times, it was demonstrated that a large amount of energy could be obtained from a little material. Energy emerges from the nuclear energy materials as a result of fission and fusion reactions. These reactions are endless in the atom. So, limited energy resources are not problem. Nuclear energy systems are based on atomic fusion process due to more available enormous energy [56, 57]. Nuclear energy policies contribute to economic growth and reducing the dependency to the foreign countries energy resources [58].

Nuclear energy has a major role in decreasing GHG emissions in energy sector. Resource investment and energy marginal production costs of nuclear energy systems are lower than other energy systems (natural gas and oil etc.). In addition, structure of nuclear energy cost is also stable. But Nuclear power plant investment cost is high. [54, 59, 60]. Nuclear energy systems may carry out some risks on environmental and public health. Almost all of the environment experts suggested that the possibility of a nuclear leak is high as a result of occurrence of an accident danger and malfunction or nuclear disaster under certain situations of production energy. Then, some amounts of radioactivity materials (Airborne radioactivity particle) and harmful radiation rays can release the environmental and public area. They may be carried by air movements far away. And then, they can cause a variety of chronic diseases on humans and devastation for nature [61, 56, 62]. Nuclear energy policies was greatly affected in 2011. The TEPCO Fukushima Daiichi nuclear power plant experienced a huge nuclear accident in March 2011. This accident was elaborated. Then, this event caused to modification of nuclear energy policies almost all over the world. [53, 54]. The idea of continuing electricity generation from green fossil energy was put forward. U.S.A. launched new nuclear programs which are safer and measured cautious. Germany shut down some nuclear plants and others brought new plan. As a result, electric/power generation from nuclear energy systems has been significantly changed after 2011. (Table 6) [63, 56].

Table 6. World nuclear energy demand [17, 18, 64, 65, 66, 19, 13, 14, 15, 16]

Years	Energy Demand Value (Mtoe)
1971	29
1990	526
2000	674
2002	692
2004	714
2007	709
2008	712
2011	674
2012	642
2013	646
2014	662

2.6 Hydro Power Energy

Hydro Power is a RE system in which, energy generation is done by movement of water. To reduce GHG in the atmosphere and to provide green energy, this energy system has been used like other RE systems. Although quality and quantity of hydro energy systems are directly affected by climate change-conditions and rely on water flow, hydro energy systems will have been drastic energy systems [67, 68, 69].

Hydro energy systems presents some advantages such as high reliability, proven technology, high efficiency, flexibility, large storage capacity, very low operating and maintenance costs [70]. Because of these advantages, these energy systems has widespread worldwide and the usage of it has continued to increase in the global energy market recent years (Table 7). About 16 % of generated electric energy is gotten from hydro energy systems. Some countries produce a large part of their electricity energy needs through hydro power energy systems. For example, 99 % of electric energy of Norway, 84 % of electric energy of Brazil and 58 % of electric energy of Canada are obtained from hydro energy systems [71].

Table 7. World hydro power energy demand [17, 18, 64, 65, 66, 19, 13, 14, 15, 16]

Years	Energy Demand Value (Mtoe)
1971	104
1990	184
2000	228
2002	224
2004	242
2007	265
2008	276
2011	300
2012	316
2013	326
2014	335

2.7 Wind Power Energy

Wind power system first started in the early 1900s in North America. This early system was important in farms for supplying required electric during works. [72]. After World War II, improvement of wind energy systems occurred due to research and developments focusing on wind energy systems in most of Europa. Therefore, wind energy has taken part in RE worldwide [73]. The global warming is a big environmental problem for the whole world. In the 21st century, global temperature has increased approximately 2 ^{o}C. It is thought that the main reason of this is greenhouse gasses (GHG) originating from fossil energy systems. [74, 75]. In order to manage environmental costs, global use of a RE systems having technical, economical and environmental advantages must become widespread. This can be achieved by using wind energy systems. Many countries aim to improve wind energy systems so that it will became a main energy system in 2050. Thus, wind energy systems will be a significant key in energy planning in the future [75, 76]. As a result of developing society and advanced technology, energy demand topics have gained importance in new strategic planning. Many countries trends to focus on new green energy systems. Wind energy system is one of these new green energy systems. Whereas wind energy carries out environmental noise, relying on wind features (wind speed continuity optimum-wind speed 10 m/s, number of blows), it may also cause possible fatalities of birds, bats, and etc. Especially it is preferred by developed countries. In these

countries, using of wind systems has increased in the last years (Table 8) because it is non-polluting, does not have negative effect on global warming and is widely used in many regions. [77, 78, 79, 80, 73].

Table 8. World wind power energy demand [17, 18, 64, 65, 66, 19, 13, 14, 15, 16]

Years	Energy Demand Value (TWh)
1990	4
2000	31
2002	48
2004	77
2007	173
2008	219
2011	434
2012	521
2013	635
2014	717

2.8 Solar Energy

Buildings and other structures require eco-friendly, low cost and sustainable energy systems for heating, cooling and other needs requiring electricity. It is determined that the most suitable of these energy systems is solar energy system. Sun rays supplies almost all of the world's energy and the energy of the sun rays in a year is more than other systems (fossil and wind etc.) have. Sun is the most powerful energy resource for world. It can be called as an infinite energy source [81, 82, 83]. A first solar cell was invented in 1954. That was made of silicon. It was a turning point for solar energy systems [84]. Solar energy system has gained importance step by step because of the increase in electricity energy prices, national policy factors and fluctuations in oil prices. Although solar energy systems are installed in nature, cities and towns, its installation cost is high. However, depending on daylight, it energy costs have declined significantly compared with many other energy systems [85, 86, 87]. There are large-scale installed solar power systems in about 60 countries. And this number is estimated to increase in other countries. [88, 89, 90]. Using of solar energy systems continue to rise worldwide (Table 9).

Table 9. World solar energy demand [65, 66, 19, 13, 14, 15, 16]

Years	Energy Demand Value (TWh)
1990	0
2004	2
2007	5
2008	12
2011	61
2012	97
2013	139
2014	190

2.9 Biomass Energy

Once, biomass was one of the major energy resources like sunshine worldwide. During the industrial revolution, coal and oil were very necessary energy resource. Then, due to sustainable energy policies and other reasons (economical and environmental etc.), new energy systems have become as interest area. One of these new energy systems is nuclear. Due to emerging the Three Mile Island incident In U.S., nuclear energy have begun to look objectionable. Then, energy policies have focused on RE systems. After many debates about energy, removing the carbon tax from energy companies producing fossil energy was accepted. Hence, this issue has been a milestone for the use of biomass energy systems [91].

Biomass energy is supplied from organic materials which remain (decomposing and organic waste) from animals or plants, and then, biomass energy resource occur. [92, 93]. Bio materials (crop, herbaceous, woody, and waste materials etc.) that are the source of the biomass energy system are much more beneficial than fossil energy resources. It is one of the primary, domestic, clean and inexhaustible energy systems. It has a unique structure different from coal and oil. Biomass energy combustion systems are non-polluting and they contribute to protection of the environment and have increased world demand (Table 10) [94, 95, 93]. But they can cause dust pollution [96].

Table 10. World biomass energy demand [65, 66, 19, 13, 14, 15, 16]

Years	Energy Demand Value (Mtoe)
1990	905
2004	1176
2007	1176
2008	1225
2011	1300
2012	1344
2013	1376
2014	1421

3. Conclusions

The energy sector is significantly influenced by political, economical, social and environmental factors. Such as global warming, air pollutions, fluctuations of energy prices (especially in oil), global economic sector (energy bourse), national economic and energy resource situations, international and national industrial and eco-friendly policies, social planning stemming from emerge power plant accident (nuclear energy), and other issues relying on some energy system (oil, natural gas and coal) lead the global energy systems.

Although oil is considered as the most harmful energy source to environment (air, water and climate etc.), due to all types of transport systems requiring nearly half of the energy consumed in the world and the dependence of

industries and activities of developing countries, global oil market demand rates have continued to increase for a long time. It is also estimated that it will continue to increase about next two decades. But the situation in nuclear energy is very different. Nuclear accident, radioactive leaks, nuclear danger and risk factors have directly affected generation of energy from nuclear systems.

RE (wind, solar, geothermal, hydro, biomass, etc.) are attractive systems because of their sustainability, non-polluting features and lower cost. Most of countries encourage energy investors to install renewable systems. For this reason, RE demand values continue to grow in large quantities.

Coal energy used for thousands of years is an indispensable system for some countries although some other countries have given it up due to some reasons such as GHG emissions of coal mining which is harmful to workers. Needed energy from coal has been changing for years.

In conclusions, Energy systems are important issue worldwide. No country and corporations can exist without energy. Whatever the obstacles to energy systems are, for development, they will leave their place to someone else which fills their time.

Nomenclature

Mtoe : Million ton oil equivalent
BCM : Billion cubic meters
Mtce : Metric tons carbon equivalent
Mt : Megatons
TWh : Terawatt Hour

References

1. Goswami, D. Y., & Kreith, F. (Eds.). Energy efficiency and renewable energy handbook. 2016, USA: CRC Press.
2. M. A. Rosen, *Assessing global resource utilization efficiency in the industrial sector*. Science of the Total Environment, 2013. 461-462: p. 804-807.
3. X. F. Wu and G. Q. Chen, *Global primary energy use associated with production, consumption and international trade.* Energy Policy, 2017. 111: p. 85-94.
4. J. F. Mercure and P. Salas, *An assessment of global energy resource economic potentials*. Energy, 2012. 46(1): p. 322-336.
5. Chen, B., Li, J. S., Wu, X. F., Han, M. Y., Zeng, L., Li, Z., and Chen, G. Q., *Global energy flows embodied in international trade: A combination of environmentally extended input–output analysis and complex network analysis.* Applied Energy, 2018. 210: p. 98-107.
6. Rahman, S. M., and Miah, M. D., *The impact of sources of energy production on globalization: Evidence from panel data analysis*. Renewable and Sustainable Energy Reviews, 2017. 74: p. 110-115.
7. Nowotny, J., Dodson, J., Fiechter, S., Gür, T. M., Kennedy, B., Macyk, W., and Rahman, K. A., *Towards global sustainability: Education on environmentally clean energy technologies*. Renewable and Sustainable Energy Reviews, 2018. 88: p. 2541-2551.
8. Finnerty, N., Sterling, R., Coakley, D., Contreras, S., Coffey, R., and Keane, M. M. , *Development of a Global Energy Management System for non-energy intensive multi-site industrial organisations: A methodology*. Energy, 2017. 136: p. 16-31.
9. Li, H., An, H., Fang, W., Wang, Y., Zhong, W., and Yan, L., *Global Energy Investment Structure Based on the Shareholding Relations of Global Listed Energy Companies*. Energy Procedia, 2016. 88: p. 230-235.
10. Wei, T. and Liu, Y. , *Estimation of global rebound effect caused by energy efficiency improvement*. Energy Economics, 2017. 66: p. 22-34.
11. Koskinen, O. and Breyer, C. , *Energy storage in global and transcontinental energy scenarios: a critical review*. Energy Procedia, 2016. 99: p. 53-63.
12. Fischhendler, I., Herman, L., and Maoz, N. , *The political economy of energy sanctions: Insights from a global outlook 1938–2017*. Energy Research & Social Science, 2017. 34: p. 62-71.
13. WEO, I. International Energy Agency. *World Energy Outlook 2013*. 2013, France: International Energy Agency.
14. WEO, I. International Energy Agency. *World Energy Outlook 2014*. 2014, France: International Energy Agency.
15. WEO, I. International Energy Agency. *World Energy Outlook 2015*. 2015, France: International Energy Agency.
16. WEO, I. International Energy Agency. *World Energy Outlook 2016*. 2016, France: International Energy Agency.
17. WEO, I. International Energy Agency. *World Energy Outlook 2002*. 2002, France: International Energy Agency.
18. WEO, I. International Energy Agency. *World Energy Outlook 2004*. 2004, France: International Energy Agency.
19. WEO, I. International Energy Agency. *World Energy Outlook 2010*. 2010, France: International Energy Agency.
20. International Energy Agency. *Global Gas Security Review (GGSR) 2017*. 2017, France: International Energy Agency.
21. Mokhatab, S. and Poe, W. A. *Handbook of natural gas transmission and processing.* 2015, USA: Gulf professional publishing 3rd Edition
22. International Energy Agency. *Energy Efficiency (EE), 2017*. 2017, France: International Energy Agency.
23. International Energy Agency, *Coal Information (CI) 2014*. 2014, France: International Energy Agency.
24. International Energy Agency, *Coal Information (CI) 2017* 2017, France: International Energy Agency.
25. Miller, B. G. *Coal Energy Systems*. 2005, USA: Elsevier.
26. Mazumder, B. *Coal science and engineering*. 2012, India: Woodhead Publishing India Pvt Limited.
27. International Energy Agency. Coal Medium-Term Market Report Market Analysis and Forecasts to 2021, 2016, France: International Energy Agency.
28. Parks, P. J. *Coal Power: Energy and the Environment (Compact Research Series)*. 2011, Reference Point Press.
29. Cataldi R., Hodgson S. and Lund J. (Eds.). *Stories from a Heated Earth – Our Geothermal Heritage*, 1999 USA: Geothermal Resources Council and International Geothermal Association.
30. Fridleifsson I. *Geothermal energy for the benefit of the people.* Renew. Sustain Energy Rev. 2001. 5: p. 299–312.
31. DiPippo R. *Geothermal power plants: evolution and*

performance assessments. Geothermics 2015. 53: p. 291-307.

32. Eisentraut, A. and Brown, A. (2014). Heating without global warming–market developments and policy considerations for renewable heat. International Energy Agency, Paris Cedex, France.
33. Twidell, J., and Weir, T. *Renewable energy resources*. 2015, USA: Routledge.
34. 1. Shere, J. (2013). Renewable: The World-Changing Power of Alternative Energy. St Martin's Press: New York.
35. Sigfusson, B., Uihlein, A. (2015). *2015 JRC Geothermal Energy Status Report.* 2015, International Energy Agency.
36. International Renewable Energy Agency (IRENA). *Geothermal Power: Technology Brief*. 2017, Abu Dhabi: IRENA.
37. International Energy Agency. *Technology Roadmap Geothermal Heat and Power*. 2011, France: IEA.
38. International Energy Agency. *Renewable Energy Essentials: Geothermal (November 2010)*. 2010, France: IEA.
39. World Energy Council. *World Energy Resources Geothermal*. 2016.
40. International Renewable Energy Agency (IRENA). *Renewable Cost Database*. 2017, Abu Dhabi: IRENA.
41. Bentley, R. W. *Introduction to peak oil (Vol. 34)*. 2016, Switzerland: Springer.
42. McNally, R. Crude Volatility: *The History and the Future of Boom-Bust Oil Prices*. 2017, USA: Columbia University Press.
43. BP. BP Energy Outlook 2017 edition. 2017, UK: BP.
44. International Energy Agency. *Oil Information 2013*. 2013, France IEA.
45. International Energy Agency. *Oil Information 2014*. 2014, France IEA.
46. International Energy Agency. *Oil Information 2015*. 2015, France IEA.
47. International Energy Agency. *Oil Information 2016*. 2016, France IEA.
48. Lacalle, D. and Parrilla, D. *The Energy World is Flat: Opportunities from the End of Peak Oil*. 2015, USA: John Wiley & Sons.
49. Palmer, H. *Oil, Gas and Energy Financing*. 2011, UK: Euromoney Institutional Investor PLC .
50. Rapier, R. *Power Plays: Energy Options in the Age of Peak Oil*. 2012, UK: Apress.
51. Carmalt, S. W. *The Economics of Oil: A Primer Including Geology, Energy, Economics, Politics*. 2017, Switzerland: Springer.
52. WEO, I. International Energy Agency. *World Energy Outlook 2009*. 2009, France: International Energy Agency.
53. Alonso, A., Nakoski, J., Lamarre, G., Vasquez-Maignan, X., Dale, B., Keppler, J., & Gannon-Picot, C. (2012). Nuclear Energy Today, Nuclear Energy Agency
54. Houssin, D., Dujardin, T., Cameron, R., Tam, C., Paillere, H., Baroni, M., ... & Herzog, A. (2015). Technology Road-map-Nuclear Energy (No. NEA-IEA--2015). Organisation for Economic Co-Operation and Development.
55. Eerkens, J. W. *The Nuclear Imperative: A Critical Look at the Approaching Energy Crisis Second Edition*. 2010, USA: Springer.
56. Murray, R., and Holbert, K. E. *Nuclear Energy: An Introduction To The Concepts, Systems, And Applications Of Nuclear Processes*. 2015, USA: Elsevier.
57. Bodansky, D. *Nuclear energy: principles, practices, and prospects Second Edition*. 2007, USA: Springer.
58. Ben Mbarek, M., Saidi, K., and Amamri, M. *The relationship between pollutant emissions, renewable energy, nuclear energy and GDP: empirical evidence from 18 developed and developing countries*. International Journal of Sustainable Energy, 2017. p. 1-19.
59. Todreas, N. E. and Kazimi, M. S. *Nuclear systems: thermal hydraulic fundamentals*. 2012, USA: CRC press.
60. Ferguson, C. D. *Nuclear Energy: Balancing Benefits And Risks*. (No. 28). 2007, Council on Foreign Relations Press.
61. Kessler, G., Veser, A., Schlüter, F. H., Raskob, W., Landman, C. and Päsler-Sauer, J. The Risks of Nuclear Energy Technology: Safety Concepts of Light Water Reactors. 2014, Germany: Springer.
62. Cadenas, J. J. G. *The Nuclear Environmentalist Is There a Green Road to Nuclear Energy?*. 2012, Springer.
63. Nuclear Energy Agency (NEA). *The Role of Nuclear Energy in a Low-carbon Energy Future, Nuclear Development.* 2012, France: NEA.
64. WEO, I. International Energy Agency. *World Energy Outlook 2005*. 2005, France: International Energy Agency.
65. WEO, I. International Energy Agency. *World Energy Outlook 2006*. 2006, France: International Energy Agency.
66. WEO, I. International Energy Agency. *World Energy Outlook 2009*. 2009, France: International Energy Agency.
67. Bostan, I., Gheorghe, A. V., Dulgheru, V., Sobor, I., Bostan, V. and Sochirean, A. *Resilient energy systems: renewables: wind, solar, hydro (Vol. 19)*. 2013, Springer.
68. Roy, U. K., and Majumder, M. *Impact of Climate Change on Small Scale Hydro-turbine Selections*. 2016, Singapore: Springer.
69. Majumder, M. *Minimization of Climatic Vulnerabilities on Mini-hydro Power Plants: Fuzzy AHP, Fuzzy ANP Techniques and Neuro-Genetic Model Approach*. 2016, Singapore: Springer.
70. International Energy Agency. *Technology Roadmap Hydropower*. 2012, France: IEA.
71. Wagner, H. J., and Mathur, J. *Introduction to hydro energy systems: basics, technology and operation*. 2011, Springer.
72. Chiras, D. *Wind power basics: a green energy guide*. 2010, Canada, New Society Publishers.
73. Nelson, V. *Wind energy: renewable energy and the environment Second Edition*. 2014, USA: CRC press.
74. Wei Zheng, C., & Pan, J. (2014). *Assessment Of The Global Ocean Wind Energy Resource*. Renewable and Sustainable Energy Reviews, 2014, 33: p. 382-391.
75. Bosch, J., Staffell, I., and Hawkes, A. D. *Temporally-Explicit And Spatially-Resolved Global Onshore Wind Energy Potentials*. Energy, 2017, 131: p. 207-217.
76. Dupont, E., Koppelaar, R., & Jeanmart, H. *Global Available Wind Energy With Physical And Energy Return On Investment Constraints*. Applied Energy, 2018, 209: p. 322-338.
77. Zheng, C. W., Li, C. Y., Pan, J., Liu, M. Y. and Xia, L. L. *An Overview Of Global Ocean Wind Energy Resource Evaluations*. Renewable and Sustainable Energy Reviews,

2016, 53: p. 1240-1251.

78. International Energy Agency. *Technology Roadmap Wind Energy*. 2013, France: IEA.
79. Vasi, I. B. *Winds Of Change: The Environmental Movement And The Global Development Of The Wind Energy Industry*. 2011, UK: Oxford University Press.
80. Burton, T., Jenkins, N., Sharpe, D., and Bossanyi, E. *Wind Energy Handbook*. 2011, UK: John Wiley & Sons.
81. Reda, F. *Solar Assisted Ground Source Heat Pump Solutions: Effective Energy Flows Climate Management*. 2017, Switzerland: Springer.
82. Asplund, R. W. *Profiting from Clean Energy: A Complete Guide to Trading Green in Solar, Wind, Ethanol, Fuel Cell, Carbon Credit Industries, and More*. 2008, USA: John Wiley & Sons.
83. Tabak, J. *Solar And Geothermal Energy*. 2009, USA: Infobase Publishing.
84. Brown, L. R. *The great transition: Shifting from fossil fuels to solar and wind energy*. 2015, USA: WW Norton & Company.
85. Plante, R. H. *Solar Energy, Photovoltaics, and Domestic Hot Water: A Technical and Economic Guide for Project Planners, Builders, and Property Owners*. 2014, USA: Academic Press Elsevier.
86. Mir Artigues, P. and Del Río, P. The Economics and Policy of Solar Photovoltaic Generation. 2016, Switzerland: Springer.
87. International Renewable Energy Agency (IRENA). *Featured Dashboard – Capacity Generation, RESOURCE*. 2017, Abu Dhabi: IRENA.
88. Rule, T. A. *Solar, Wind And Land: Conflicts In Renewable Energy Development*. 2014, USA: Routledge.
89. Mauthner, F., Weiss, W., and Spörk-Dür, M. *Solar heat worldwide: markets and contribution to the energy supply (Solar Heating and Cooling Program)*. 2014, France: IEA.
90. International Energy Agency. Technology Roadmap Solar Photovoltaic Energy. 2014, France: IEA.
91. Dahlquist, E. (Ed.). *Biomass as Energy Source: Resources, Systems And Applications (Volume 3)*. 2012, CRC Press.
92. Renewable Heating and Cooling (RHC) European Technology Platform. (2014). *Biomass Technology Roadmap*. 2014, Belgium: European Technology Platform.
93. International Energy Agency. Technology Roadmap Bioenergy for Heat and Power. 2012, France: IEA.
94. Cheng, J. (Ed.). *Biomass to Renewable Energy Processes*. 2010, USA: CRC press.
95. Demirbas, A. *Potential Applications Of Renewable Energy Sources, Biomass Combustion Problems In Boiler Power Systems And Combustion Related Environmental Issues*. Progress in energy and combustion science, 2005 31 (2): p. 171-192.
96. De, S., Agarwal, A. K., Moholkar, V. S., and Thallada, B. (Eds.). Coal and Biomass Gasification: Recent Advances and Future Challenges. 2018, Singapore: Springer.

Available online at www.dergipark.gov.tr

INTERNATIONAL ADVANCED RESEARCHES
and
ENGINEERING JOURNAL

Journal homepage: www.dergipark.gov.tr/iarej

International
Open Access

Volume 02
Issue 01

April, 2018

e-ISSN: 2618-575X

Review Article

A review on the effects of micro-nano particle size and volume fraction on microstructure and mechanical properties of metal matrix composites manufactured via mechanical alloying

Sinem Aktaş [a]* ***and Ege Anıl Diler*** [b]

[a]*Interdisciplinary Division of Materials Science and Engineering, Ege University, Izmir, 35040, Turkey*
[b]*Department of Mechanical Engineering, Ege University, Izmir, 35040, Turkey*

ARTICLE INFO

Article history:
Received 05 March 2018
Revised 20 March 2018
Accepted 22 March 2018

Keywords:
Mechanical alloying
Mechanical properties
Metal matrix composites
Microstructure
Reinforcement particle size
Volume fraction

ABSTRACT

The major challenge for the production of the composites which are reinforced with nano and micro-sized particles is to obtain uniform distribution of reinforcement particles in microstructure. Powder metallurgy method can be used in order to obtain a homogeneous distribution of reinforcement particles. This method has three steps: 1) mixing and/or alloying of powders, 2) pressing, and 3) sintering. Mechanical alloying is a complex process which involves optimization of many parameters such as milling time, process control agent, particle size, ball to powder weight ratio, milling speed, milling atmosphere, mill types, etc. The main aim of the present study is to explain the roles of volume fraction and size of reinforcement particle on the microstructural properties and how these parameters affect the mechanical properties of aluminum based metal matrix composites with micro and nano-sized reinforcement particles produced by mechanical alloying.

1. Introduction

Metal matrix composites (MMCs) are manufactured by adding reinforcement particles with different sizes from micro to nano and various shapes into a metal matrix. The ceramic particles such as SiC, Al_2O_3 are usually used as reinforcement in MMCs. The addition of reinforcement particles into matrix can improve the mechanical properties of MMCs such as hardness, ultimate tensile strength (UTS), yield strength (YS) and wear resistance. For instance, Mazahary and Shabani [1] produced nanocomposite with SiC (50 nm) in A356 matrix. According to experimental results, strength values were increased by adding nano-sized SiC particles and this increment continued with the increasing of volume fraction of SiC particles until other mechanisms such as agglomeration and clustering took place. Many researchers have found similar results. For example, in a study [2] that the properties of Al-TiO_2 nanocomposites manufactured by powder metallurgy method were investigated, the results showed that wear resistance and the tensile strength of composites increased with an increase in volume fraction of nano particles.

There are several manufacturing methods in the production of metal matrix nanocomposites (MMNCs), which can be categorized into ex-situ and in-situ methods [3]. Ex-situ synthesis (for instance, powder metallurgy, mechanical milling, stir casting, etc.) consists of adding nano-sized reinforcement to a liquid or solid (powder) metal. On the other hand, in in-situ method, the reinforcements are synthesized in a metal matrix by chemical reactions among elements or between element and compound during the composite fabrication. Self-propagating high temperature synthesis (SHS), direct reaction synthesis (DRS) and reaction milling (RM) can be given as examples. Each of method in MMNCs production has some advantages and drawbacks [4-7].

Distribution of reinforcement particles in a metal matrix has a huge challenge as aforementioned. Heterogeneous distribution of reinforcement particles has a negative influence on the mechanical properties of

*Corresponding author. *Tel.: +90 555 020 1714*
E-mail address: synemaktas@gmail.com
Note: This study was presented at International Advanced Researches and Engineering Congress 2017 (IAREC'17)

metal matrix composites. Especially, when the size of reinforcement particles decreases from microscale to nanoscale, this drawback influence increases. On the other hand, it is possible to minimize the agglomeration of particles by means of mechanical alloying [8]. In this process, mixtures of powders are mechanically milled together.

2. Mechanism of Mechanical Alloying

Mechanical alloying is a useful technique for producing both microcomposites and nanocomposites [10]. Figures 1 and 2 show the schematic drawings of a high-energy planetary ball mill and a ball-powder-ball collision of powder mixture during mechanical alloying. In this method, there are three repeated steps following each other, which are deformation, cold welding and fracture. During the milling process, whenever balls collide with each other some of the powders are trapped in between them. This collision gives energy to system so that the particles transforms physically; in other words, they deform elastically and plastically.

In the early stages of milling, collide mechanism creates flake and new surfaces because soft particles have tendency to weld together. As a result, particle size is larger than the starting particle [12] (Figure 3).

The continuation of deformation leads to work hardening and fracture by a fatigue failure mechanism or by fragmentation of fragile flakes. In such a system, the tendency of fracture dominates over cold welding progressively when a balance is occurred (steady state condition) between welding and fracture. Average composite particle size decreases, and particles are steadily refined. Figures 4-6 show the effects of mechanical milling on the morphology [13].

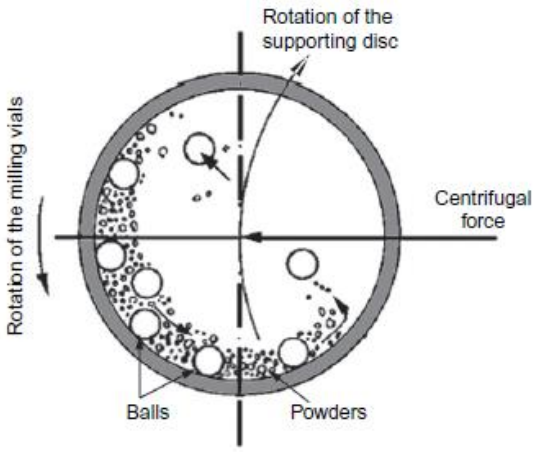

Figure 1. Schematic drawing of a high-energy planetary ball mill [9]

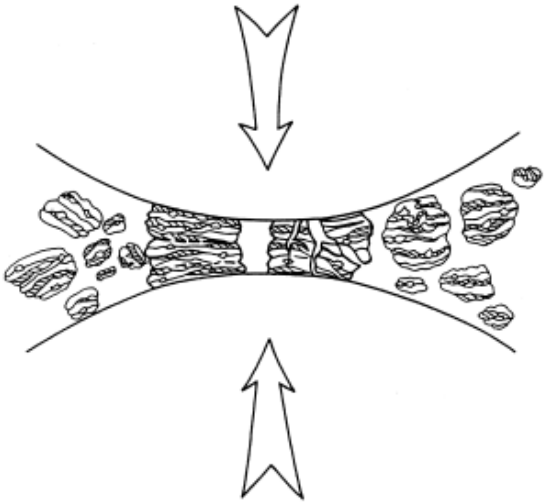

Figure 2. Ball-powder-ball collision of powder mixture during mechanical alloying [11]

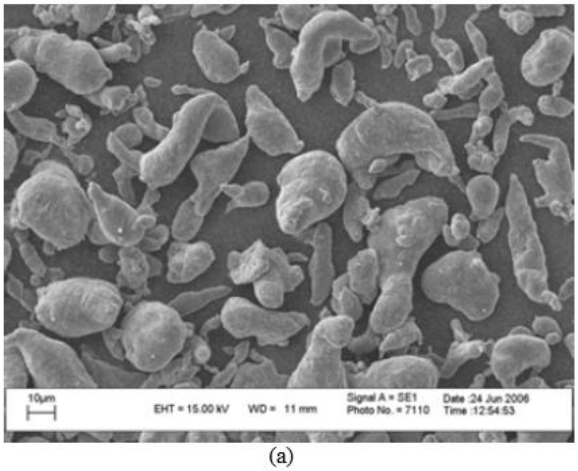

(a)

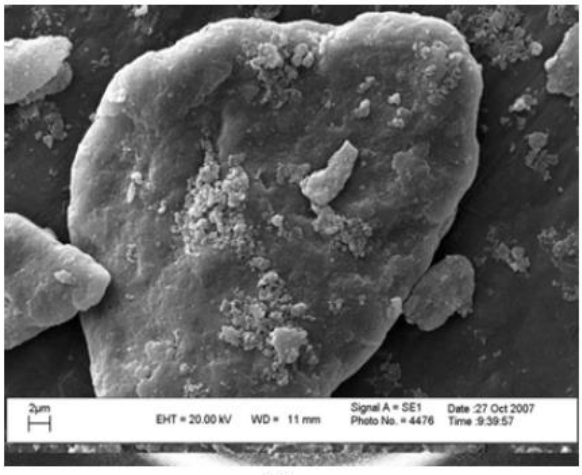

(b)

Figure 3. (a) The initial aluminum powders with particle size smaller than 63 μm in Al-Al_2O_3 nanocomposite system and (b) after 4h milling, flake like Al particles [12]

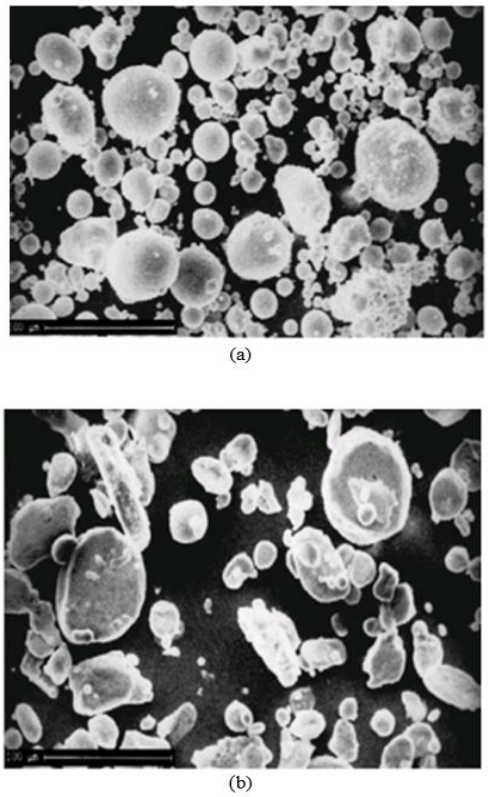

Figure 4. (a) Morphologies of the as received Al powder and (b) milled for 2 h [13]

As can be seen in figure 4, at the beginning of the milling process, particles deform plastically and their shapes start to change; also, average size of particles diminishes slightly. As milling time progresses, particles flatten with high aspect ratio and flake-like particles form (Figure 5). Also, micro welding can be observed between the particles.

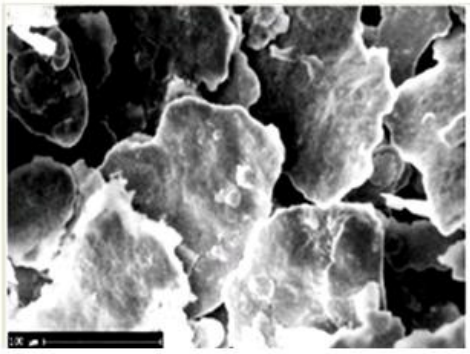

Figure 5. Morphology of Al powder milled for 12 h [13]

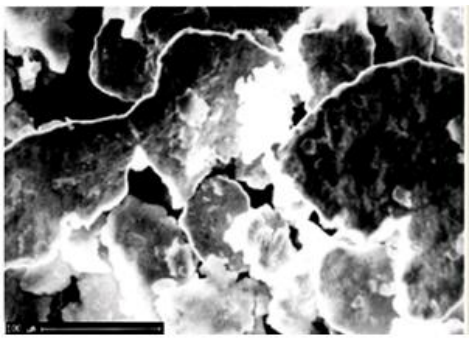

Figure 6. Morphology of Al powder milled for 18 h [13]

After long milling time, cold welded particles (Figure 6) start to fracture due to work hardening effect so particle size decreases and their shape converses from laminar to almost equiaxial. If welding and fracture are at equilibrium, the equiaxed particles are oriented randomly. It should be also noted that these stages of milling might occurs at the same time. All milling stages, namely, deformation, cold welding and fracture can be observed during manufacturing of ceramic reinforced metal matrix composite by mechanical alloying (Figure 7).

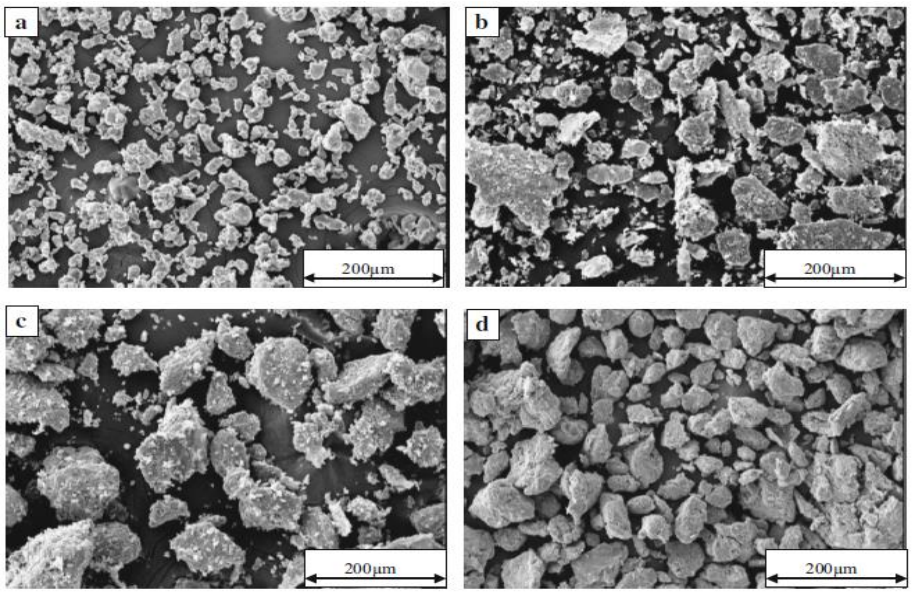

Figure 7. The evolution of morphology during mechanical milling of Al–2.5wt.%SiC nanocomposite powder milled for: (a) 2 h, (b) 15 h, (c) 20 h and (d) 25 h [14]

3. Effect of Particle Size

Particle size and volume fraction affect the milling stages of production and the microstructure of composite material, which define the mechanical properties of metal matrix composites with reinforcement particles. At early stage of milling, there is no remarkable and clear effectiveness of hard ceramic particles on alloying mechanism; however, at longer milling time, comparing to unreinforced metal particles, hard particles act as a milling agent. They initiate premature welding and fracture; in other words, reinforcement particles accelerate the milling process. Acceleration in a microcomposite is relatively faster than that in a nanocomposite [13]. Since when balls collide with each other or particles they give their energy to the system. Some amount of energy is spent to break and to separate the agglomerated and clustered nano particles.

Micro and nano scaled particles act as an obstacle against dislocation movement; furthermore, they can generate new dislocations. Comparing to microcomposites, dislocation density is higher for nanocomposites due to high interaction between reinforcement particles and matrix material. Decreasing of crystallite size depends on increasing dislocation density and work hardening. When dislocation density leads to work hardening, powders will be brittle, and finally, they will fracture. In others words, much more particles will fracture to smaller size. Also, it should be noted that Hall-Petch equation (1) defines to relation between mechanical properties and particle size.

$$\sigma_{y=}\, \sigma_0 + kd^{-1/2} \qquad (1)$$

Hall–Petch equation given where σ_0 is the friction stress in the absence of grain boundaries, σ_y is the yield stress, k is a constant and d is the grain size. According to Hall-Petch equation, the yield stress increases as grain size decreases.

However, if this size approaches threshold, inverse Hall-Petch will involve in this process [15]. After threshold value passes, particle size does not have positive effect on microstructure evolution and mechanical properties. Because, smaller particles have tendency for agglomeration which can deteriorate the uniform distribution of reinforcement particles and mechanical properties of composites reinforced with particles.

In a study about particle size effect on mechanical properties [16], the researchers produced aluminum matrix composites reinforced with 30 μm and 50 nm B_4C particles. The mixed powders were mechanically milled at 5, 10, 15 and 20 h (Figure 8).

After the 20 h milling, the crystallize size of the micro and nano composite were 55 nm and 40 nm, respectively (Figure 9). Also, hardness values of micro and nano composites were 118 and 130 HV, respectively (Figure 10).

As can be seen in figures 10 and 11, the hardness and strength values of nanocomposite are higher than microcomposite due to Orowan strengthening mechanism [17]. Orowan strengthening effect increases with decreasing particle size but there is a critical value and this effect drops suddenly below the critical threshold.

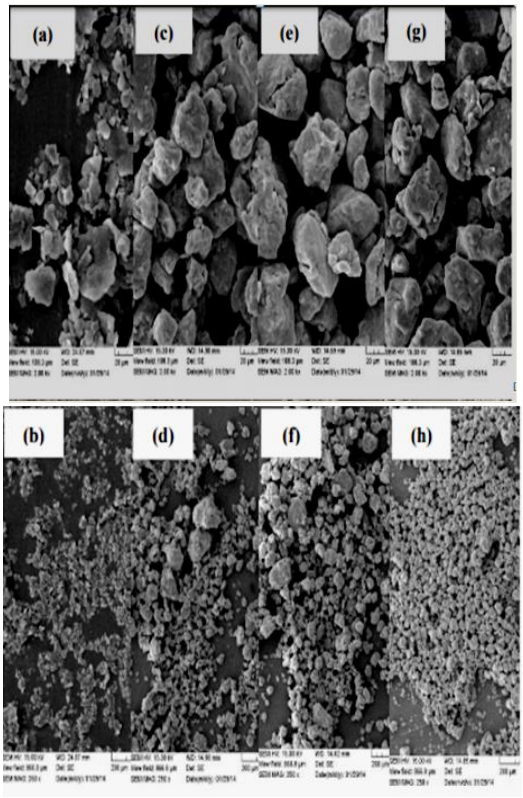

Figure 8. Morphology of nano-composite powders after (a) and (b) 5 h, (c) and (d) 10 h, (e) and (f) 15 h, and (g) and (h) 20 h milling time [16]

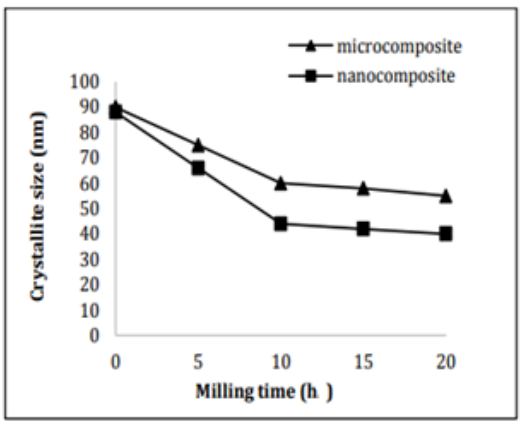

Figure 9. The change of the crystallite size for the microcomposite and nanocomposite [16]

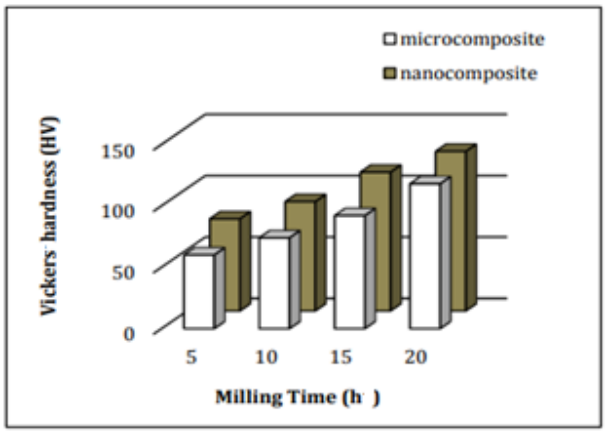

Figure 10. The variation of Vickers hardness of the microcomposite and nanocomposite with the milling [16]

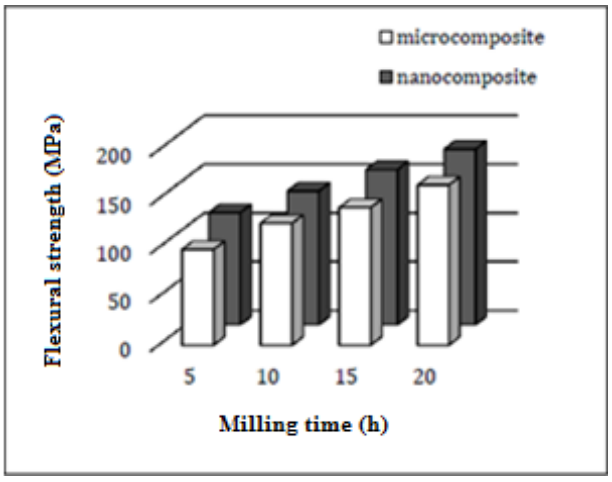

Figure 11. The variation of flexural strength of the microcomposite and nanocomposite with the milling [16]

4. Effect of Volume Fraction

The other parameter which affects microstructure, milling mechanism and mechanical properties is volume fraction of reinforcement particles. Firstly, increasing volume fraction of particles enhances grain refinement due to the fact that local plastic deformation increases. There are some reasons this increment. One of them is the formation of shear bands containing a high dislocation density depending on prevention of dislocation movement by particles. Also, formation of subgrains or cell conversing into grains and sliding these grains leads to increasing local plastic deformation [18]. This phenomenon is noticeable when nanometric particles are used because of Orowan strengthening mechanism.

In a study [19], the effect of volume fracture on average particle size, density and compressive stress were investigated (Figures 12 and 13). According to results, finer particle size has a positive effect on mechanical properties.

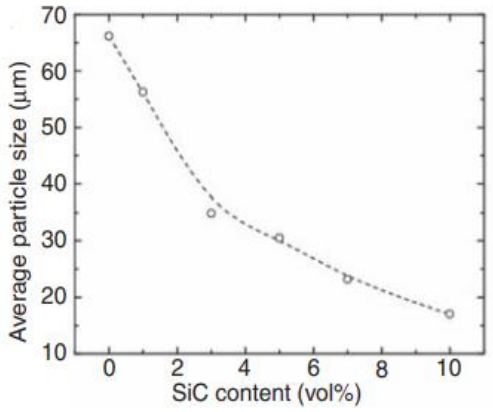

(a)

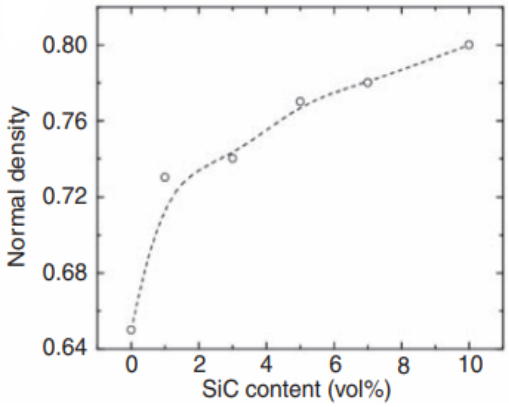

(b)

Figure 12. Effect of SiC content on (a) the average particle size and (b) density of mechanically milled powders [19]

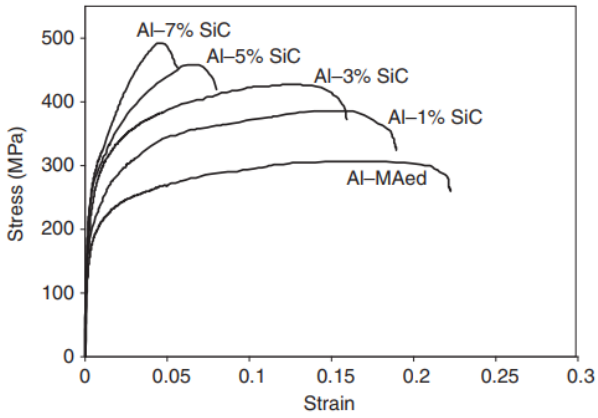

Figure 13. Compressive curves of Al and Al-SiC composites prepared by mechanical alloying and sintering [19]

Volume fraction has an influence on milling stages. Pakserethet A.H. et al. [14] examined the influence of different volume fractions (2.5, 5, 10, 15 and 20 vol.%) on microstructure and mechanical properties of Al-SiC nanocomposites. According to this study, when 2.5 vol.% SiC compared to 10 vol.% SiC in matrix, steady state occurred in shorter milling time. This correlation was observed as 25 h in 2.5 vol.% and 20 h in 10 vol.%

SiC; furthermore, while cold welding mechanism was showing up after 2 h in 20 vol.%, 2.5 vol.% SiC powder mixture needed 15 h to achieve the same condition because of the fact that nano-sized SiC particles rise the energy induced, which accelerates process.

Many researchers have found similar results. Amal and Nassar [2] studied the properties of Al-TiO_2 nano composites manufactured by powder metallurgy method and the results showed that wear resistance (Figure 14) and the tensile strength of composites increased with an increase in volume fraction of nano particles.

In a study found in literature, C. Suryanarayana [20] put forth how volume fraction and particle size affect the mechanical properties of Al metal matrix composites reinforced with Al_2O_3 particles of 50 and 150 nm. For a constant particle size (50 nm), compressive yield strength was measured as 488 MPa for Al-Al_2O_3 composites with 5 vol.% while this value increased to 515 MPa for Al-Al_2O_3 composites with 10 vol.%. As the volume fraction of reinforcement particles increased, the mechanical properties of composites improved. Also, it can be seen in Table 1 that the decreasing of particle size resulted in increasing strength.

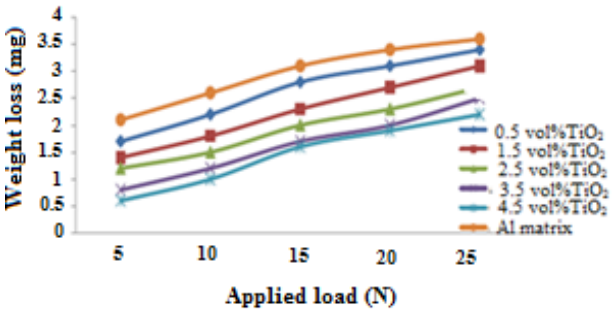

Figure 14. Effects of applied load on wear resistance [2]

Table 1. Mechanical properties of Al–Al_2O_3 nanocomposites obtained by milling and subsequent consolidation by vacuum hot pressing and hot isostatic pressing [20]

Particle size of Al_2O_3 (nm)	Volume fraction of Al_2O_3 (%)	Compressive yield strength (MPa)	Compressive strength (MPa)
50	5	488	605
50	10	515	628
150	5	409	544
150	10	461	600

5. Conclusion

The studies found in literature have shown that particle size and volume fraction have extremely significant influence on microstructure and mechanical properties of metal matrix composite reinforced with micro and nano-sized particles in production via mechanical alloying.

The addition of reinforcement particles into the metal matrix increases dislocation density and work hardening, which leads to enhancement of mechanical properties of particle reinforced metal matrix composites. However, this increment for a nanocomposite is higher than that for a microcomposite due to Hall-Petch effect and Orowan strentghening mechanism.

Comparing to unreinforced metal powders, hard particles act as a milling agent. They initiate premature welding and fracture mechanism. Reinforcement particles accelerate the milling process; therefore, acceleration in a microcomposite is relatively faster than that in a nanocomposite because of the fact that some amount of energy is spent to break and to separate the agglomerated and clustered nano particles.

Grain refinement effect increases as volume fraction of reinforcement particles increases; moreover, milling stage occurs earlier.

As a result, nano-sized reinforcement particle with increasing volume fraction has a stronger influence on microstructure and mechanical properties of metal matrix composites that are reinforced with particles and produced via mechanical alloying.

Acknowledgment

This work was supported by Scientific Research Projects (BAP) Directorate of Ege University (project no:16-MÜH-107, 17-FBE-008).

References

1. Mazahary A., and M.O. Shabani, *Mechanical properties of A356 matrix composites reinforced with nano SiC particles*, Strength of Materials, 2012. **44**(6): p. 146-155.
2. Amal E.N., and E.E. Nassar, *Properties of Al matrix nano composites prepared by powder metallurgy processing*, Journal of King Saud University-Engineering Science, 2017. **29**(3): p. 295-299.
3. Dongshuai Z., F. Qiu, H. Wang, and Q. Jiang, *Manufacture of nano-sized particle-reinforced metal matrix composites: A Review*, Acta Metall. Sin.(Eng. Lett.), 2014. **27**(5): p. 798-805.
4. Murthy N.V., A.P. Reddy, N. Selvaraj, and C.S.P. Rao, *Aluminium metal matrix nano composites-manufacturing methods: A Review*, International Journal of Mechanical Engineering, 2015, **4**(4): p.24-44.
5. Sajjadi S.A, H.R. Ezatpour, and H. Beygi, *Microstructure and mechanical properties of Al-Al_2O_3 micro and nano composites fabricated via stir casting*, Materials Science and Engineering A, 2011. 528: p. 8765-8771.
6. Jose J.G., R. Catalin, G.V. Picu, M. Nithin, S. Thomas, A. Lopes, and C. Buchheim, *Mechanical behaviour of Al-SiC nanocomposites produced by ball milling and spark plasma sintering*, Metallurgical and Materials Transactions A, 2013. 44 A: p. 5259-5269

7. Endalkachew M., V.Y. Bazhin, and S. Savchenkow, *Review on nano particle reinforced aluminum metal matrix composites*, Research Journal of Applied Sciences, 2016. **11**(5): 188-196.
8. Aizadeh A., M. Khademian, and A. Abdollahi, *Investigation of fabrication method effects on microstructure and mechanical properties of Al-2wt %B_4C nanocomposite*, [cited 2017 29 August]; Avaliable from:http://www.ias.ac.in/public/Volumes/boms/forthcoming/BOMS-D-15-00636.pdf
9. Sherif M.E., *Mechanical Alloying*, *Nanotechnology*, *Materials Science and Powder Metallurgy*. 2015, Elsevier.
10. Prabhu B., C. Suryanarayana, L. Ana, and R. Vaidyanathan, *Synthesis and characterization of high volume fraction Al-Al_2O_3 nanocomposite powders by high energy milling*, Materials Science and Engineering A, 2006. 425: p.192-200.
11. Suryanarayana C., *Mechanical milling and alloying*, Progress In Materials Science, 2001. 46: p. 1-184.
12. Mahboob H., S.A. Sajjadi, and S.M. Zebarjad, *Synthesis of Al-Al_2O_3 nanocomposites by mechanical alloying and evaluation of the effect of ball milling time on the microstructure and mechanical properties*, in ICMM'08: Kuala Lumpur. p. 240-245.
13. Razavi Z.H., A. Simchi and S.M. Reihani, *Structural evolution during mechanical milling of nanometric and micrometric Al_2O_3 reinforced Al matrix composite*, Materials Science and Engineering A, 2006. 428: p. 159-168.
14. Paksereht A.H., A. Baghbaderani and R. Yazdani, *Role of different fractions of nano sized SiC and milling time on the microstructure and mechanical properties of Al-SiC nanocomposites*, Transactions of the Indian Institute of Metals, 2016. **69**(5): p. 1007-1014.
15. Carlton C.E., and P.J. Ferreira, *What is behind the inverse Hall-Petch effect in nanocrystalline materials?* ActaMaterialia, 2007. 55: p. 3749-3756.
16. Allalhesabi S., S.A. Manafi and E. Borhani, *The structural and mechanical properties of Al-2.5%wt. B4C metal matrix nano composite fabricated by mechanical alloying*, Mechanics of Advanced Composites Structures, 2015. 2: p. 39-44.
17. Zhang Z., and D.L. Chen, *Contribution of Orowan strengthening effect in particulate-reinforced metal matrix nanocomposite*, Materials Science and Engineering A, 2008. 483-484: p. 148-152.
18. Kamrani S., A. Simchi, R. Riedel and S.M.S. Reihani, *Effect of reinforcement volume fraction on mechanical alloying of Al-SiC nanocomposite powders*, Powder Metallurg, 2007. **50**(3): p. 276-282.
19. Kamrani S., R. Riedel, S.M.S. Reihani, and H.J. Kleebe, *Effect of reinforcement volume fraction on the mechanical properties of Al-SiC nanocomposites produced by mechanical alloying and consolidation*, Journal of Composite Materials, 2010. 44: p. 313-326.
20. Suryanarayana C., *Synthesis of nanocomposites by mechanical alloying*, Journal of Alloys and Compounds, 2001. 509: p. 229-234.